

Universidade do Minho

Escola de Engenharia

Fernando Luís Bior Mendes

**Optical sensor system for monitoring
the pH of cellular media: application to
an Organ-on-a-chip platform**

Dissertação de Mestrado

Mestrado Integrado em Engenharia Física

Trabalho efetuado sob a orientação de

Professora Doutora Raquel O. Rodrigues

Professor Doutor Stefan Gassmann

setembro de 2020

DECLARAÇÃO

Nome: Fernando Luís Bior Mendes

Título da dissertação: Optical sensor system for monitoring the pH of celular media: application to an Organ-on-a-chip platform

Orientadores:

Professora Doutora Raquel O. Rodrigues

Professor Doutor Stefan Gassmann

Ano de conclusão: 2020

Mestrado em Engenharia Física

É AUTORIZADA A REPRODUÇÃO INTEGRAL DESTA DISSERTAÇÃO APENAS PARA EFEITOS DE INVESTIGAÇÃO, MEDIANTE DECLARAÇÃO ESCRITA DO INTERESSADO, QUE A TAL SE COMPROMETE.

Universidade do Minho, ____/____/_____

Assinatura:

DIREITOS DE AUTOR E CONDIÇÕES DE UTILIZAÇÃO DO TRABALHO POR TERCEIROS

Este é um trabalho académico que pode ser utilizado por terceiros desde que respeitadas as regras e boas práticas internacionalmente aceites, no que concerne aos direitos de autor e direitos conexos.

Assim, o presente trabalho pode ser utilizado nos termos previstos na licença abaixo indicada.

Caso o utilizador necessite de permissão para poder fazer um uso do trabalho em condições não previstas no licenciamento indicado, deverá contactar o autor, através do RepositóriUM da Universidade do Minho.

Licença concedida aos utilizadores deste trabalho



Atribuição-NãoComercial-SemDerivações
CC BY-NC-ND

<https://creativecommons.org/licenses/by-nc-nd/4.0/>

[Esta é a mais restritiva das nossas seis licenças principais, só permitindo que outros façam download dos seus trabalhos e os compartilhem desde que lhe sejam atribuídos a si os devidos créditos, mas sem que possam alterá-los de nenhuma forma ou utilizá-los para fins comerciais.]

STATEMENT OF INTEGRITY

I hereby declare having conducted this academic work with integrity. I confirm that I have not used plagiarism or any form of undue use of information or falsification of results along the process leading to its elaboration.

I further declare that I have fully acknowledged the Code of Ethical Conduct of the University of Minho.

This work results partially of the project NORTE-01-0145-FEDER-029394, RTChip4Theranostics, supported by Programa Operacional Regional do Norte - Norte Portugal Regional Operational Programme (NORTE 2020), under the PORTUGAL 2020 Partnership Agreement, through the European Regional Development Fund (ERDF) and by Fundação para a Ciência e Tecnologia (FCT), IP, project reference PTDC/EMD-EMD/29394/2017.

NORTE-01-0145-FEDER-029394



PTDC/EMD-EMD/29394/2017



"I seem to have been only like a boy playing on the seashore, and diverting myself in now and then finding a smoother pebble or a prettier shell than ordinary, whilst the great ocean of truth lay all undiscovered before me."

Isaac Newton

"It is strange that only extraordinary men make the discoveries, which later appear so easy and simple."

Georg C. Lichtenberg

Acknowledgments

The author acknowledges the support given by the Erasmus Placement mobility programme and the University of Minho, especially to the International Relations Office for the concern during the mobility program and for allowing the scholarship for the elaboration of the Master's thesis in cooperation with Jade Hochschule - Wilhelmshaven, Germany.

To my advisor and co-advisor Professor Doctor Raquel O. Rodrigues and Professor Doctor Stefan Gassmann, and lab technicians Dipl.-Ing. Helmut Schütte and Dipl.-Ing. Robert Buse, all the support and knowledge that they shared with me, and all the help they gave me during my experience in Germany.

A special thanks to Professor Doctor Graça Minas and Professor Doctor Thomas for being two very important pillars and guides in the Portuguese and German universities, respectively, that helped me know in which direction to proceed with my work and study.

For the engineers Raquel Lopes and Miguel Madureira who have been two great supports in professional and personal terms in my research course abroad. They helped me to believe and to be resilient and patient.

To all the Jade Hochschule, especially to Mechanical & Optics laboratory for the availability of its facilities, with great work conditions.

To everyone who was present and marked me during my academic journey, especially to all professors who shared their knowledge with me.

To Inês Carvalho my great gratitude for teaching me to be better and good to everyone. More than a colleague, she was an incredible friend who marked my academic journey more than anyone, who was present in everything.

Finally and with love, to all my family and friends for always believing in me and all the patient.

Abstract

pH is a physiological parameter that changes its value according to cellular state of a human organ. When a tumour is being developed, it is known that they have a more acid interstitial pH than normal tissues. This is mainly due to the high metabolic activity of the abnormal cells with increase of acidic sub-products and the absence of organised vasculature of tumours, that leads to poor tissue oxygenation. Indeed, in *in vitro* animal systems, such as static cell culture experiments or advanced microfluidic devices, the cell's metabolic activity during incubation causes the alteration of the cell culture pH, which drops the pH from close to the physiological (7.4) to acidic ones (lower than 7.0). Because low environmental pH inhibits cell survival, proliferation and activity, cell culture media has to be consecutively replaced for fresh one.

For the pH monitoring, cell culture media is, in general, complemented with a pH colorimetric indicator (e.g. phenol red). However, the colour change of the cell culture media does not quantify the pH value. For this reason, the monitoring and quantification of cell culture medium pH, especially in advanced cell culture devices, such as organ-on-a-chip (OoC), which contain healthy and/or tumour organ models, is still a challenge and a parameter of utmost importance for the maintenance of homeostasis (auto-regulation).

The pH of tissues can be measured by a variety of techniques, being pH electrodes the most used. Nevertheless, other methods can be used for pH measurement, such as optical sensors. In general, this technique eliminates the tissue injury effects, but results in an integrated measurement over a long period and demanding a relatively large volume of sample.

Particularly, in OoC platforms, the small size of each OoC constituent part, has triggered the development of micro(bio)sensors to be integrated in the microchambers that feed the perfusion chambers containing the organ models, which are used for monitoring the pH of the cell culture media in circulation.

In this study, a literature review of pH sensors that can be miniaturised and integrated in OoC was investigated. Based on this previews literature research, and the presence of a colorimetric pH indicator (phenol red) that is commercially added to cell culture media, a miniaturization of an optical pH sensor, for real-time sensing of the cell culture medium feeding advanced microfluidic devices was investigated. This strategy can have several advantages, such as low-cost implementation and improvement of the pH reading based on the beam-splitter phenomenon. For

this purpose, a microchamber, processed by micromilling in PMMA, was developed and optimised to support the pH optical sensing system, creating a prototype device that can be directly incorporated into an OoC platform.

For the pH sensing experiments, buffered solutions with established pH and phenol red were used to test and optimize the optical sensor, by analysing their transmittance signal. In this study, the colorimetric pH indicator (phenol red) was added in the same concentration than the one used in commercial cell culture media. The results shown that the pH reading was successful achieved in intervals of 0.2 pH units, in a range between 6.0 to 8.0.

Keywords: Optical sensor, Beam-splitter, Organ-on-a-chip, Cell culture medium, Buffer solutions, Phenol red, pH, Microchamber, Micromilling.

Resumo

O pH é um parâmetro fisiológico, cujo valor se altera de acordo com o estado celular de um órgão humano. Quando um tumor está em proliferação, este tem um pH intersticial mais ácido do que os tecidos normais. Isto deve-se principalmente à elevada atividade metabólica das células anormais com o aumento de subprodutos ácidos e a ausência de vasculatura organizada dos tumores, que leva à pobre oxigenação dos tecidos. De facto, em sistemas animais *in vitro*, tais como experiências de cultura celular estática ou dispositivos microfluídicos avançados, a atividade metabólica da célula durante a incubação provoca a alteração do pH da cultura celular, que baixa o pH de perto do fisiológico (7.4) para um mais ácido (inferior a 7.0). O baixo pH fisiológico inibe a sobrevivência, proliferação e atividade celular, e, em consequência, os meios de cultura celular têm de ser substituídos consecutivamente.

Para a monitorização do pH, os meios de cultura celular são, em geral, complementados com um indicador colorimétrico de pH (por exemplo, vermelho de fenol). No entanto, a mudança de cor dos meios de cultura celular não quantifica o valor do pH. Por esta razão, a monitorização e quantificação do pH dos meios de cultura celular, especialmente em dispositivos avançados de cultura celular, tais como *Organ-on-a-chip* (OoC), que contêm modelos de órgãos saudáveis e/ou tumorais, é ainda um desafio e um parâmetro da maior importância para a manutenção da homeostase (autorregulação).

O pH dos tecidos pode ser medido por uma variedade de técnicas, sendo os elétrodos de pH os mais utilizados. Contudo, outros métodos podem ser utilizados para a medição do pH, tais como os sensores óticos. Esta técnica elimina os efeitos da lesão tecidual, mas resulta numa medição integrada durante um longo período e a partir de um volume relativamente grande de amostra.

Particularmente, nas plataformas de OoC, o pequeno tamanho de cada parte constituinte de OoC, desencadeou o desenvolvimento de micro(bio)sensores para serem integrados nas microcâmaras que alimentam as câmaras de perfusão, as quais contêm os modelos de órgãos, e que podem ser utilizados para monitorizar o pH dos meios de cultura celular em circulação.

Neste estudo, foi investigada uma revisão bibliográfica de sensores de pH que podem ser miniaturizados e integrados na OoC. Com base nesta pesquisa bibliográfica prévia, e a presença de um indicador colorimétrico de pH (vermelho fenol) que é comercialmente adicionado aos meios de cultura celular, foi investigada uma miniaturização de um sensor ótico de pH para a deteção

em tempo real do meio de cultura celular que alimenta dispositivos microfluídicos avançados. Esta estratégia pode ter várias vantagens, tais como a implementação a baixo custo e a melhoria da leitura do pH com base no fenômeno do separador de feixe. Para este efeito, foi desenvolvida e otimizada uma microcâmara, processada por *micromilling* em PMMA, para apoiar o sistema de detecção ótica de pH, criando um dispositivo protótipo que pode ser diretamente incorporado numa plataforma OoC.

Para as experiências de detecção de pH, foram utilizadas soluções tampão com pH estabilizado e vermelho fenol para testar e otimizar o sensor ótico, através da análise do seu sinal de transmitância. Assim, o indicador colorimétrico de pH vermelho de fenol foi adicionado na mesma concentração encontrada nos meios de cultura celular comerciais. Os resultados mostram que a leitura do pH foi bem-sucedida em intervalos de 0.2 unidades de pH, num intervalo entre 6.0 a 8.0.

Palavras-chave: Sensor ótico, *Beam-splitter*, *Organ-on-a-chip*, Meio de cultura, Soluções tampão, Vermelho fenol, pH, Microcâmara, *Micromilling*.

Table of contents

Acknowledgments	vii
Abstract	viii
Resumo	x
Table of contents	xii
List of figures	xiv
List of tables	xix
List of abbreviations	xx
Chapter I – Introduction	1
1.1. Objectives and Motivation	2
1.2. Structure	4
Chapter II - State of the Art	5
2.1. Micro-Electro-Mechanical Systems (MEMS)	6
2.2. Microfluidics	8
2.3. Organ-on-a-chip (OoC)	10
2.3.1. Organ-on-chip sensing and control	11
2.4. Medium for cell culture	13
2.4.1. pH in cell culture medium	13
2.4.2. RPMI 1640	14
2.4.3. Phenol red	15
2.5. pH sensors	17
2.5.1. Electrochemical pH sensors	18
2.5.2. Optical pH sensors	20
2.6. Spectrophotometry concepts	27
2.6.1. Quantitative analysis of light	27
2.6.2. Spectrophotometry measurements	30
Chapter III - Development and implementation of the optical pH sensor	32
3.1. Microfluidic Chamber	33
3.1.1. The material selection	34
3.1.2. Microfabrication	35
3.2. Design of the photodetection system	44
3.2.1. Light source	44
3.2.2. Photodetector	46

3.2.3. Software for signal acquisition using Arduino	47
3.2.4. Acquisition hardware and reading	48
3.2.5. Holding the acquisition chip board	50
3.3. Design of the Beam-splitter Sensor	52
3.3.1. Conceptual design	52
3.3.2. Base structure	54
3.3.3. Lens and optical path	55
3.3.4. Adaptation to Adafruit AS7262	57
3.3.5. PMMA microchip	59
3.3.6. Sensor and acquisition on PCB	59
3.3.7. Interface algorithm and software	60
Chapter IV - Results and Discussion	62
4.1. Macroscopic measurements of pH solutions	63
4.1.1. Preparation of pH buffer solutions with phenol red	63
4.1.2. Transmittance response acquisition on 1 cm cuvettes – pre-study	64
4.2. Microfluidic chamber measurements	67
4.3. Photodetection spectral behaviour	70
4.4. pH measurements using 1 cm cuvette	71
4.5. pH measurements using 1 mm chamber	74
4.6. pH measurements using 2 mm chamber	79
4.7. pH measurements using beam-splitter sensor	83
4.7.1. Stability and signal noise	83
4.7.2. Proof of operation	84
4.7.3. Final measurements	87
4.7.4. User interface	90
Chapter V - Conclusion and Future applications	91
5.1. Final remarks	92
References	94
Appendix I	109
Appendix II	112
Appendix III	115
Appendix IV	118
Appendix V	121

List of figures

Figure 1 - First polysilicon surface micromachines MEMS device integrated with circuits (Howe & Muller, 1986).....	6
Figure 2 - Setup of a continuous-flow microfluidic device (Vullev et al., 2006).	9
Figure 3 - A concept drawing of a four-organ μ Hu (Homo chippiens). (A) An on-chip peristaltic ventricular assist, (B) Right heart, (C) Lung, (D) Left heart, (E) Liver, (F) Peripheral circulation, (G) Microchemical analyser of metabolic activity. The system would work on a single microfluidic chip, with on-chip pneumatic valves controlling system functions and connections (Wikswow et al., 2013).	11
Figure 4 - Graph showing the relationship between pH and pCO_2 in three media. Solution A, bicarbonate enriched medium. Solution B, standard medium. Solution C, bicarbonate-deficient medium (TAYLOR, 1962).	13
Figure 5 - RPMI 1640 from ThermoFisher (A) without phenol red and (B) with phenol red.	15
Figure 6 - Structure of phenol red (Berthois et al., 1986).	16
Figure 7 - Phosphate buffers (100 mL) with phenol red (concentration of 1.1 mg/L) for different pH values.....	16
Figure 8 - Schematic representation of (A) potentiometric pH sensor fabricated by screen-print method, (B) thick film Ag/AgCl RE, (C) IDE based conductimetric pH sensor and (D) chemi-resistor (Manjakkal et al., 2020).....	19
Figure 9 - Optical fiber array-based sensor: (a) schematic illustration of high throughput optical sensor array system, (b) the assembly of microfluidic detection, (c) the photograph microfluidic detection chip, (d) the illustration of each detection unit (cross-sectional view) and (e) the photograph of the assembled high throughput optical sensor array (Wu et al., 2009).....	23
Figure 10 - Scheme of pH sensor based on POF (Arifin et al., 2019).	24
Figure 11 - Fabricated devices and test setup. (a) Exploded view of the sensing module for pH and oxygen measurement, (b) photograph of the fabricated sensing module, (c) schematic of the bioreactor, (d) photograph of the fabricated bioreactor, (e) schematic of the sensing module integrated with a peristaltic pump, culture medium reservoir, and bioreactor in a fluidic system (Shaegh et al., 2016).....	25
Figure 12 - Schematic of the fabricated fluidic detection chamber with integrated optical components: (a) exploded view (b) assembled view and, (c) schematic of detection level of light absorption in culture medium using solid-state optics (Shaegh et al., 2016).....	26
Figure 13 - Schematic of the decrease in radiant power of a monochrome radiation after crossing a cuvette of width, l , containing a solution with a concentration, c , in the component under study and a characteristic molar absorption coefficient, ϵ (Spencer Lima, 2013).....	29
Figure 14 - Molecular structure of PMMA (Altuglas International, 2006).....	34
Figure 15 - Setup for Micromilling in Fachbereich Ingenieurwissenschaften Labore Technische Optik&Mikrofertigung, at Jade Hochschule.	36
Figure 16 - Window of <i>AutoCAD</i> software.	36
Figure 17 - Visual Mill window and its different properties.	37
Figure 18 - Mach3 window.	38
Figure 19 - Tools used in micromilling of the company Zecha.	39

Figure 20 - Microscope Sensofar and the milled device.....	40
Figure 21 - (a) Zone of junction of the two liquids in a 3D bifurcation geometry, and (b) its corresponding profile; (c) first curvature where the liquids reach of the mixing area of the microchannel, in 3D, and, (d) its corresponding profile.....	40
Figure 22 - Microchannel with 1 mm chamber designed by steps, (a) top view of the device, (b) top view of the microchamber, (c) side view of the microchamber, (d) 3D view of the device and (e) 3D view of the microchamber, all in AutoCAD.....	41
Figure 23 - Optical glue used to glue the tubes with PMMA.....	42
Figure 24 - Microfluidic devices with microchannels and a 1 mm chamber fabricated in PMMA assembled with connecting tubes.	43
Figure 25 - Schematic of the source light on Eagle software.	44
Figure 26 - Board design for the source light PCB on Eagle Software.....	44
Figure 27 - (a) Apparatus with camera with brightness connected to a computer via USB, monitored in the software splovieview interface, micro-camera, two optical filters 1/10 and 1/5 and LED on to obtain (b) the incidence behaviour of the 3 components of white light emitted by the LED.....	45
Figure 28 - Example of the spectra intensity of the LED obtained with spectrometry on OceanView software.....	45
Figure 29 - (a) Adafruit AS7262 and (b) its photodiode array.	46
Figure 30 - AS7262 Visible Spectral_ID System. (ams AG, 2016).....	46
Figure 31 - Pinout Diagram of MICRO ARDUINO board, available on Arduino Store. © 2020 Arduino.....	50
Figure 32 - AutoCAD design of Holder for Adafruit AS7262 with a hole representative of the photodetector entrance.....	51
Figure 33 - (a) Microscope and the part to align. (b) Pinhole to align. (c) Adaptor to connect optical fiber to Adafruit AS7262. (d) Setup to achieve the spectral responsivity od Adafruit AS7262.	51
Figure 34 - Sensor conceptual design in AutoCAD.....	53
Figure 35 - Optical path diagram on beam-splitter with thickness d (Vis-nir, 2020).	53
Figure 36 - Exemplary transmission for TBP VIS-NIR 50:50 for 450 - 1000 nm ($\alpha=45^\circ$; unpolarised) (Vis-nir, 2020).....	54
Figure 37 - a) Sensor structure base cube. (b) Function level of the beam-splitter support in the base cube (LINOS Microbench, Bench and Rail Systems, n.d.).....	54
Figure 38 - Achromatic lens with a 60 mm focal length in the holder.....	55
Figure 39 - Schematic of how the object and image meet concerning the lens.	55
Figure 40 - Qioptic N mounting plates for (A) LED PCB and (B) lens.	56
Figure 41 - AutoCAD design of pinhole (light stop).	57
Figure 42 - (a) Schematics of the shift in the optical path. (b) Representation of not negligible optical path shift and fundamental trigonometry to calculate it.	57
Figure 43 - AutoCAD design of the front side of the holder to Adafruit AS7262.	58
Figure 44 - AutoCAD design of PMMA chip of 1 mm microchamber of the sensor.	59
Figure 45 - Eagle design of sensor PCB board.	59
Figure 46 - Sensor viewed from (a) right side, (b) left side, (c) front and (d) back.....	60
Figure 47 - Solutions A and B with phenol red in 500 mL volumetric balloon.....	64
Figure 48 - Buffer solutions and water (reference solution) in 1 cm cuvettes.....	64

Figure 49 - Acquisition setup for the buffer transmittance response. PC, on the left, camera for placing the buffer, in the middle, and light source and spectrometer, on the right, connected to the camera by optical fiber.....	65
Figure 50 - Radiation flux in microchannel.	67
Figure 51 - Graphical representation of the intensity on the 6 channels of Adafruit AS7262 using a white optic fiber light source.	70
Figure 52 - Setup to measure pH values. A pH meter from inoLab in measuring the pH and temperature conditions of buffer solution in a test tube with a stirrer, placed in an IKA RCT basic magnetic stirrer.....	71
Figure 53 - Transmittance Spectra of complete buffer solutions at different pH levels, obtained with the software OceanView.....	72
Figure 54 - AutoCAD design of the 1 mm chamber to study the transmittance level for different buffer solutions.	74
Figure 55 - (a) Method of inserting the glue with a small needle to fix the optical fibers on the chip; (b) fixed optical fiber so that the waveguides are directed to the microchamber; (c) the 1 mm microchamber PMMA microchip with the optical fibers.....	74
Figure 56 - Setup for the transmittance measurements on the microchamber. The buffer solutions go to the microchip in continuous flow during the whole measurement through a micropump with a frequency near to 100 Hz. The waste liquid is discarded into a beaker.....	75
Figure 57 - Intensity of Adafruit AS7262 6-channels for experiment performed for buffer solutions with pH 5.8, 6.4, 7.0, 7.4, 8.0, respectively over time. The experiment is done by alternating the reference sample, pure water, and buffer solutions, in the 1 mm chamber. Each step corresponds to the response of the buffer solution in relation to the water response (maximum observable value).	75
Figure 58 - Transmittance of channels violet and green of Adafruit AS7262 for experiment performed for buffer solutions pH 5.8, 6.4, 7.0, 7.4, 8.0, respectively over time. The experiment is done by alternating the reference sample, pure water and buffer solutions, in the 1 mm chamber. Each step corresponds to the response of the buffer solution in relation to the pure water response (maximum observable value).	76
Figure 59 - Transmittance response of channels violet and green of Adafruit AS7262 for pH 5.8 - 8.0 range. The experiment is performed for buffer solutions pH 5.8, 6.4, 7.0, 7.4, 8.0, in the 1 mm chamber, which is done by alternating the reference sample, pure water and buffer solutions.	77
Figure 60 - Expected theoretical response (T) and experimental transmittance response (TP) of green channel of Adafruit AS7262 for pH 5.8 - 8.0 range. A polynomial approach is made to study the error between what is obtained and what is expected, through polynomial equations. The experiment was performed for buffer solutions pH 5.8, 6.4, 7.0, 7.4, 8.0, in the 1 mm chamber, which is done by alternating the reference sample, pure water and buffer solutions.	78
Figure 61 - AutoCAD design of the 2 mm chamber to study the transmittance level for different buffer solutions.	79
Figure 62 - Intensity of Adafruit AS7262 6-channels for the experiment performed with buffer solutions of pH 5.8, 6.4, 7.0, 7.4, 8.0, respectively, and over time. The experiment is done by alternating the reference sample, pure water and buffer solutions, in the 2 mm chamber. Each	

step corresponds to the response of the buffer solution in relation to the pure water response (maximum observable value).	79
Figure 63 - Transmittance of channels violet, blue, green and yellow of Adafruit AS7262 for experiment performed with buffer solutions pH 5.8, 6.4, 7.0, 7.4, 8.0, respectively, over time. The experiment is done by alternating the reference sample, pure water and buffer solutions, in the 2 mm chamber. Each step corresponds to the response of the buffer solution in relation to the pure water response (maximum observable value).	80
Figure 64 - Transmittance response of channels violet, blue, green and yellow of Adafruit AS7262 for pH 5.8 - 8.0 range. The experiment is performed for buffer solutions pH 5.8, 6.4, 7.0, 7.4, 8.0, in the 2 mm chamber, which is done by alternating the reference sample, pure water and buffer solutions.	81
Figure 65 - Expected theoretical response (T) and experimental transmittance response (TP) of green channel of Adafruit AS7262 for pH 5.8 - 8.0 range. A polynomial approach is made to study the error between what is obtained and what is expected, through polynomial equations. The experiment is performed for buffer solutions pH 5.8, 6.4, 7.0, 7.4, 8.0, in the 2 mm chamber, which is done by alternating the reference sample, pure water and buffer solutions.	82
Figure 66 - Noise signal of the channels of photodetector of Adafruit AS7262.	83
Figure 67 - Solutions 1, 2 and 3 prepared with red food coloring ink and pure water, 4:1, 8:1, 12:1, respectively.....	84
Figure 68 - Transmittance Spectra of red food colouring ink solutions 1, 2 and 3, obtained with the software OceanView.	84
Figure 69 - Transmittance obtained with the sensor for experiment performed with red food coloured ink solution, first, second and third solution, respectively over time. The experiment is done by alternating the reference sample, pure water, and red food coloured ink solution, pumping the fluids using neMESYS syringe pump at a flowrate of 20 $\mu\text{L}/\text{min}$. Each step corresponds to the response of the solutions in relation to the pure water response (maximum observable value). .	85
Figure 70 - Transmittance Spectra of black food colouring ink solution, obtained with the software OceanView.	86
Figure 71 - Transmittance obtained with the sensor for experiment performed with black food coloured ink solution (black food colouring ink and pure water in the proportion of 1:10), over time. The experiment was done by alternating the reference sample, pure water, and black food coloured ink solution, pumping the fluids using neMESYS syringe pump at a flowrate of 20 $\mu\text{L}/\text{min}$. Each step corresponds to the response of the same solution in relation to the pure water response (maximum observable value).	86
Figure 72 - Transmittance obtained with the sensor without mirror for experiment performed with black food coloured ink solution (black food colouring ink and pure water in the proportion of 1:10), over time. The experiment was done by alternating the reference sample, pure water, and black food coloured ink solution, pumping the fluids using neMESYS syringe pump at a flowrate of 20 $\mu\text{L}/\text{min}$. The step corresponds to the response of the same solution in relation to the pure water response (maximum observable value).	87
Figure 73 - Transmittance obtained with the sensor for experiment performed with buffer solutions pH 5.8, 6.0, 6.2, 6.4, 6.6, 6.8, 7.0, 7.2, 7.4, 7.6, 7.8 and 8.0, respectively, over time. The experiment was done by alternating the reference sample, pure water and buffer solutions, in the 1 mm chamber, pumping the fluids using neMESYS syringe pump at a flowrate of 20 $\mu\text{L}/\text{min}$.	

Each step corresponds to the response of the buffer solution in relation to the pure water response (maximum observable value).	88
Figure 74 - Sensor transmittance response over the range pH 6.0 - 8.0, with a sensitivity of 1.7%/0.2 pH and a linear regression that shows an accuracy around 94%	89
Figure 75 - Interface aspect for (a) solution with pH outside the pH 6.0-8.0 range, and for (b) the zero level (pH=6.0).	90

List of tables

Table 1 - Main physicochemical PMMA characteristics (Altuglas International, 2006).....	35
Table 2 - Properties of the used Zecha tools to mill.....	39
Table 3 - Optical characteristics AS7262 (Pass Band). (ams AG, 2016)	47
Table 4 - Tech Specifications Of Micro Arduino board. (AG, 2014)	49
Table 5 - Phosphate buffer for different pH values (Works, 2018)	63
Table 6 - Optical features of DH-MINI Ocean Optics UV-VIS-NIR Fiver Optic Light Source (Ave, n.d.).....	65
Table 7 - Measured transmittance for buffer solutions with different pH in a 1 cm cuvette and forecast for 1 mm and 2 mm microchamber.	69
Table 8 - Measures of pH with prepared buffer solutions with error associated and temperature conditions.	71
Table 9 - Transmittance in two peaks of transmittance spectra for the buffer solutions.....	73
Table 10 - Transmittance and absorption values for the buffer solutions in the pH range 6.0 - 8.0, with a step of pH 0.2 obtained with the sensor.	89

List of abbreviations

3D	Three-Dimensional
AU	Absorbance Units
CAD	Computer-Aided-Design
CAE	Calcein Acetoxymethyl Ester
CAM	Computer-Aided Manufacturing
CDA	Clean Dry Air
CNC	Computer Numerical Control
CTAB	Hexadecyltrimethylammonium Bromide
EGFET	Extended-Gate Field Effect Transistor
FET	Field-Effect Transistor
FWHM	Full Width at Half Maximum
GPTMS–ETEOS	3-glycidoxypropyltrimethoxysilane – rthyltriethoxysilane
HPTS	8-hydroxypyrene-1,3,6-trisulfonic acid
HPTS-IP	8-hydroxypyrene-1,3,6-trisulfonic acid – Ion Pared
IC	Integrated Circuit
IDE	Interdigitated Electrode
IR	Infra-Red
ISFET	Ion-Sensitive Field-Effect Transistor
LED	Light-Emitting Diode
LWL	Light-Waveguide
MEMS	Micro-Electro-Mechanical Systems
MLCT	Metal to Ligand Charge Transfer
MOSFET	Metal Oxide Field Effect Semiconductor Transistor
NC	Numerical Control
NEMS	Nanoelectromechanical Systems
NIR	Near-Infrared
OoC	Organ-on-a-chip
pHe	Extracellular pH
pHi	Intracellular pH
PCB	Printed Circuit Board

PDMS	Polydimethylsiloxane
PI	Propidium Iodide
PMMA	poly(methyl methacrylate)
POC	Point-of-Care
PSP	Phenolsulfonphthalein
RE	Reference Electrode
RPMI	Roswell Park Memorial Institute medium
SE	Sensitive Electrode
SMT	Surface Mount Technology
USB	Universal Serial Bus
UV	Ultraviolet
VIS	Visible

Chapter I – Introduction

1.1. Objectives and Motivation

Interest in tumour pH started when the pioneering work of Otto Warburg implied that aerobic glycolysis was a characteristic property of malignant cells (Warburg, Posener, 1924). Warburg conjectured that the oxygenation supply of tumour cells was harmed, so that they preferentially metabolised via anaerobic pathways, generating large quantities of lactic acid. This metabolic pathway makes malignant tissue more acidic than healthy ones, which led to several experimental tests to measure tissue pH (Freeman et al., 1980). As a result, it is now established that at least some tumours have a more acid interstitial pH than normal tissues.

Organ-on-a-chip (OoC) systems are miniaturised microfluidic devices with 3D human organ or tissue replicas, designed to repeat the essential biological and physiological parameters observed *in vivo* (Ahadian et al., 2018). The OoC arisen as a practical platform for differentiated medicine and drug screening tests. The *in vitro* models with biomimetic compositions and functions are projected to take over the traditional static cell cultures. An entire system of interconnected organoid models with microfluidics, mimicking *in vivo* conditions, contribute to analyse multiple interactions between several organs.

Although an extensive multiplicity of OoC models have been created so far, there are still challenges in the incorporation of micro(bio)sensor systems for their continuous monitoring. Therefore, the *in situ* and continual measuring of the microenvironment parameters and the dynamic activities of the organs is still a critical technological issue. Additionally, automated and noninvasive proceeds are clearly favorite for the long-term monitoring.

Generally, the *in vitro* systems for biology and drug development involve low volume microdevices for the chemical signalling, microfabricated pumps, valves, electrochemical sensors for rapid metabolic assessment, advanced bioinformatics, integrated electronic control and many other components. The development of portable and integrated biosensing devices for real-time analysis, can offer significant advantages over current analytical methods. Integrated optics-based biosensors have become the most appropriate technology for OoC integration, due to their ability for miniaturization, high sensitivity, reliability, and their potential for mass production at low cost.

The main goal of this dissertation project, performed through a partnership between University of Minho (Portugal) and Jade Hochschule – Wilhelmshaven, (Germany), is to develop and optimize reliable and miniaturised optical pH sensors for cell culture media monitoring, has response to the

biological organoid activity, both tumoral and healthy tissues. Overall, the designed pH micro(bio)sensor has the potential to be integrated with OoC platforms for continuous monitoring of organ models during several days.

1.2. Structure

The present dissertation is divided into five main chapters, namely:

Chapter I where the objectives and motivation have been set out.

Chapter II refers to the survey of all literature considered important for the idealization of the optical sensor, from the type of sensors already existing for measuring pH, the cell culture medium used in cell culture practices and the study of the optical compost for transmittance measurements in 1 cm cuvettes and 1 and 2 mm microchambers.

Chapter III describes the entire sensor manufacturing process. It refers to the micro-camera, light source and photodetector technologies used, codes used in both signal acquisition and sensor user interface, materials and structure used.

Chapter IV leads through the procedures and experiments and the optical response measurements on 1 and 2 mm microchambers and the sensor. The work presented in these two last chapters (III and IV), represents the experimental work developed in Germany.

Finally, Chapter V presents the main conclusions, as well as the suggestions for future work.

Chapter II - State of the Art

2.1. Micro-Electro-Mechanical Systems (MEMS)

Miniaturization of devices and tools extends advantages as high portability and produce cost reduction since less material is required and consequently, resources are spared (Krimpenis et al., 2014). Thus, a continuous effort has directed the research and microfabrication strategies in companies and scientific facilities, to produce smaller parts and machine components.

Micro-Electro-Mechanical Systems (MEMS) is a technology used to create microscopic integrated devices. These devices are incorporated into systems that merge mechanical and electrical components. The creation of MEMS relies on the capability of establishing manageable, mechanical and moveable structures using integrated circuit (IC) processing technology (Grayson et al., 2004). MEMS can gather information through measurement methods, which can be mechanical, thermal, chemical, optical or magnetic phenomena, processed through the microelectronic components. The complementary micro-mechatronics and microsystems comprise the technology of microscopic devices, mainly those including parts with degrees of freedom of movement. Currently, they have been transposed to the nanoscale into nanoelectromechanical systems (NEMS) and nanotechnology (Zhu et al., 2020).

MEMS technology has developed gradually since the discovery of piezoresistivity (Smith, 1954) stimulated by the development of silicon sensors. The turning point for MEMS was a research paper dated from 1982 (Petersen, 1982), reviewing the use of silicon for mechanical structures. These investigations triggered the development of the first polysilicon surface micromachine MEMS device, cf. Figure 1.

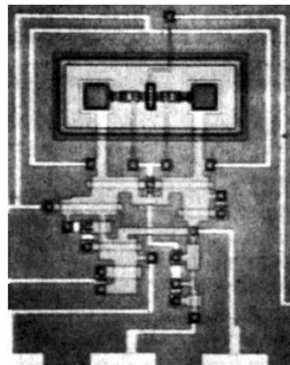


Figure 1 - First polysilicon surface micromachines MEMS device integrated with circuits (Howe & Muller, 1986)

The promising technology of MEMS has empowering microfluidic systems for many applications, such as micro chromatography, biochemical detection, and mass spectrometry (S. Wu et al., 2001). Nowadays, MEMS have evolved so much that they can be found in the most diverse applications such as in low-cost and energy-efficient hearing aid applications (Mallik et al., 2019), optical metamaterials (Ren et al., 2020), flow sensors (Ejeian et al., 2019), GPS future application improvement (Shen et al., 2019) and in MEMS sensors for Internet applications, namely as physical MEMS sensor, acoustic MEMS sensor, and gas MEMS sensor (Zhu et al., 2020).

2.2. Microfluidics

As mentioned before, MEMS has originated the conception and engineering of microfluidics, a multidisciplinary field that is largely used in engineering, physics, chemistry, biochemistry, nanotechnology and biotechnology, and whose products are often developed from computer-aided-design (CAD).

From chemical synthesis and biological analysis to optics and information technology (Whitesides, 2006), this technology can operate without any electrical connection, manipulating small amounts of fluid in channels, with dimensions in the order of few micrometers. As a consequence of its small size, low amounts of energy are needed and faster reactions accomplished. Thus, simple and portable devices can be manufactured. Also, these microfluidic systems are in general sealed, which prevent contaminations.

In biomedical or biotechnological applications, cells can be used and flow across a microchannel by a steady laminar flow, which is useful for extremely effective and precise cell manipulation. This advantageous function is important to incorporate microfluidic devices in on-chip biochemical and cell biological experiments (Yang et al., 2002).

The combination of MEMS and microfluidics has given rise to Fluidic MEMS. The first and highly successful MEMS devices, started with research involving a gas chromatograph (Terry et al., 1979) and inkjet printer nozzles (Bassous et al., 1977). This same technology has evolved, and in the present days, allowed the invention of implantable medical devices (Kubby, 2011) to monitor internal chemical concentrations and other properties, such as blood sugar levels, pH and oxygen concentration, as well as to precisely and continuously release dose drugs as-needed basis.

Presently, the microfluidic systems have already been combined with sensors to prepare integrated module solutions, able to read and analyse biological and physicochemical properties, the so-called lab-on-a-chip. Those take the utmost benefit of application in test development point-of-care (POC) devices (Rodrigues et al., 2015), such as portable and low-cost analytical devices, managing to eliminate conventional methods, as they can be mass-produced without losing their accuracy and reliability. Due to these advantages, they can be implemented in any place of the world, even in the most remote and undeveloped countries, allowing *in situ* reading and rapid analysis of many diseases (Harink et al., 2013).

Also, microfluidic devices offer advantages compared with classical cell culture systems, such as

temporal and spatial regulation of fluids and physicochemical parameters with the incorporation of sensors to acquire direct readings (Harink et al., 2013). These devices provide a high level of restraint, closed and convention-free vessels, which reproduces the environment that cells encounter *in vivo* (Son et al., 2012).

Therefore, lab-on-a-chip technology and microengineering attempts to offer a unique toolbox to be employed in cell biology and linked fields, through continuous-flow microfluidic devices, as exemplified in Figure 2.

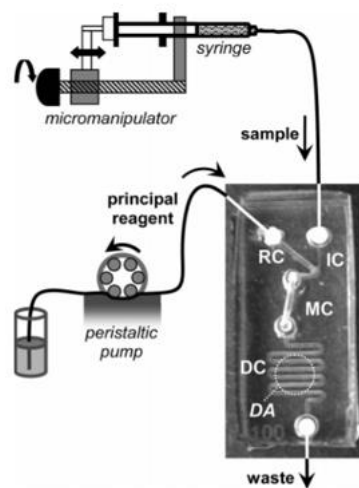


Figure 2 - Setup of a continuous-flow microfluidic device (Vullev et al., 2006).

2.3. Organ-on-a-chip (OoC)

The increase in the average life expectancy and the consequent aging of the population in the world, results in a growing demand for fast, reliable and *in situ* measuring of testing devices. Advanced microfluidic devices offer a new way to accelerate clinical research into diseases like cancer, where rapid drug development has been blocked due to large pharmacological and physiological gaps between cell culture monolayers, animal and human models (Edmondson et al., 2014).

The demand for advanced preclinical devices and treatment of diseases requires a full understanding of the biological and physiological complexity of human organs. From here, the organ-on-chip (OoC) platforms emerge, converging laboratory-on-chip engineering and cell culture, enabling the creation of multicellular organisms *in vitro* and its study. Among OoC potentiality as a preclinical tool, personalised medicine, drug development and toxicological screening are the most relevant (Y. S. Zhang, 2017).

OoC relies on the *in vitro* miniaturization of organs, representing one-thousandth or one-millionth less the size of an adult's human organs (Wikswa et al., 2013). OoC systems are microfluidic 3D miniaturized human organoid models, aimed to reproduce the vital biological and physiological parameters of the real human organs.

Several labs have been created effective tissues and organ models from human cells with functional and dynamic microvascular networks (Moya et al., 2013), having a major advantage of the pressure and fluid flow conditions that are easily controllable. These organ models and tissues are created from human cell lines, which are, in general, commercially available.

Depending on the application and the process of structuring the system, artificial organs, their validation and optimization vary. The modeling of these systems, in order to reproduce the organs *in vitro* under conditions of the actual physiognomy of the human being, is possible with the use of microfabrication, microelectronics and microfluidics. Besides, the microfluidic culture conditions are also appealing to fast fluid exchange in the cell microenvironment in an automatic and controlled way, as well as to control the cell surrounding over the time, which is excluded in standard cell culture microwells (Warrick et al., 2007).

2.3.1. Organ-on-chip sensing and control

Conventional sensing devices to control the cellular microenvironment are still difficult to integrate with microfluidic OoC systems, due to the low-volume bioreactors for continual monitoring (Shaegh et al., 2016). However, the micrometric structures have a huge surface-volume ratio, allowing the control of physical parameters at a higher level. Therefore, the attention that is being given to the development of these platforms is increasing. The OoC systems impart the integration of sensors to scrutinize the physicochemical properties of cultured organoids growing in the platform, maintaining a good microenvironment.

Meantime, human OoC models have been produced, as the four-organ Homo chippiens (i.e., mimic human body using a network of simulated organs, cf. Figure 3). However, studies on the inclusion of sensors are not yet sufficient for continuous real-time measurement, either to read microenvironmental parameters or to acquire the dynamic behaviour that organoids demonstrate in response to pharmaceutical compounds over the time. Besides, these platforms must have automated sensing potential for long-term monitoring (Y. S. Zhang, 2017).

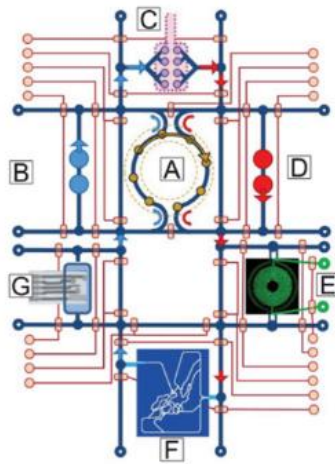


Figure 3 - A concept drawing of a four-organ μ Hu (Homo chippiens). (A) An on-chip peristaltic ventricular assist, (B) Right heart, (C) Lung, (D) Left heart, (E) Liver, (F) Peripheral circulation, (G) Microchemical analyser of metabolic activity. The system would work on a single microfluidic chip, with on-chip pneumatic valves controlling system functions and connections (Wikswow et al., 2013).

The interactions between organs place a severe restriction on the total and carrier circulating fluid. For this reason, it is crucial to develop the pump systems, valves, and analytical instruments in the microdevices design to study and maintain the physiological contributions within the normal parameter' values found in the human body (Ayuso et al., 2019).

One of the most important features to achieve a device with similar physiological parameters of the human body, is the volume of cell culture (mimicking blood supply) in proportion to the mass of cells. In other words, the total volume of fluid in OoC devices must be proportional to the total platform size, in the same proportion as between the volume of blood in the human body and its mass. (Wikswa et al., 2013).

Advanced cell culture platforms, such as OoC, must update various cell types while optimising physiological processes. Therefore, the monitoring of parameters related to the medium for cell culture can be seen as a focal point for the optimization of OoC.

To maintain the good working conditions of an OoC, the pH of cell culture media is a key parameter to be conditioned and observed. The pH must be kept within relatively narrow limits (pH 6.5 - 7.5)(Met, 1987), for the maintenance and growth of most cells.

2.4. Medium for cell culture

2.4.1. pH in cell culture medium

The chemical and physical conditions in the environment of cells may immediately determine or alter the cellular activities. Therefore, a major effort is made to study how to handle the appropriate conditions to maintain cells in active proliferation and growth. In previous observations (Absolonova et al., 2018) was observed that the changes in hydrogen ion (H^+) concentrations are related to the response of animal cells in the environments.

Broadly speaking, where a metabolic reaction involves H^+ as a reactant, there is a pH-dependence of the apparent equilibrium constant and related parameters, such as the free energy change and the pK_a value or the redox potential (Ullmann & Bombarda, 2013), cf. Figure 4.

In short, the pH scale is between 0 and 14. A solution is acid when the pH value is below 7 (neutral pH), while a solution is basic when the pH value is above 7 (Mohan, 2003). pH measurement is one of the most important parameters in biochemistry as almost all biological processes depend on the pH. In general, there are metabolic complications if a small change in the pH value occurs.

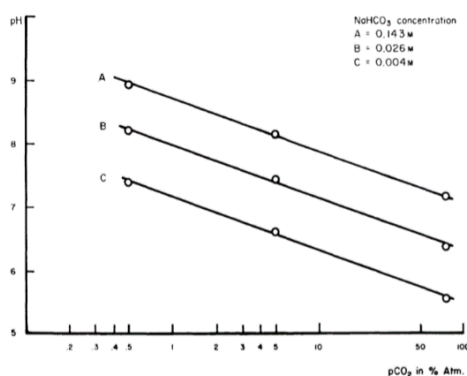


Figure 4 - Graph showing the relationship between pH and pCO_2 in three media. Solution A, bicarbonate enriched medium. Solution B, standard medium. Solution C, bicarbonate-deficient medium (TAYLOR, 1962).

The acidification of the extracellular medium (low pH_e) and the simultaneous intracellular alkalification of the cytoplasm (high pH_i) are important carcinogenic characteristics that cause the formation of an inverse pH gradient, manifesting themselves through the increase of activity of several plasmatic membrane carriers and acid efflux proteins that control the pH homeostasis (Aoi & Marunaka, 2014). This inverse pH gradient is connected to tumour proliferation (Gillies et al.,

2012). The cancer cells present $pH_i > 7.4$ and $pH_e \sim 6.7-7.1$ whereas normal cells show a $pH_i \sim 7.2$ and a $pH_e \sim 7.4$ (Webb et al., 2011, Persi et al., 2018). As mentioned before, these changes in the pH can be used to monitor cellular activity and identify abnormal cancer cells.

A range of cellular processes are correlated with pH_i changes, which occur during cell proliferation and secretion (Press, 1991). Since intracellular pH plays an important part in the transport of nutrients and enzymatic reactions in the cells, the regulation of intracellular pH is a fundamental physiological process of great significance to the growth and metabolism of cells, which in turn apply a lot of energy to the regulation of cytoplasmic pH.

Most animal cells in culture are grown close to a neutral pH (Ham & McKeethan, 1979), isogenic with the cytoplasmic pH, which has to be maintained within a narrow range for optimum growth of cells. Therefore, pH control is achieved through either the incorporation of buffers in the medium and/or replacement of the medium (Met, 1987).

2.4.2. RPMI 1640

For the *in vitro* cell culture, certain environmental conditions are necessary for cell growth and maintenance. Cell culture media are artificial gel or liquids that create an artificial environment for the cell activity and homeostasis. The selection of cell culture medium depends on the cell type and metabolic requirements.

Among cell culture media, RPMI (Roswell Park Memorial Institute) is a medium commonly used in cell culture. The complex media RPMI 1640, Figure 5, uses a bicarbonate buffer system (Ozturk & Palsson, 1990) and it is a medium that works for most types of mammalian cells (Shimizu et al., 2001), as in the growth of cells, when used with primary cells such as hematopoietic cells (Del Pup et al., 2003). It works with different cell lines if accurately complemented with serum, later serum replacements, or proper growth factor supplementation.



Figure 5 - RPMI 1640 from ThermoFisher (A) without phenol red and (B) with phenol red.

Moreover, the medium offers an advantage to pH monitoring by incorporating the colorimetric pH indicator, phenol red, phenolsulfonphthalein (PSP), often used in cell biology laboratories, typically in a concentration of 1.1 mg/L.

2.4.3. Phenol red

As mentioned above, phenol red is a water-soluble molecule, used as pH indicator in medium for *in vitro* cell culture. Its colour gradually changes from yellow ($\lambda_{\max} = 443 \text{ nm}$), corresponding to a pH 6.8, to red ($\lambda_{\max} = 570 \text{ nm}$), a pH of 8.2 (Mittal et al., 2009), and above 8.2 pH units becomes a bright pink colour.

Phenol red is a steady red crystal in air (Mittal et al., 2009) and behaves like a weak acid at 20 °C. It has a solubility of 0.77 grams per liter (g/L), when dissolved in water, and 2.9 g/L if dissolved in ethanol. In crystalline form or solution under extremely acidic conditions, the compound is established as a zwitterion (Belattar et al., 2018), cf. Figure 6.

This zwitterion form is written as H_2PS^- and has an orange-red colour. If the pH is above 1.2 pK_a , the ketone group loses one proton, resulting in the ion HPS^- , with a yellow tone. Higher than a pK_a of 7.7, the hydroxy group of phenol red loses its proton, creating the red ion, PS^{2-} . (Kazushige Sogawa, 1970)

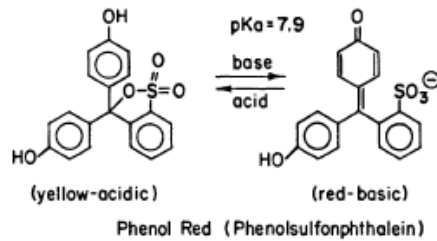


Figure 6 - Structure of phenol red (Berthois et al., 1986).

2.4.3.1. Phenol red as an indicator for cell culture

Most living tissues thrive at a near-neutral pH. For instance, the pH of blood has values between 7.35 and 7.45 pH units. Therefore, to grow cells in tissue culture is necessary to have a medium with the pH corresponding to its normal physiological value.

To control the pH of the medium, a small amount of phenol red is added, giving a pink-red colour under normal conditions (cf. Figure 7, at pH 7.4) (Ian Freshney, 2015). The colour change of the indicator, to yellow, is due to the acidification of the medium, which occurs in case of problems in the cells such as accumulation of metabolic sub-products produced by them. In the case of cancer cells, they present excessive amounts of glycolysis that produce high lactate (Granja et al., 2017), or when they are dying or have an excessive growth of contaminants.

The colour change, which can be identified with the naked eye, is an accessible way to rapidly verify the health of the tissue cultures. Even without cancer cells in the medium, the change of colour from pink-red to orange or yellow indicates that the medium must be replaced, so cells are maintained in optimal conditions (Phelan & May, 2017).

This colorimetric indicator is promising in the application of cancer detection, being used as an assistant in identification the interface between the cancer and normal tissue.

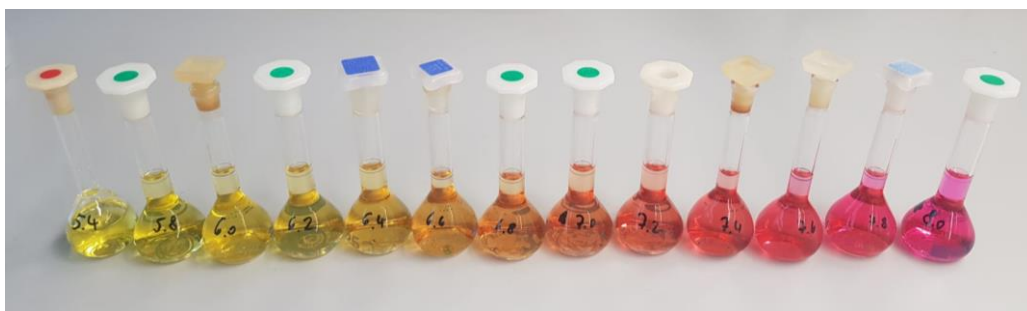


Figure 7 - Phosphate buffers (100 mL) with phenol red (concentration of 1.1 mg/L) for different pH values.

2.5. pH sensors

The boom in biotechnology has helped the rise of several industrial processes based on cell and microbial culture, translated in an enormous number of bioprocesses at the laboratory scale and enhancing the development and optimization of the final process.

To develop the processes of cell growth in medium, it is crucial the acquisition of data once it allows the monitoring of operating and performing of the experiments. As mentioned before, one of the key parameters of biotechnological processes is the pH value during cell culture, since cell behaviour is extremely sensitive to the surrounding microenvironment. Even in small changes of extracellular, pH can influence considerably the production of matrix macromolecules (Seifan et al., 2017, Kakkar et al., 2017).

Mainly, pH sensing can be realised by electrochemical or optical-based detection devices. In the past decades, a substantial effort was been done to develop electrochemical and non-electrochemical pH sensors for various applications.

In electrochemical methodology, electrodes prevent their use from being non-invasive, but the manufacturing process is relatively complicated. A matter of cross-chemistry between adjacent sensors (Suzuki & Akaguma, 2000) since the working and reference electrodes are always required. The phenomenon of signal drift dependent on the flow rate is a huge obstacle, due to interferences resulting from the compositions of the tested liquid (Kurita et al., 2002, Zhang & Chen, 2019). Due to these challenges, electrochemical sensors are not suitable for pH monitoring in a cell culture, in which its flow rate can be dynamic and molecules can interfere in the reading (Morris et al., 2009).

For this reason, many studies and projects are directed on the development of an optical-based pH sensor. Among the advantages, the optical pH sensors are low cost, resistant to electrical interference, viable for miniaturization and, most important, are a non-invasive sensing technique. In short, optical pH sensors are based on alterations in the spectroscopic properties of solutions, known roughly as absorption (Islam et al., 2016, Wu et al., 2007) or fluorescence (Gotor et al., 2017, Yadavalli & Pishko, 2004), due to pH variation. The following sub-chapters will describe pH, electrochemical and optical sensors. It will be discussed and clarified why non-invasive optical sensors, are a more promising type of sensors to be incorporated in an OoC, in comparison to electrochemical sensors.

2.5.1. Electrochemical pH sensors

In the area of electrochemical sensors, there is a vast literature on non-glass membrane pH sensor electrodes, which imply low cation interference with good measurement results at high temperatures. Unfortunately, this kind of electrode often shows a considerable redox sensitivity, causing them to deteriorate more rapidly. Nevertheless, the pH-response of these electrodes can rarely be explained with simple ion-exchange processes, which often includes pH-dependent redox equilibria (Gerischer, 1963).

An ideal electrochemical pH sensor of the ion-exchange type, must have certain common properties in their interfaces with external electrolytes, offering almost uniform composition surfaces, which permit rapid exchange of protons in the film or bulk phase, being an ionic semiconductor without electronic conductivity (Madou & Morrison, 1989)

Overall, a good working pH sensor must provide a stable phase over a wide temperature range, with uniform ion exchange capacity over the pH range and be independent of material oxidizing and reducing due to the reagents in the ambient media (Manjakkal et al., 2020).

The types of materials that are most used in the manufacturing of electrochemical pH sensors are glass (Pradela-Filho et al., 2020, Manjakkal et al., 2018), metal oxides (Ghadi et al., 2020, Jović et al., 2018), polymer or carbon (Alam et al., 2018, Joshi et al., 2017), Metal/Metal oxide (Manjakkal et al., 2020, Sadig & Cheng, 2020) and mixed-conduction oxides (W. D. Huang et al., 2011).

The sensors based on metal oxide are the most advantageous. Similarly to the glass electrode-based pH sensors, the metal oxide-based pH sensors, have a sensitivity close to Nernstian response, long lifetime and high accuracy. These also present fast response, low interferences to other ions, very low hysteresis, drift, and optical effects, easy maintenance and miniaturised size, as Metal/Metal oxide-based pH sensors. These sensors can be applied in flexible/wearable systems, as polymer or carbon-based ones, and are compatible with online monitoring applications. Nevertheless, this type of sensors demonstrates a slow response in basic solutions, causing large drift, hysteresis and optical effect (on ISFET based sensors). Another barrier of these sensors is that some materials show low accuracy and resolution, and others show a super-Nernstian or sub-Nernstian response (Kurzweil, 2009).

Within the electrochemical pH sensors based on metal oxides, it is important to highlight the

potentiometric pH sensor, the capacitive/conductimetric/inductive based pH sensor and the Ion-Sensitive Field-Effect Transistor pH sensor.

The potentiometric sensor comprises a combination of an sensitive electrode (SE), thick films in the form of nanostructures (nanowires, nanotubes or nanoflowers) (Manjakkal et al., 2020) and an reference electrode (RE), based on glass, immersed in a solution, deposited using screen printing on the same substrate, Figure 8(A), with its sensitivity determined by the difference in potential between the two electrodes. The conductivity method can be a simple two-electrode probe configuration in an electrochemical (Gill et al., 2008) cell configuration, i.e. an IDE on a substrate and screen printing deposition of a sensitive layer (Manjakkal et al., 2014), Figure 8(C). Unlike the potentiometric sensor, it does not use RE (Antohe et al., 2011) and the response to the electrochemical reaction that occurs at the solution-RE interface is measured by the change in electrical properties such as capacitance or impedance of the film deposited in the IDE.

In the ISFET pH sensors, the ISFET is formed directly on the FET (Field-Effect Transistor) electrode (Y. Qin et al., 2015). The gate is coated with a layer of oxide, ceramic, organic, polymer or composed of catalytic metals (Bergveld, 2003, Y. Qin et al., 2015), ion-sensitive, deposited between the source and the drain, detecting the pH (Wei et al., 2020).

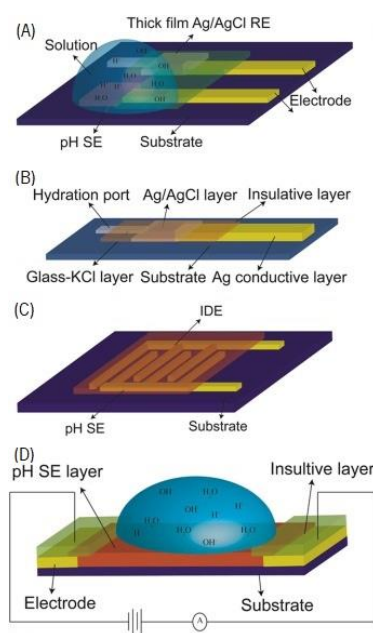


Figure 8 - Schematic representation of (A) potentiometric pH sensor fabricated by screen-print method, (B) thick film Ag/AgCl RE, (C) IDE based conductimetric pH sensor and (D) chemi-resistor (Manjakkal et al., 2020).

Even the metal oxide, the more advantageous electrochemical pH sensors, are not the best option to pH measurement because of their several disadvantages, as the potential deterioration by extended operation in distinct conditions, limiting its application, device instability, low current sensitivity, direct contact with the solution to be measured and sensitivity to light.

Although these disadvantages, electrochemical methods are still the most widely adopted techniques for pH sensing. However, mechanical fragility and the lack of flexibility/bendability hinder their implementation in emerging areas, such as wearable systems. Further, durability and performance instability at high temperatures and pressures, limit their use for pollution monitoring and other industrial applications. These drawbacks of the mentioned sensors have encouraged researchers to explore alternative ways to perform pH sensing.

For small applications, where the space and liquid volume are limited and agitation is vigorous, such as in OoC, the conventional electrode-type sensors used for monitoring biomodels, are impractical to implement. Besides, in the electrochemical sensors, the probes are inherently invasive, and the stringent sterility requirements are difficult to achieve and maintain (Kermis et al., 2003).

Additionally, the cost of instrumenting multiple small devices becomes unreasonable, since they are designed to be disposable. For these applications, there is a demand for sensing technology that is non-invasive, robust, compact and amenable to mass production.

2.5.2. Optical pH sensors

Potentiometry is the standard technique for pH measurement, due to its simplicity, reversibility, speed, precision and inexpensiveness. However, in some applications, optical sensors offer more advantages, namely, insensitivity to electrical interferences, electrical safety, lack of the need for a reference element, low-cost (Wu et al., 2009), better characteristics to measuring extreme pH values in low ionic strength solutions, even in the presence of organic matter (Capel-Cuevas et al., 2010), such as in OoC platforms.

In general, optical pH sensors are used for measurement and control of pH for applications in chemistry (Korostynska et al., 2007), biochemistry (Schäferling, 2016), clinical chemistry (Boysen et al., 2017) and environmental sciences (Alemohammad et al., 2018). New technological advances have made it possible to manufacture optical pH sensors with the most diverse

geometries, employing innovative planar detection platforms and using optical fibres (Gaur et al., 2018, Wencel et al., 2014).

Optical pH sensors are mainly based on changes in the structure of the indicator, which may be reversible, induced by a change in pH. These changes are a function of the acid or basic concentration, that the indicator has in the environment. Depending on the pH conditions of the study environment, the colorimetric indicator will have variations in its optical spectrum, and these can be analysed as variations in spectroscopic phenomena. In other words, the change in the optical properties of the immobilised reagents/dyes is measured with alterations of absorbance (Timbó et al., 2016, Worlinsky et al., 2015) or fluorescence (Rovati et al., 2018) signal. Still, there are optical sensors that are not based on acid-based indicators (Hasanah et al., 2019), such as sol-gel based optical pH sensors (Sørensen et al., 2019).

To be able to rely on a good functionality of a sensor, it must have a varied range of possible measurements. Hence, there are different strategies that have been studied and put into practice that have served to extend the range of work of optical pH sensors (Al-Qaysi & Duerkop, 2019).

In some approaches, the absorption of indicators conducts to wider ranges of measurements than the ones in solution, due to multi-layered adsorption (Barczak et al., 2016). For instance, the presence of different polymeric species of variable chain lengths and composed of different structural moieties that exhibit different pKa values, leads to a large pH range.

Particularly, conductive polymers change the absorption properties of indicators, in function of pH, both in the visible and near-infrared (IR) regions, such as polyaniline. Polyaniline based optical pH sensors consist of the formation of polyaniline films (Jin et al., 2000), (Q. Qin et al., 2010), with a pH range compatible with human physiology and without toxicity. Consequently, polyaniline optical pH sensors are suitable devices, because it presents large changes in λ_{max} and absorbance, allowing it to accurately measure blood pH (Gicevicius et al., 2019, Park et al., 2019), by monitoring the absorbance at λ_{max} (Abu-Thabit, 2018).

The analytical information required for correct sensing can also be done by imaging techniques through the preparation of detection membrane matrices containing complementary pH indicators (Gorji et al., 2019). A very important material to be mentioned is sol-gel materials, which have emerged as very versatile immobilization matrices for the optical detection of pH (Mahboubeh Vafi et al., 2019). Sol-gel matrices have many advantages, such as superior chemical and mechanical

stability, high optical transparency (Islam et al., 2019) and material versatility concerning coating and deposition techniques (Mersagh Dezfuli & Sabzi, 2019). Sol-gel materials simplify the immobilization of analyte-sensitive indicators, if physically covalently bonded. Thus, the indicator can be covalently bound to the polymer or sol-gel matrix (Barczak et al., 2016), which eliminates leaching effects.

Another approach in pH sensors development to broaden its dynamic range, consists of optical fiber format, via co-immobilizing of multiple pH indicators. This immobilization normally needs two spectroscopically fitting indicators with paired pH responses (Safavi & Bagheri, 2003), with selected pH zones distant from each other.

The fiber optic format used for manufacturing optical pH sensors has shown reliable results, as have similar innovative sensors based on a LED light source. These sensors can be miniaturised, are inexpensive, disposable and can be portable for *in situ* measurements. Due to these reasons for technological evolution and for the application in an OoC platform, the sensor for this study was an optical pH sensor based on the absorption and using a LED light source with a digital acquisition. In this chapter, optical sensors that work analogously with LED light sources and fiber optics are exposed in more detail.

Finally, for the projection and design of any sensor, it is necessary to think about its calibration. In the case of optical sensors based on absorption, which are advantageous for miniaturization and reliability, the functions used in the calibration derive from relations of the law of mass action between pH and intensity of radiation. Depending on its configuration and constituent materials, a sensor can use calibration with a single signal, absolute intensity measurements (Liu et al., 2017), with relative signals (Morsy et al., 2016) or standardised signals (Fonollosa et al., 2016) or through multiple intensity measurements, when measuring signals at more than one wavelength (Li et al., 2016).

2.5.2.1. Optical fiber based sensor

The measurement of pH by fiber optics, a waveguide that transmits light (John M. Senior, 2009) incorporated in a sensor, is now possible due to developments in the area of technological instrumentation. In general, the optical fiber can be glass optical fiber (GOF) and plastic optical fiber (POF) (Mitschke, 2010). POF is very flexible, and is therefore widely used in systems to

measure solution concentration and pH solution measurement (Yunus & Arifin, 2018).

An important strategy to expose the use of the fiber optic sensor was reported by Wu et al., 2009 (Wu et al., 2009), which is an optical fiber array-based sensor for online pH monitoring using microfluidic technology.

The system comprises a microfluidic chip, optical fibers arranged in pairs and placed on media, cf. Figure 9(a). The microfluidic chip, Figure 9(b), consists of a PDMS layer and a standard glass cover layer. The chip has detection cameras, Figure 9(c), setting up a flow system for high-performance online detection purposes.

The operating principle is established on the optical absorption of phenol red. The light source is a LED with a wavelength of 568 nm, making the systems to have only one individual detection unit. The optical fibers and the other to a photodiode. The fiber-optic illuminated light passes through the layer in the tested solution inside the detection chamber. The photon receiver then detects the unabsorbed light, Figure 9(d), that varies in intensity depending on the different pH values, since the optical spectrum of phenol red varies with pH. The simplicity of this non-invasive device makes it suitable for real-time pH monitoring.

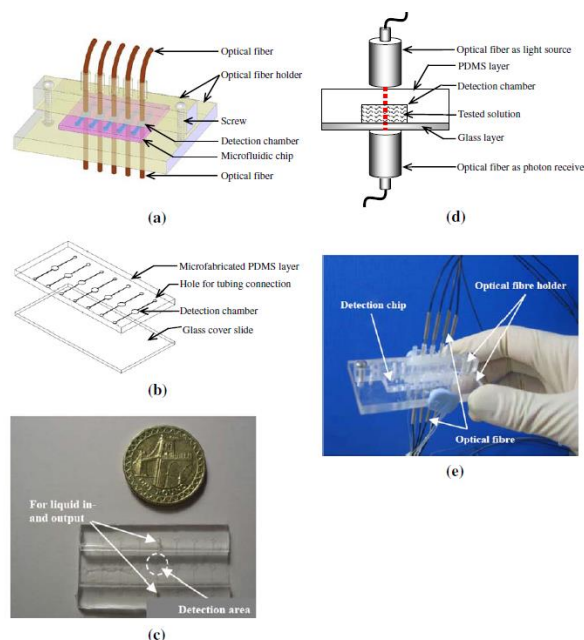


Figure 9 - Optical fiber array-based sensor: (a) schematic illustration of high throughput optical sensor array system, (b) the assembly of microfluidic detection, (c) the photograph microfluidic detection chip, (d) the illustration of each detection unit (cross-sectional view) and (e) the photograph of the assembled high throughput optical sensor array (Wu et al., 2009).

Another approach is the integration of plastic fiber optics in a loop as reported by Arifin et al., 2019 (Arifin et al., 2019). The optical fiber is dipped in buffer solutions with different pH values and the infrared LED light intensity, type IF-E91A with 950 nm wavelength, suffer energy losses caused by changes in the average refractive around the POF sensor. Consequently, the receiver, phototransistor type IF-D92, will receive a lower luminous intensity. The phototransistor is connected to differential amplifier, Arduino Uno microcontroller and computer. Therefore, with less light intensity recession, the output voltage reading in the microcontroller decreases. The same will be verified by reading directly on the computer.

The output light from the POF receiver is connected to a differential amplifier, which increases the electrical signal (analogic voltage) from the phototransistor. The receiver then connects to the Arduino Uno microcontroller, which converts the analogic signal into a digital signal transmitted to the computer. Hence, the result of the output voltage is read on the computer. The diagram of the pH sensor is shown in Figure 10.

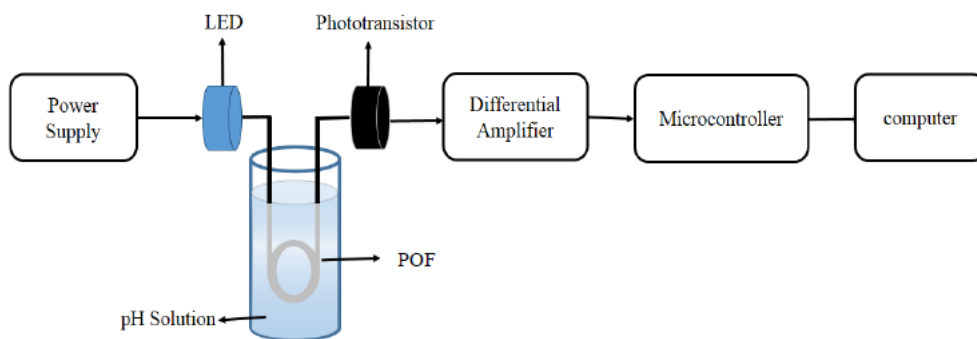


Figure 10 - Scheme of pH sensor based on POF (Arifin et al., 2019).

2.5.2.2. LED-photodiode microfluidic optical sensor

Conventionally, in microfluidic devices, samples are not analysed *in situ*. The entire process of transporting samples from the collection site to the laboratories is costly and time-consuming and can compromise the integrity of the sample, as there are risks of contamination during the handling process. Traditional fluorescence analysis systems use excitation sources such as argon, halogen, mercury or incandescent lamps (Yeh et al., 2017). These lamps require high power, produce a lot of heat and have to be modelled in wavelength through monochromators or light filters to block unwanted bands from their emission spectra.

In contrast, systems that use LEDs as light sources are stable, robust, inexpensive, and consume less energy. LED-based chemical detection and photodetector configuration make miniaturization and online detection a reality, as they can be integrated into microchips due to their small size and have a long lifetime (Novak et al., 2007).

Therefore, portable sensors have been developed for *in situ* pH measurement in aqueous samples (Perez De Vargas Sansalvador et al., 2016). These sensors incorporate microfluidic technology, allowing the use of small sample volumes and reagents. From this it is possible to create low-cost integrated detection systems, using LED as light source and photodiode as detector (photodiode) (Cogan et al., 2014, Czugala et al., 2013). Few still operate from microfluidic devices for colorimetric pH measurements (Florea et al., 2013). In this subchapter, an innovative Multi-analyte microfluidic optical sensor, reported by Shaegh et al., 2016 (Shaegh et al., 2016) will be detailed:

The pH detection is done on a single PMMA chip, which allows the connection to the bioreactor, cf. Figure 11, while the medium moves through the detection module. Likewise, in this sensor, the detection is based on the level of light absorbed by the phenol red in the culture medium, which is a function of the pH. As already mentioned, the colour of the colorimetric indicator is known to change from red to yellow when the pH becomes acid, respectively.

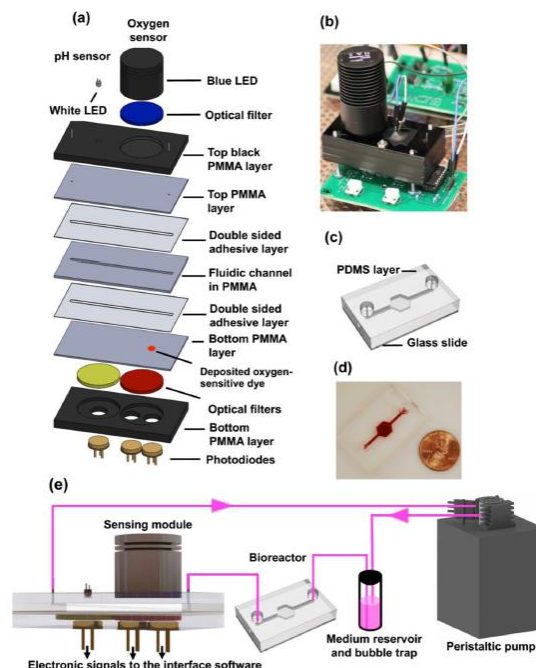


Figure 11 - Fabricated devices and test setup. (a) Exploded view of the sensing module for pH and oxygen measurement, (b) photograph of the fabricated sensing module, (c) schematic of the bioreactor, (d) photograph of the fabricated bioreactor, (e) schematic of the sensing module integrated with a peristaltic pump, culture medium reservoir, and bioreactor in a fluidic system (Shaegh et al., 2016).

The optical path is defined by the height of the fluidic channel. The LED light source is placed above the detection chamber and the photodiode (photodetector) under the chamber, thus detecting the amount of light that is absorbed by the medium, cf. Figure 12(a) and Figure 12(b). The Si photodiode is filtered by a long pass optical filter to quantify the amount of light absorbed by the light emitted by the LED, Figure 12(c) as a photodetector.

This sensor demonstrates that it is possible to create low-cut optical monitoring systems capable of being integrated into advanced microfluidic devices that include culturing cells, such as OoC platforms.

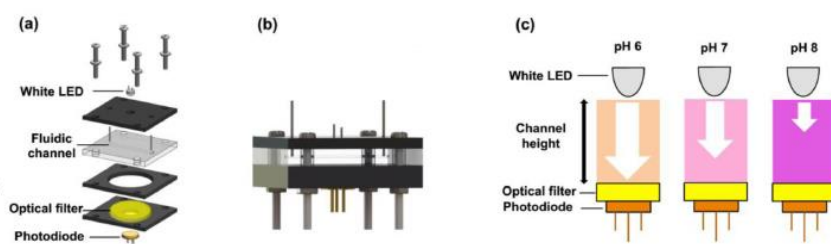


Figure 12 - Schematic of the fabricated fluidic detection chamber with integrated optical components: (a) exploded view (b) assembled view and, (c) schematic of detection level of light absorption in culture medium using solid-state optics (Shaegh et al., 2016).

2.6. Spectrophotometry concepts

2.6.1. Quantitative analysis of light

In 1870, Lambert observed that there was a relationship between the transmission of light and the thickness of the absorbent medium layer. When a monochromatic light feature (I_0) pass through a homogeneous transparent medium, each layer of the medium absorbs a fraction of light that pass through, regardless of the intensity of the light, which can be expressed as Equation 1:

$$I = I_0 10^{-k \cdot d} \quad (1)$$

where,

I is the intensity of the light that is emitted

I_0 is the incident intensity

k is the absorption coefficient and

d is thickness of the medium.

This concludes that the intensity of the light that is emitted (I) decreases exponentially as the thickness (d) of the absorbent medium increases.

Previously, in 1853, Beer observed that a certain solution absorbs light in proportion to the molecular concentration of the solute found in it. That is, the intensity of a monochrome light beam decreases exponentially as the concentration of the absorbing substance increases (Hughes, 1963).

The Beer-Lambert–Bouguer absorption law, or Beer's law, when it comes to the absorption in an optical medium, is precise only at power densities lower than a few kW. This law, at higher power densities, neglects the processes of stimulated emission and spontaneous emission (Kocsis et al., 2006). This is because at high photon flux, the processes of stimulated emission and spontaneous emission cannot be ignored. Since, its start to affect the population of the energy levels of the atoms (Abitan et al., 2008). Thus, the general absorption law, reduces the Beer's law for low power densities, Figure 13.

The laws of Lambert-Beer are treated simultaneously, a process in which the amount of light

absorbed or transmitted by a given solution depends on the concentration of the solute and the thickness of the solution.

Lambert-Beer's law can be expressed mathematically by the relationship described as Equation 2 (Swinehart, 1962):

$$T = e^{-a.d.C} \quad (2)$$

where,

T=Transmittance

e = Euler's Natural Logarithm

a = constant

d = Thickness of the solution

C = Solution concentration.

Converting the equation to logarithmic form, Equation 3:

$$-\ln T = a. d. C \quad (3)$$

Using logarithm on base 10, the absorption coefficient is converted into the extinction coefficient

k. From here follows Equation 4:

$$-\log T = k. d. C \quad (4)$$

where,

$$k = a/2.303$$

This can be expressed as the absorptivity, as following:

$$\frac{I}{I_0} = 10^{-\alpha.d.C} \quad (5)$$

$$A = -\log \frac{I}{I_0} \quad (6)$$

$$\alpha = \frac{4\pi k}{\lambda} \quad (7)$$

$$A = \alpha. d. C \quad (8)$$

where,

α is the molar absorptivity of the substance and

λ is the wavelength of the beam of light.

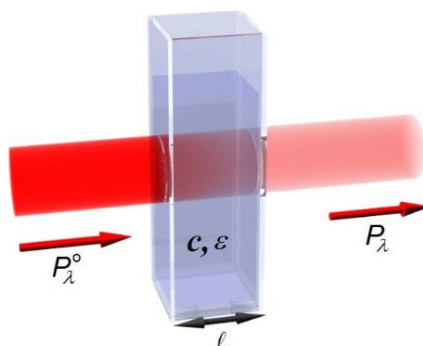


Figure 13 - Schematic of the decrease in radiant power of a monochrome radiation after crossing a cuvette of width, l , containing a solution with a concentration, c , in the component under study and a characteristic molar absorption coefficient, ϵ (Spencer Lima, 2013).

If d and α are known, the concentration of the substance can be determined from the quantity of light transmitted. The units of C and α depend on how the concentration of the absorbing substance is expressed (Wypych, 2018), and if the substance is liquid it should be expressed as a molar fraction. The units of α are the inverse of the length.

In short, the Lambert-Beer law explains that there is an exponential relationship between the transmission of light through a substance and the concentration of the substance, as well as between the transmission and the length of the body that the light passes through (Davies-Colley & Vant, 1987).

The correlation of the law between concentration and light absorption is the starting point for the use of spectroscopy to determine the concentration of substances in analytical chemistry (Axner et al., 2006). In the field of absorption spectroscopy, spectroscopists use absorption spectra as a technique to detect and characterize substances (Axner et al., 2006).

Spectrophotometry is a method used to measure quantities of chemical absorption, reading intensity when a beam of light passes through the chemical solution. The measurement is also used to measure the amount of a known chemical, once each compound absorbs or transmits light in a certain wavelength range.

2.6.2. Spectrophotometry measurements

The knowledge of light absorption by matter, is the most usual way to determine the concentration of compounds present in solution. All chemical compounds absorb, transmit or reflect light (electromagnetic radiation) at a certain wavelength range. Through spectrophotometry, the intensity of light is measured in wavelengths, and the components of a solution can be identified by their characteristic ultraviolet, visible or infrared spectra (Rojas et al., 1988).

The technique uses the property of the solutions to absorb or transmit light to quantify reactions. In practice, the amount of light absorbed or transmitted is proportional to the concentration of the substance in solution. The more concentrated the solution, the greater the light absorption is (Vogelmann & Evans, 2002). On the other hand, the color of the solution is determined by the color of the transmitted light.

The two most important concepts in spectrometry are transmittance and absorbance. Transmittance expresses the fraction of light energy that can pass through a certain thickness of a material without being absorbed (Woolley, 1971). In short, it expresses the capacity to transmit light. Absorbance expresses the fraction of light energy that is absorbed by a given thickness of a material, the capacity to absorb light (Gong & Krishnan, 2019).

Therefore, the absorbance is the intrinsic capacity of materials to absorb radiation at a specific frequency. Usually, such property is employed in the analysis of solutions in analytical chemistry.

In spectroscopy, absorbance is defined as Equation 9:

$$A_{\lambda} = \log_{10} \left(\frac{I_0}{I} \right) \quad (9)$$

The term absorption refers to the physical process of absorbing light, while absorbance refers to mathematical quantification. Absorbance only refers to the ray of light transmitted over incident light, not the mechanism by which the intensity of light decreases. This property is often treated as AU (Absorbance Units) (Srinivasan Damodaran, Kirk L. Parkin, 2010).

The absorbance of a solution is related to the transmittance. When the absorbance of a solution increases, the transmittance decreases. Transmittance and absorbance tend to be complementary magnitudes. Thus, its sum (for the same energy and incident wavelength) is approximately equal to 1, or 100%. If 90% of the light is absorbed, then 10% is transmitted (De Los Ríos & Fernández, 2014).

The measurement of the absorbance of a substance is performed in a spectrophotometer, usually performed in a solution. Then, a monochromatic light of the desired wavelength passes through a cell containing the sample, and another identical beam of light passes through a white one, filled with the same solvent as the sample, but without the substance being analysed (i.e., blank). A detector measures the intensity of the transmitted beams. Some equipment requires the blank to be measured before the sample, while others measure both simultaneously. Comparison with the blank, ensures that only the absorbance relative to the solute of interest is evaluated, and the absorbance of the solvent and losses, due to reflections in the cell, are discounted (Donald Voet, Judith G. Voet, 2016).

The longer the length crossed by the beam (optical path), the higher the absorbance, since the beam will interact with more particles of the attenuating substance. As the absorbance is a logarithmic measure of a ratio of luminous intensities, it has no dimensionality. The logarithm in base 10 generates the following relations, Equation 10 and 11:

Absorbance:
$$A = -\log_{10}\left(\frac{I}{I_0}\right) \quad (10)$$

Transmittance:
$$T = \frac{I}{I_0} \quad (11)$$

Therefore, in this study, by comparing the signal that is transmitted through the 1 mm chamber by the different samples and the reference sample, i.e., the blank, the transmittance fraction of each sample can be obtained. Thus, these different values of the transmittance fraction, corresponding to each sample, can be translated into the pH difference.

Since the buffer samples will have a colorimetric indicator, phenol red, the pH differences of each buffer in test will be translated into a different spectrometry response. Consequently, each sample with a different pH will have a different transmittance or absorbance level.

Chapter III - Development and implementation of the optical pH sensor

3.1. Microfluidic Chamber

At the macroscale, the milling process is very versatile and can create three-dimensional characteristics and structures. At the microscale, this process allows a fast and immediate fabrication of micro-molds and masks, enhancing the development of microcomponents (Friedrich & Vasile, 1996). The micromilling process ensures a high level of resolution and a small error of tolerance, at the microscale level (Geschke et al., 2004).

The operation of micromachining is mostly restricted to precision machining of two-dimensional microparts, normally performed on micro-electrical discharge machining or microlaser computer numerical control (CNC) machine tools. To achieve complex three-dimensional micro-geometries, micromilling can entirely use computer-aided design/computer-aided manufacturing (CAM) software abilities. Hence, both the movement and position of the tools are controlled by the computer. Optimization methodologies and generic algorithms can be coupled with CAM software, after following totally defining the parameters and related constraints of this process, resulting in a small calculation cost.

There is a direct correlation between the fragility and the size of the tools, since the smaller the tool is, the more fragile it will be, demanding more caution during the fabrication process. Therefore, due to the small size of the tool tip, it is quite difficult to detect wear on the cutting edges of the tool and its breakage. It results that it is more difficult to predict, since the technology of microscale sensors has limitations, as any technology.

The geometrical accuracy of microtools, which varies between approx. 5 and 10 μm , is a significant technological constraint (Krimpenis et al., 2014). A lower surface quality is obtained when the cutting edge of a standard microtool has a small damage. Thermal processes should also be performed on microtools through their manufacturing, and thus improving the microtool cutting performance (Cuypers et al., 2010). Besides, different grain sizes can be used for microtools amelioration, helping in the stability of the manufacturing process (Fleischer & Kotschenreuther, 2007).

3.1.1. The material selection

The success and growth of microfluidic technology applications depend directly on the material selection, which depends on the needs and conditions of those applications, samples, buffers and their polarities, design and budget.

For the development of this work the only material that was used was Plexiglass, also known as PMMA, acrylic glass or Plexiglas XT 0A000 (Figure 14).

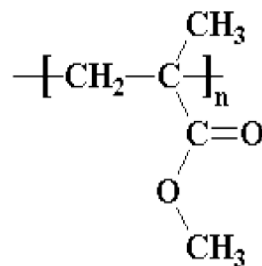


Figure 14 - Molecular structure of PMMA (Altuglas International, 2006).

PMMA is a typical substrate material used in microfluidics, due to its exceptional optical property, biocompatibility, appropriate strength and low cost (Hupert et al., 2007). Due to these advantages it was used as the target substrate in this work.

This material is a clear rigid plastic acrylic, transparent and colorless, which can replace glass. For these properties, its common usage goes from hockey rinks, signs and lenses.

It is a material produced by emulsion polymerization, solution polymerization or bulk polymerization. To produce 1 kg of PMMA, about 2 kg of petroleum is needed. PMMA has a temperature of ignition at 430 °C and burns. For this reason, PMMA is typically processed at 240 – 250 °C (Hupert et al., 2007). The moulding process applied to PMMA consists of injection, compression and extrusion moulding. In order to produce high quality PMMA sheets, cell casting is used, in which the polymerization and moulding stages take place simultaneously (X. Huang & Brittain, 2001).

PMMA is a strong, tough and lightweight material. It has a density of 1.17 – 1.20 g/cm³ (Pawar, 2016), which is less than half of glass. In addition to a high density, it also has better resistance. In addition, PMMA is a very transparent material, transmitting up to 92% of visible light (for plates with 3 mm thickness), and gives a reflection of about 4% from each of its surfaces due to its refractive index (1.4905 at 589.3 nm) (Bernini et al., 1992). Regarding the different types of

light other than visible light, PMMA is capable of filtering ultraviolet (UV) light at wavelengths below 300 nm, similar to normal window glass, allows infrared light to pass up to 2800 nm and blocks IR from longer wavelengths up to 25000 nm. Table 1 summarizes the main physicochemical characteristics found in PMMA.

PMMA has many good properties, however, it swells and dissolves in many organic solvents and also has poor resistance to many other chemicals, due to its easily hydrolysed ester groups. Even so, its environmental stability is superior to most other plastics, such as polystyrene and polyethylene (Barkoula et al., 2008).

Table 1 - Main physicochemical PMMA characteristics (Altuglas International, 2006).

Density (ρ)	1190 Kg/m ³
Forming Temperature	150 - 160 °C
Ignition Temperature	430 °C
Production	Extruded
Colour	Colourless and clear

3.1.2. Microfabrication

In this subsection, it will be presented the methodology used to make the microchannels by micromilling. The setup for the actual milling consists on a regular desktop with the software, the micromilling machine (*Minitex Mini-Mill/GX*) and a second monitor with the point-of-view of the microscope attached to the milling machine, cf. Figure 15. This process passes through three software, namely *AutoCAD*, *Visual Mill* and *Mach3*.

At first, the *AutoCAD* is used to draw the microchannel geometries. After the drawings, the files are exported for the *Visual Mill* software to program all the movements for the milling process, to post the code in “.nc”, making compatible with the final software, the *Mach3*. This *Mach3* tool is the one used to mill the microchannels.

In this chapter it will be also presented every detailed step, as well as the specifications of the milling material, tools, the assemble and cleaning, as well as the most common errors that occurred during the process of fabrication.



Figure 15 - Setup for Micromilling in *Fachbereich Ingenieurwissenschaften Labore Technische Optik&Mikrofertigung*, at Jade Hochschule.

3.1.2.1. Software Support

AutoCAD

Intending to design the microchannels, using *AutoCAD*, Figure 16, there are several aspects and steps to have into consideration:

- The drawing must start at the position (0,0)
- The scale used is 1 unit, corresponding to 1 mm in the scale used at the milling machine
- As the milling is done by parts, each of which has its polygon, it is mandatory to close all the polygons. Since, it is possible to do different conjunctions of polygons for the same design, making the path selection for the tools easier, while programming and saving time, once using different tools in the same channel
- Every inlet and outlet circles must be created with 2.1 mm of diameter
- At the end of the process, the file is saved as a “.dxf” format.

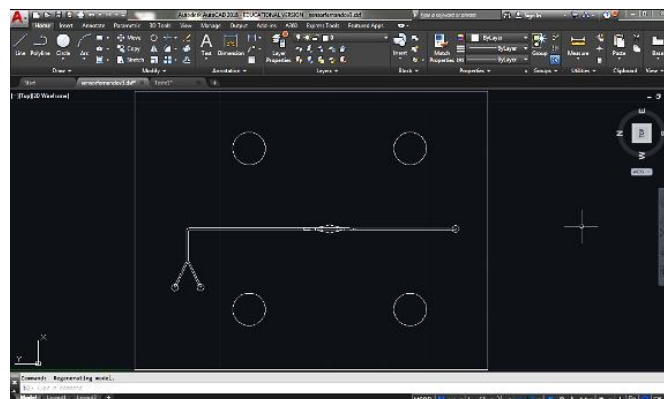


Figure 16 - Window of *AutoCAD* software.

Visual Mill - MecSoft VisualCAD

To program the movements of the milling machine, this software is used to define parameters as depth, velocity, angle, among others.

In this software some precautions and considerations must be taken to achieve the best possible results. One of the first considerations is that different milling tools have different heights, so the position z is different in the different tools. Another consideration is that the working table is not at the same level, so some parts are higher than others. Each stage of the milling process should have his file with their specifications, to optimize and review each step separately.

In Figure 17, it can be seen the aspects that need to be introduced on the development of the NC code. The other parameters already loaded from a previous database created by utilizing the company specifications, Zecha, for each tool.

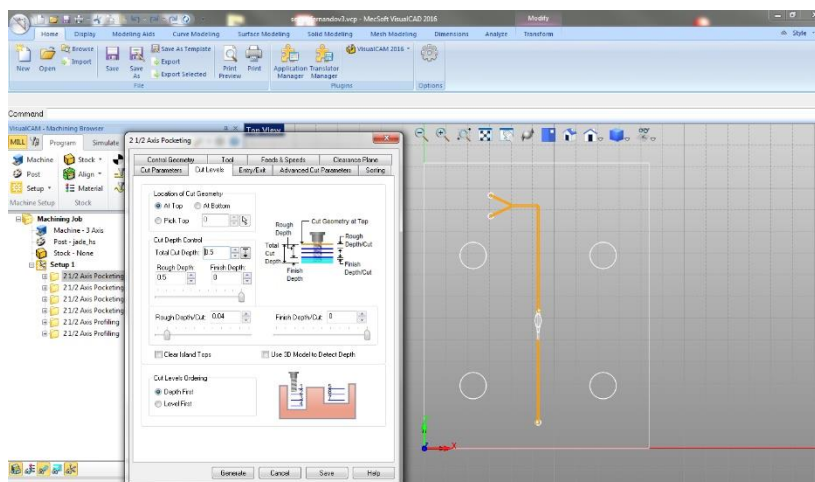


Figure 17 - Visual Mill window and its different properties.

At this stage, important steps need to be done, namely:

- Start with the middle size tool and organise the milling steps by tool size to optimise the process
- Change the smaller tool, if necessary
- Do the holes for the inlets and outlet and the lid cutting
- Save and post each configuration
- Check the time necessary for the actual production
- Close the *MecSoft VisualCAD*, so it does not interfere with the final software

After this process, the NC code is ready, and it should be functional on the *Mach3* software.

Mach3

This software reads the NC (numerical control) code and transpose those in the milling fabrication. The principal caution with this step to fabricate the microchannels, is the zero position, especially in the *z*-axis, since the tools have different sizes, as mentioned before, and this decides if the channel stays always with the same depth.

To achieve the zero position of each tool and to make sure that the depth of the microchannels has accuracy and high level of fabrication, it is necessary that the position of the tool is placed close enough to the channel, but avoiding to touch it, by slowly lower the rotating tool with the aid of the microscope. When this level of distance to the PMMA is reached, additional small increments in the movement of the tool, nearly 1 μm or less, is performed, stopping when the first touch is achieved, so we can assume in the software that is our zero position on the *z*-axis, as shown in the Figure 18.



Figure 18 - Mach3 window.

The process described is done for every part of the device, except for the inlets and outlets, because its zero *z*-axis is determinate in the middle of the PMMA.

The cooling agent utilised in this work was water with soap for the microchannels and compressed air for the lid. Additionally, the acrylic glass should be washed with water and soap with circular motions and blown with oxygen or air for drying.

3.1.2.2. Milling tools

One important aspect to have in consideration, is the mill tool size used in the drawing. For example, for a 100 μm drawing it should be used the 100 μm tool, or smaller.

The milling tools have in general available different diameters values for cutting, as shown in Figure 19.



Figure 19 - Tools used in micromilling of the company Zecha.

The milling tools are fragile, as mentioned before, and need to be handled carefully, since a simple touch with our fingers can break the tool.

Because every tool has its diameter, each one also has different working parameters that need to be taken into consideration to perform the milling, as listed in Table 2.

In this work, the 60 μm and 100 μm were used for the milling of the most of the microchannels, while the 1 mm was only used to make the inlets, outlets and to cut the lid.

Table 2 - Properties of the used Zecha tools to mill.

Tools	Depth/Cut [mm]	Feed rate [mm/min]
Zecha 0.06 x 0.12, 60 μm	0.01	80
Zecha 0.1 x 0.2, 100 μm	0.03	150
Zecha 1 x 2.5, 1000 μm	0.09	300 - 500

3.1.2.3. Pre-fabrication and checking

The fabrication of the microchannels must be pre-checked, to know if all the process will follow as expected. For this, a microscope Sensofar was used, as shown in Figure 20. Through this step the actual height of the microchannels and other fabrication parameters were evaluated.

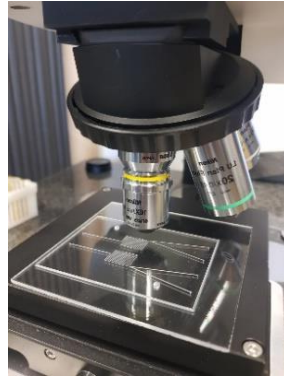


Figure 20 - Microscope Sensofar and the milled device.

The real image and the profile behavior of the microchannel features were analysed with the software *SensoSCAN*, as shown in Figure 21.

This pre-fabrication step and checking allowed to validate the fabrication conditions for the microchannels, with the ideal height of 0.3 mm, through the height profile in Figure 21(d). Also, this figure shows that the microchannel is milled with almost no roughness, presenting a smooth and clean structure.

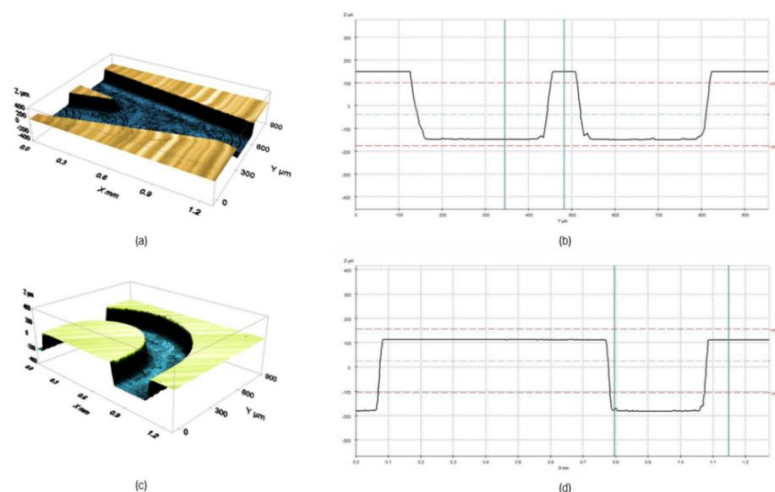


Figure 21 - (a) Zone of junction of the two liquids in a 3D bifurcation geometry, and (b) its corresponding profile; (c) first curvature where the liquids reach of the mixing area of the microchannel, in 3D, and, (d) its corresponding profile.

3.1.2.4. Fabrication of 1 mm chamber

The fabrication of a 1 mm pH-sensor reading chamber started with the milling of the microchannel with 0.5 mm in depth, with two inlets and one outlet, cf. Figure 22. Then, a chamber with a total depth of 1 mm was manufactured in three steps. The first has 0.5 mm, the second 0.7 mm and the third 1 mm (the expected value for the chamber). This created a smooth change in the depths between the channel (1 mm) and the microchamber (0.5 mm depth), and thus, less chance to create disturbances in the system, such as bubbles, which are prone to occur.

The design of the different depths for the fabrication of the microchamber does not need to be drawn in *AutoCAD*. As previously mentioned, this can be programmed on the software *Visual Mill*. Thus, only the 2D drawing of the device is done in *AutoCAD* software, as exemplified in Figure 22(a).

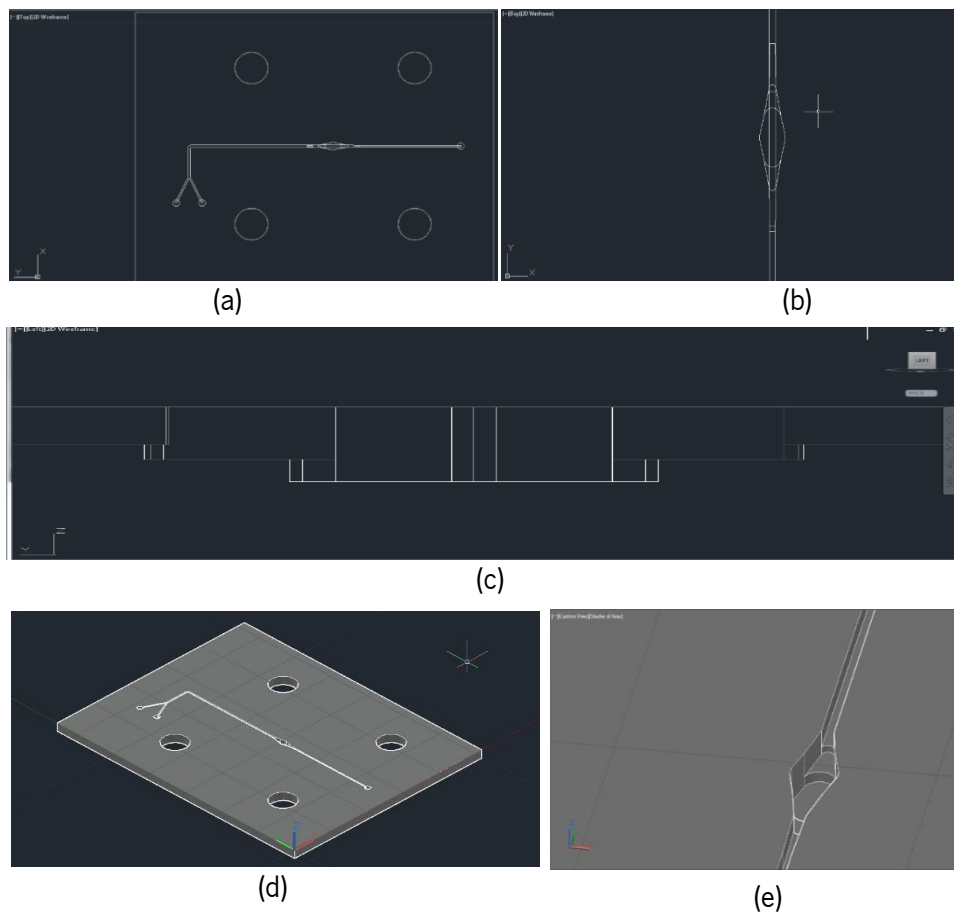


Figure 22 - Microchannel with 1 mm chamber designed by steps, (a) top view of the device, (b) top view of the microchamber, (c) side view of the microchamber, (d) 3D view of the device and (e) 3D view of the microchamber, all in AutoCAD.

3.1.2.5. Cleaning and sealing process

After the fabrication of the desired microchannels and chamber, the device has to be cleaned up with water and soap for glassware, and finally blasted with a compressed air gun. After that, the device is introduced on an ultrasonic machine for 20 minutes, where it is submerged on water with cleaning fluid. In this machine, the ultrasonic waves remove the remaining PMMA particles, improving the cleaning. Then, a final cleaning step is needed to clean the channel with water and soap. These first steps allow the fabrication checking, as briefly described in the previous sub-chapter 3.1.2.3.

After the confirmation of the depth, each in/outlet needs to be connected to a tube. Before assembling the tubes with the PMMA, a syringe is passed through the holes for an easy insertion of the tubes. The tubes should be inserted from the top to the entrance/exit of the channel.

A plasma pen is used to activate the surface, creating a good surface for the connection with Norland Optical Adhesive 68 glue (Figure 23), making it pass slowly by the microchannels area and tubes.

Finally, the channels are blown with CDA (Clean Dry Air) to dry the device and sealed with the adhesive film, by doing some pressure.



Figure 23 - Optical glue used to glue the tubes with PMMA.

The final microfluidic device designed with a 1 mm chamber to integrate an optical pH-sensor, is shown in Figure 24.

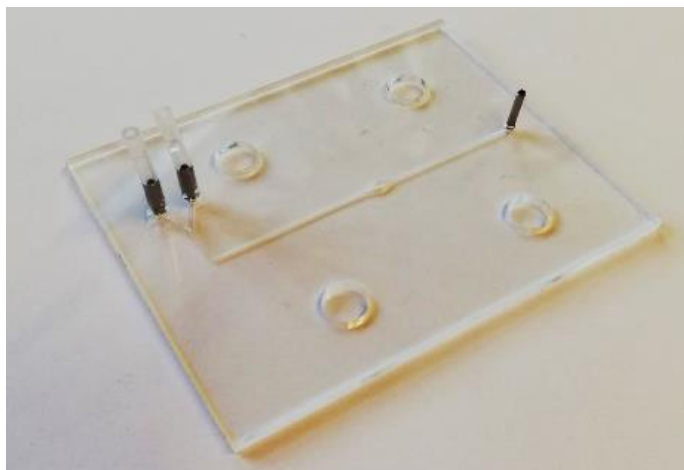


Figure 24 - Microfluidic devices with microchannels and a 1 mm chamber fabricated in PMMA assembled with connecting tubes.

3.2. Design of the photodetection system

3.2.1. Light source

A white LED from OSRAM, LW G6CP, was used as light source, an advanced power TOPLED, which features a compact package with a wide brightness range and high luminous efficiency. It has a white SMT package, colorless clear silicon resin, using the technology ThinGaN. The colour can be described as $C_x=0.33$, $C_y= 0.33$ (chromaticity coordinate).

The schematic of the basic circuit of a LED, Figure 25, was made on *Eagle* software and the board was then designed, Figure 26, with the appropriate dimensions, and manufactured the respective PCB with the LPKF machine that manufactures high performance from eagle design to finished prototype circuit board.

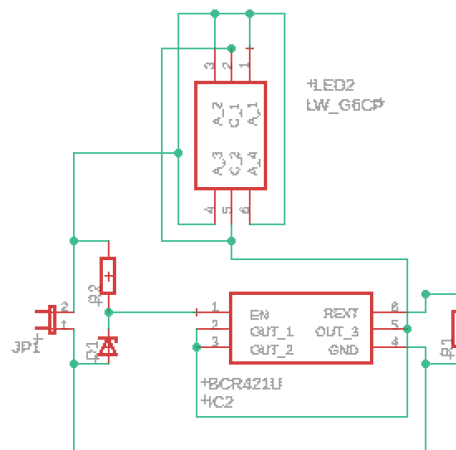


Figure 25 - Schematic of the source light on Eagle software.

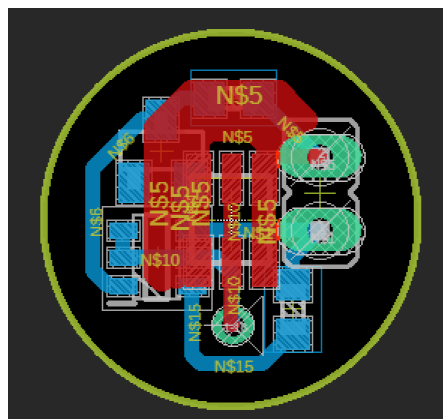


Figure 26 - Board design for the source light PCB on Eagle software.

The understanding of how the LED light beam affects the 1 mm chamber is achieved by viewing the image that is created by the beam when it reaches the chamber via a typical USB microscope camera, using the *sploview* program. This image, Figure 27(b), is followed by using optical filters, allowing the light to filter into its three components.

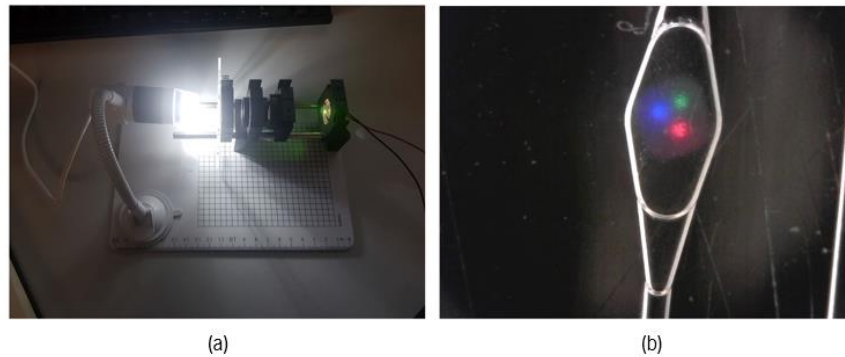


Figure 27 - (a) Apparatus with camera with brightness connected to a computer via USB, monitored in the software *sploview* interface, micro-camera, two optical filters 1/10 and 1/5 and LED on to obtain (b) the incidence behaviour of the 3 components of white light emitted by the LED.

The spectral response of the LED observed at Figure 28, was made using the spectrometer and the *OceanView* software. Two peaks are observed in the light intensity spectrum of the LED, for 456 nm and 565 nm, with more and less intensity, respectively. These observations are compatible with the LED datasheet.

This LED is suitable for the study of solutions with phenol red, because compared to the spectral response of the transmittance to the different buffer solution, with different pH, the sharpest peak is at 560 nm. Therefore, the peak with less intensity of the LED, is superimposed with the peak transmittance response of the solutions.

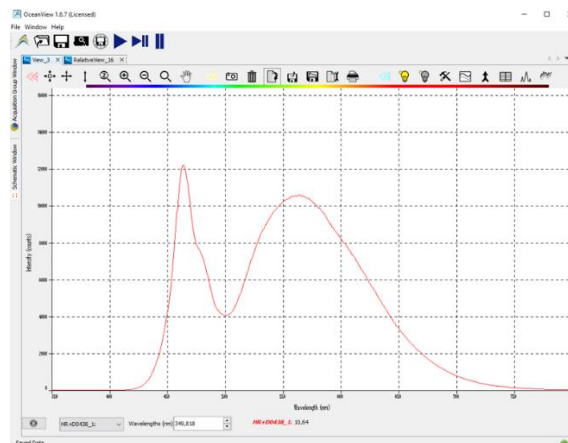


Figure 28 - Example of the spectra intensity of the LED obtained with spectrometry on *OceanView* software.

3.2.2. Photodetector

The photodetector used in the sensor was incorporated in the AS7242, a 6-channel visible spectral_ID Device with Electronic Shutter and Smart Interface. It is a code effective multi-spectral sensor-on-chip solution, sensing in the visible wavelengths from approximately 430 nm to 670 nm, a good range (2.88 eV – 1.85 eV) corresponding to the interval of transmittance response of the sample solutions in study (i.e, 560 nm). The AS7262 incorporates Gaussian filters into standard CMOS silicon via nano-optic added interference filter technology and is packaged in an LGA package that offers a built-in aperture to control the light entering the sensor array, cf. Figure 29.

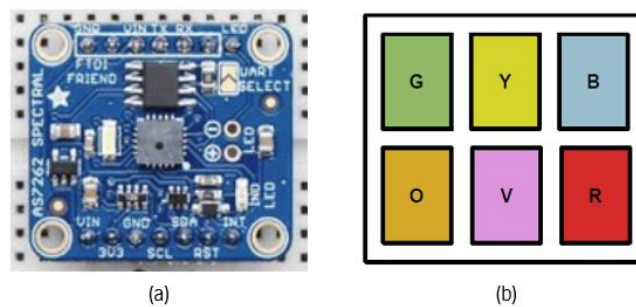


Figure 29 - (a) Adafruit AS7262 and (b) its photodiode array.

The compact 6-channel spectrometry solution features in the 450, 500, 550, 570, 600 and 750 nm, each with 40 nm FWHM.

It is a simple and easy device to operate, Figure 30, since no additional signal conditioning is required, using a 16-bit ADC with digital access. Also, it has low voltage operation, i.e., 2.7 V to 3.0 V. The control and spectral data access are implemented through I^2C register set.

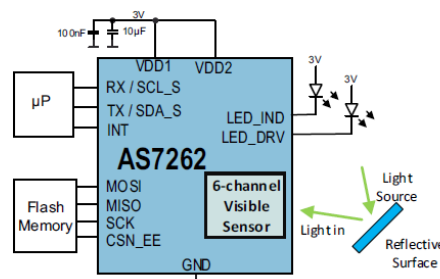


Figure 30 - AS7262 Visible Spectral_ID System. (ams AG, 2016)

The optical characteristics of AS7262, Table 3, are relative to calibration and measurements made using diffuse light, in each channel tested with GAIN=16x, Integration Time (INT_T)= 166 ms and

VDD=VDD1=VDD2= 3.3 V in an environment temperature of 25 °C. The accuracy of the channel counts/ $(\mu\text{W}/\text{cm}^2)$ is $\pm 12\%$. The source light used is a 5700 K white LED with an irradiance of $\sim 600 \mu\text{W}/\text{cm}^2$ (300 – 1000 nm). The energy at each channel (V, B, G, Y, O, R) is calculated with a ± 40 nm bandwidth around the center wavelengths (450, 500, 550, 570, 600 and 650 nm).

Table 3 - Optical characteristics AS7262 (Pass Band). (ams AG, 2016)

Parameter	Test Conditions	Channel (nm)	Min	Typ	Max	Unit
Channel V	5700K White LED	450		45		count/ $(\mu\text{W}/\text{cm}^2)$
Channel B	5700K White LED	500		45		count/ $(\mu\text{W}/\text{cm}^2)$
Channel G	5700K White LED	550		45		count/ $(\mu\text{W}/\text{cm}^2)$
Channel Y	5700K White LED	570		45		count/ $(\mu\text{W}/\text{cm}^2)$
Channel O	5700K White LED	600		45		count/ $(\mu\text{W}/\text{cm}^2)$
Channel R	5700K White LED	650		45		count/ $(\mu\text{W}/\text{cm}^2)$
FWHM			40	40		nm
Wavelength Accuracy				± 5		nm
Dark Channel Counts					5	counts
PFOV				± 20.0		deg

3.2.3. Software for signal acquisition using Arduino

The programming of Adafruit AS7262 is user-friendly in Arduino, as it has libraries associated with many predefined functions in the "Adafruit_AS726x.h" library. In this chapter is presented the explanation of the code of the acquisition chip for the photodetector signal (full code in Appendix II).

Briefly, the first lines of code allow the inclusion of two libraries. The "<Wire.h>" library allows us to communicate with I2C devices. The wire library implementation used 32-byte buffer; therefore, any communication should be within this limit, exceeding bytes in a single transmission will just be dropped. The "Adafruit_AS726x.h" library is a class that stores state and functions for interacting with AS726z spectral sensors.

To create the object ("ams") in the code it is used "Adafruit_AS726x_ams", therefore it is necessary a buffer "sensorValues [AS726x_NUM_CHANNELS]" to hold vales.

The main function of code is the "setup" function. In this code part the data acquisition baud rate is implemented in 9600 with the function "Serial.begin (9600)". The digital pin LED_BUILTIN is set as an output and if is not possible to connect with the sensor, an information will be processed to the user: "could not connect to the sensor! Please check your wiring".

If there is a connection with the sensor, the code will run the function "loop" with an integration time of 0.28 s. The function "setIntegrationTime" on the sensor object, allows the signal acquisition with an integration time of 2.8 ms multiplied by the number in this function.

To read the set, the LED with a current of approximately 10 mA, uses a cable connection with the LED of the chip, directly with the source light LED, so there is just the need to connect the USB cable if the MICRO Arduino is connected to the PC. Power implementation is just needed for the source light. The LED is turned on in the chip with the function "drvOn" with a 12.5 mA current, translated to the number 0 in the function "setDrvCurrent".

In the function "loop", the device temperature can be read, and the measurements are started with the function "startMeasurement". The values are read with the function "readRawValues" and at every 0.28 s is given an output of the intensity read in counts, on each of the 6 photodetector channels (violet, blue, green, yellow, orange, red), with the function "Serial.print(sensorValues[AS726x_VIOLET]", in the case of the violet channel and printed with the function "Serial.print".

3.2.4. Acquisition hardware and reading

In order to achieve the acquisition of the signal reading, it is necessary to connect the sensor to the computer and program it.

This sensor has four mounting holes and two header breakout strips. The power pins are Vin (power pin 3-5VDC), 3Vo (3.3V output) and GND (common ground for power and logic). The logic pins are SCL, SDA and RST. SCL and SDA are the I2C clock pins, connected to microcontrollers I2C clock line with a 10K pullup, level shifted to use 3-5VDC. The RST is the reset pin, which when pulled to ground the sensor rests itself. In the same way as the two other pins, RST is level shifted

to use the 3-5VDC logic.

The Micro board is based on the ATmega23U4 developed with Adafruit. It has 20 digital input/output pins (Figure 31), a 16 MHz crystal oscillator, a micro USB connection, an ICSP header, and a reset button. Every important tech specification of the board is listed on the Table 4. It contains all the information needed to support the microcontroller. This board is simply connected to a computer with a micro USB cable.

Table 4 - Tech Specifications Of Micro Arduino board. (AG, 2014)

Operating Voltage	5 V
Input Voltage (recommended)	7-12 V
Input Voltage (limit)	6-20 V
Digital I/O Pins	20
PWM Channels	7
Analog Input Channels	12
DC Current per I/O Pin	20 mA
DC Current for 3.3V Pin	50 mA
Flash Memory	32 KB (ATmega 32U4) of which 4 KB used by bootloader
SRAM	2.5 KB (Atmega 32U4)
EEPROM	1 KB (ATmega 32U4)
Clock Speed	16 MHz
LED_BUILTIN	13
Length	48 mm
Width	18 mm
Weight	13 g

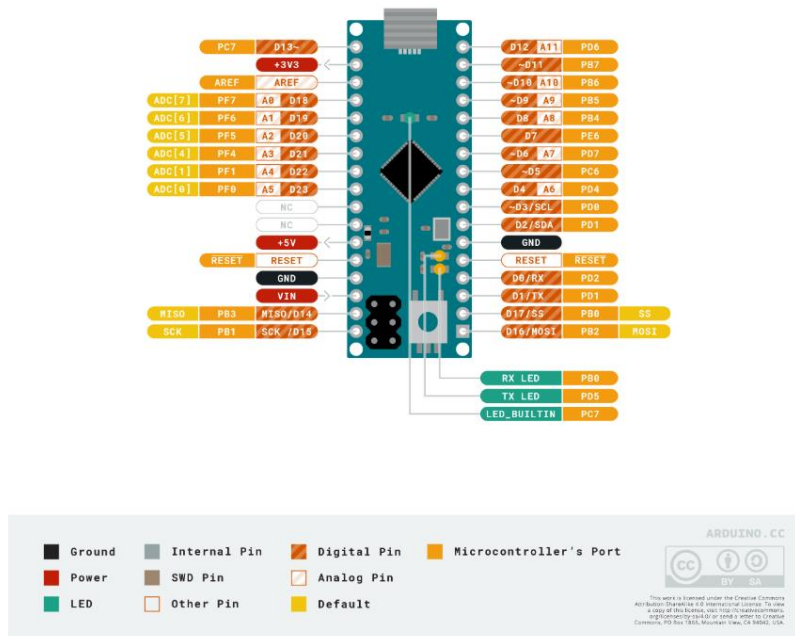


Figure 31 - Pinout Diagram of MICRO ARDUINO board, available on Arduino Store. © 2020 Arduino

For the acquisition of signal, there are four connections that need to be made between the sensor Adafruit AS7262 and the micro Arduino board. The Vin is connected to the power supply (pin +5 V), the same voltage that the microcontroller logic is based on. The GND is connected to common power/data ground (pin GND). The SCL is connected to the I2C clock SCL pin on Arduino (PD0), and the SDA pin to the I2C data SDA pin, on Arduino (PD1). The connections are made with welded wires in adapters for the Micro Arduino.

3.2.5. Holding the acquisition chip board

When the connection is made, it is necessary that the photodetector aligns directly with the light beam that comes through the optical fiber. The Adafruit AS7262 is placed in a PMMA holder designed in *AutoCAD*, cf. Figure 32, to be stable and the open photodetector be perfectly placed in the center of the holder.

To manufacture the holder, it is necessary that the height removed from PMMA is compatible with the height of the AS7262 dipositive PCB components. In order to have a close contact with the PCB. For example, in this study 1.6 mm of PMMA had to be removed, as there are parts on the used device with a height of 1.5 mm.

In micromilling, an air syringe is normally used to help remove PMMA residue from the surface

that was processed. In this case, the surface is needed with a very small roughness, to make sure it fits perfectly. Therefore, some oil is used on PMMA with the *Zecha* 1 x 2.5, 1000 μm tool. The 4 holes at the corners of the design shown in Figure 43 are a bit more open after the micromilling, using a 2.5 mm screw and oil, to make sure that the screws between Adafruit AS7262 and the holder are tightened without damaging the PMMA.

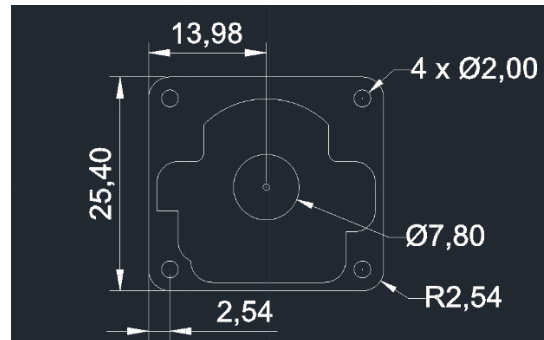


Figure 32 - AutoCAD design of Holder for Adafruit AS7262 with a hole representative of the photodetector entrance.

By using a microscope, Figure 33(a), the alignment is done through a pinhole placed above the photodetector, Figure 33(b). All these alignment components, microbank structures, are used in optical setups (black structures observed in the Figure 33). After the photodetector is in the center, it is possible to place an adapter for the optical fiber, Figure 33(c), that makes the light beam from the optical fiber and the photodetector be placed in the center. The setup is shown in Figure 33(d).

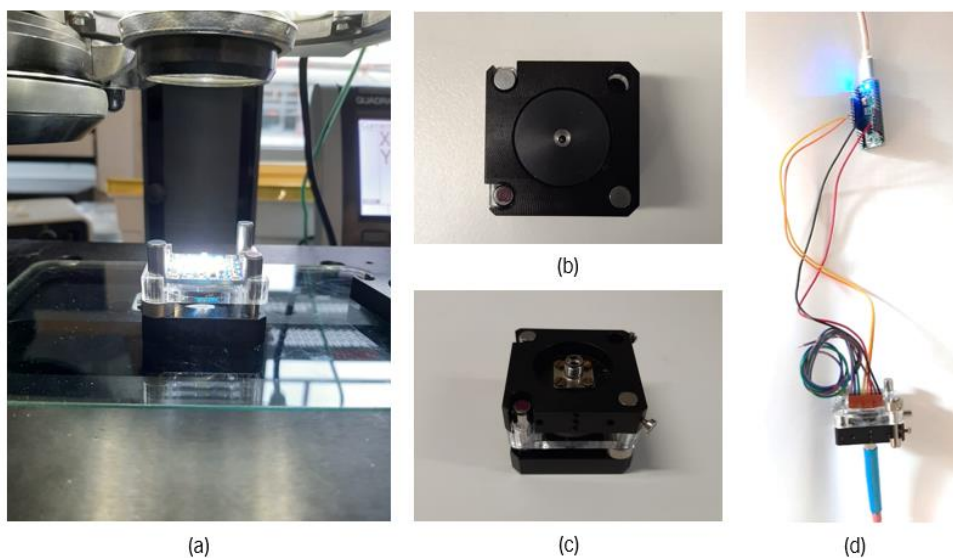


Figure 33 - (a) Microscope and the part to align. (b) Pinhole to align. (c) Adapter to connect optical fiber to Adafruit AS7262. (d) Setup to achieve the spectral responsivity of Adafruit AS7262.

3.3. Design of the Beam-splitter Sensor

3.3.1. Conceptual design

With the goal that the optical path, in the 1 mm chamber to be integrated in the pH sensor, is the same as the optical path in a 2 mm chamber, a configuration has been thought of, so that the light goes through the 1 mm microchamber twice. In other words, the light falls on the micro camera and when it reaches its extremity, the light goes the opposite way, so that we have the optical path doubled and thus more intensity in the values that can be measured by spectroscopy. To achieve this goal, a beam-splitter setup was thought.

In order to divide a beam of light into a multiplicity of parallel beams of equal intensity, the material used must have at least two blocks of light-transmitting isotropic material. These blocks must have one main face (incident input beam) coated to be partially transmissible and one silvery opposite face. These are arranged so that when the beam reaches the first block (input beam), it splits into a reflected part and a transmitted part. The transmitted part enters the block and after full internal reflection provides an output beam parallel to the reflected part of the first beam. Each subsequent block receives all parallel beams from the previous block, and so on (Partitioner, 1987).

However, in some applications, the beam splitter is presented with a single parallel-sided slab with a given coating. The material used in the coating varies along the length, causing the coefficients of reflection and transmission to vary, causing successive internal reflections, emerging in parallel and with equal intensity.

The technical drawing, Figure 34, shows apparatus for the sensor producing two parallel output beams of equal intensity from a single led beam.

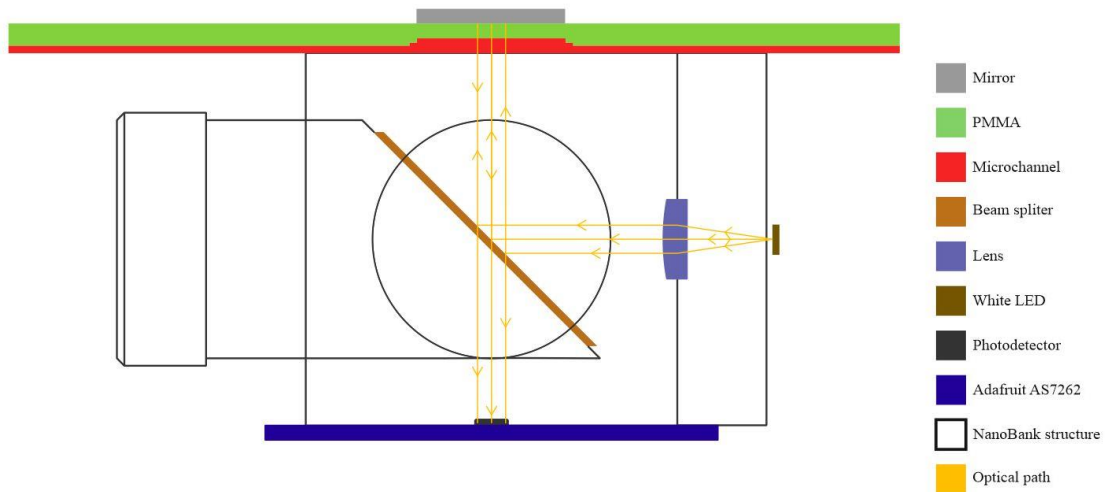


Figure 34 - Sensor conceptual design in *AutoCAD*.

The LED beam passes through a beam-splitter, which consists of a quarter wavelength retarder of 45° rotator, cf. Figure 35, which ensures that the beam reaches it and the light has equal S-polarised and P-polarised components. In this study it was used a beam splitter plate VIS-NIR, from *Qioptiq*, used for dividing or combining beam paths with a wedge angle to avoid multiple reflections. The material used in this beam-splitter is N-BK7 with rear surfaces broadband mirrored with ARB1. N-BK7 is a highly pure universal optical glass made by SCHOTT. It is one of the most common glasses used to produce high-quality optics, mainly for the visible spectrum. The relatively hard borosilicate crown glass consists of purest raw materials (Pcr & Kit, 2012). It is virtually free of bubble and inclusions and appears a clear colorless. The refractive index of this material is $n_{N-BK7} = 1.5168$.

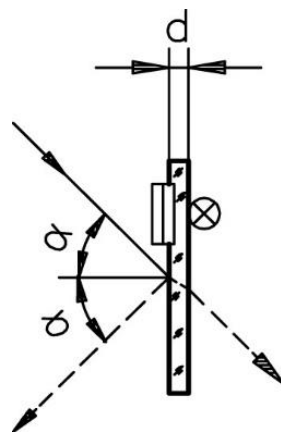


Figure 35 - Optical path diagram on beam-splitter with thickness d (Vis-nir, 2020).

The reflection and transmission are both equal with a deviation from each other of $\pm 5\%$ for an $\alpha=45^\circ$, unpolarised. The complete broadband of the beam-splitter is 450 - 1000 nm, as shown in Figure 36, with and uniform transmission in the visible.

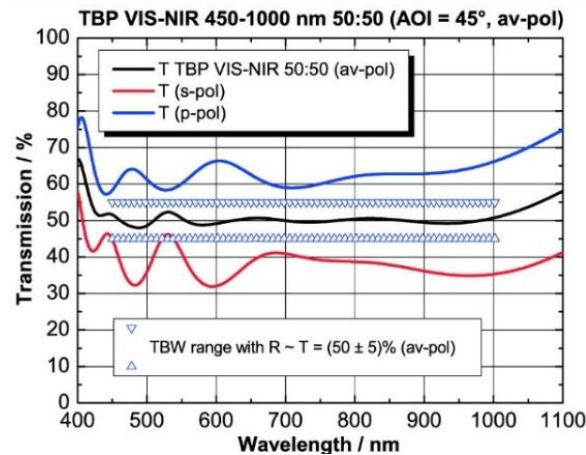


Figure 36 - Exemplary transmission for TBP VIS-NIR 50:50 for 450 - 1000 nm ($\alpha=45^\circ$; unpolarised) (Visnir, 2020).

3.3.2. Base structure

For the sensor structure, it was used the *NanoBank* structure provided by *Qioptic*. The basic cubic structure of the sensor is a type of cube used for compact three-dimensional, G050175000, Figure 37(a), which is used to install beam splitters, mirrors and prisms with 45° mirror brackets, as is the case to place the beam-splitter at 45° in the center of the cube's volume. The beam splitter holder, G050557000, is therefore installed in the cube with the beam splitter, G344140000, and glued together, cf. Figure 37(b).

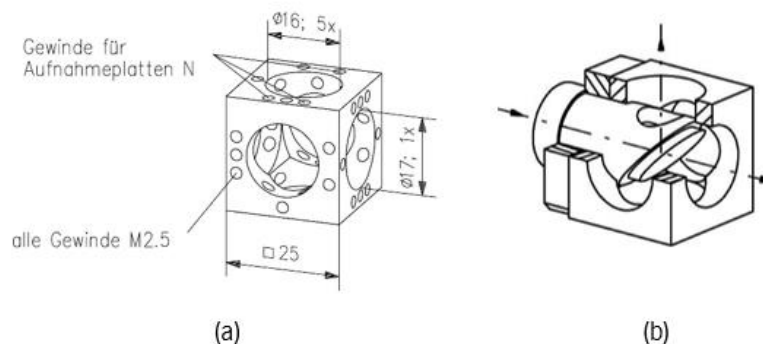


Figure 37 - a) Sensor structure base cube. (b) Function level of the beam-splitter support in the base cube (LINOS Microbench, Bench and Rail Systems, n.d.).

3.3.3. Lens and optical path

The optical path from the lens to the microchamber (image distance= v) is 25 mm, once the chosen cube side has exactly that length. The beam is directed from the lens, Figure 38, to the beam-splitter (12.5 mm optical path) and from the beam-splitter to the micro-camera (12.5 mm optical path).

To position the LED at a distance from the lens (object distance= u) such that the image distance is 25 mm, a study was performed using the software *WinLens3D Basic*. To carry out this study, it is necessary to understand the analytical and optical basis by which the distance of the object and the image are related to the chosen lens. By so, it was selected the lens with a 6 focal distance (F), G052003000, as illustrated in Figure 38.



Figure 38 - Achromatic lens with a 60 mm focal length in the holder.

When the object is located in front of the $2F$ point, the image will be located beyond the $2F$ point on the other side of the lens. Regardless of exactly where the object is located between $2F$ and F , the image will be in the specified region. In this case, the image will be inverted (i.e., a right side up object results in an upside-down image). The image dimensions are larger than the object dimensions, i.e. the absolute value of the magnification is greater than 1, cf. Figure 39. Lastly, a “real” image is created, whereas the light rays converge at the image location.

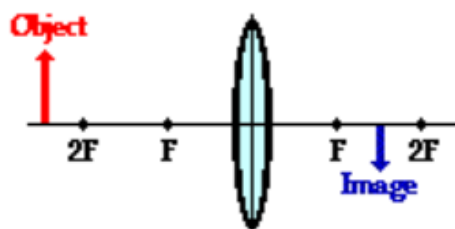


Figure 39 - Schematic of how the object and image meet concerning the lens.

The common Gaussian form of the lens equation is given by Equation 19.

$$\frac{1}{F} = \frac{1}{u} + \frac{1}{v} \quad (19)$$

From the study, full presented in Appendix IV, in the software *WinLens3D Basic*, to obtain an image distance of approximately 25.3 mm, the object distance is 6.5 mm. The calculated object distance can be achieved by integrating one framework holder (the same one that will be used for the LED - G061047000) between the LED and the lens.

The lens and LED are placed in holders, G061010000 and G061047000 respectively, with the size adapted to the lens, as seen in the previous Figure 38, followed by the PCB of the LED, then in the sensor setup with *Qioptic N* Mounting Plates, Figure 40, bolted to the base cube.

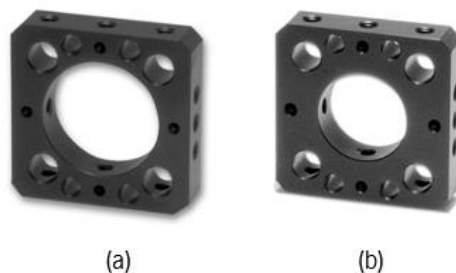


Figure 40 - *Qioptic N* mounting plates for (A) LED PCB and (B) lens.

The distance between the lens and the LED is set to 6.5 mm by means of a screwdriver, that adapts the LED.

After walking the optical path of approximately 25 mm, the light beam reaches the 1 mm camera and crosses the camera. The beam then crosses 1 mm of PMMA material and finally, it is reflected by a silver mirror placed on top of the PMMA chip. This way the optical path in the microchamber is doubled to 2 mm.

The biggest issues involved in this strategy, are stigmatism and aberrations anomalies, since the numerical aperture of the beam-splitter is very small due to two stops of light. These stops consist of two pinholes, metal plates with a 1 mm diameter hole to limit the numerical aperture of the beam. The pinholes are designed in *AutoCAD*, Figure 41, and cut in a laser machine. One of the stops is placed between the light source and the lens, and the other between the PMMA microchip and the mirror.

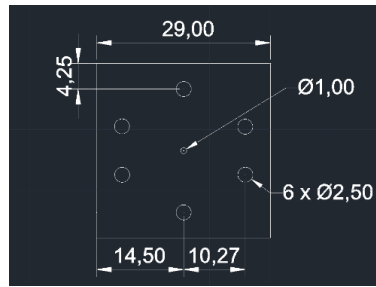


Figure 41 - AutoCAD design of pinhole (light stop).

3.3.4. Adaptation to Adafruit AS7262

To put Adafruit in the base structure it is necessary to make changes to its holder, since it happens a change in the optical path, Figure 42.

Therefore, Δn (optical path deviation) is due to the reflection of the beam in the mirror plus when it passes through the microchamber. This can be negligible and can be corrected with the repositioning and alignment of the beam-splitter holder, ensuring that the beam is focused on the Adafruit AS7262 photodetector. The Δ deviation is due to the diffraction of light that occurs in the change between the media (air and N-BK7). This shift can be corrected in the holder of Adafruit AS7262, and the shift of the beam Δ can be calculated through basic trigonometry and Snell's law.

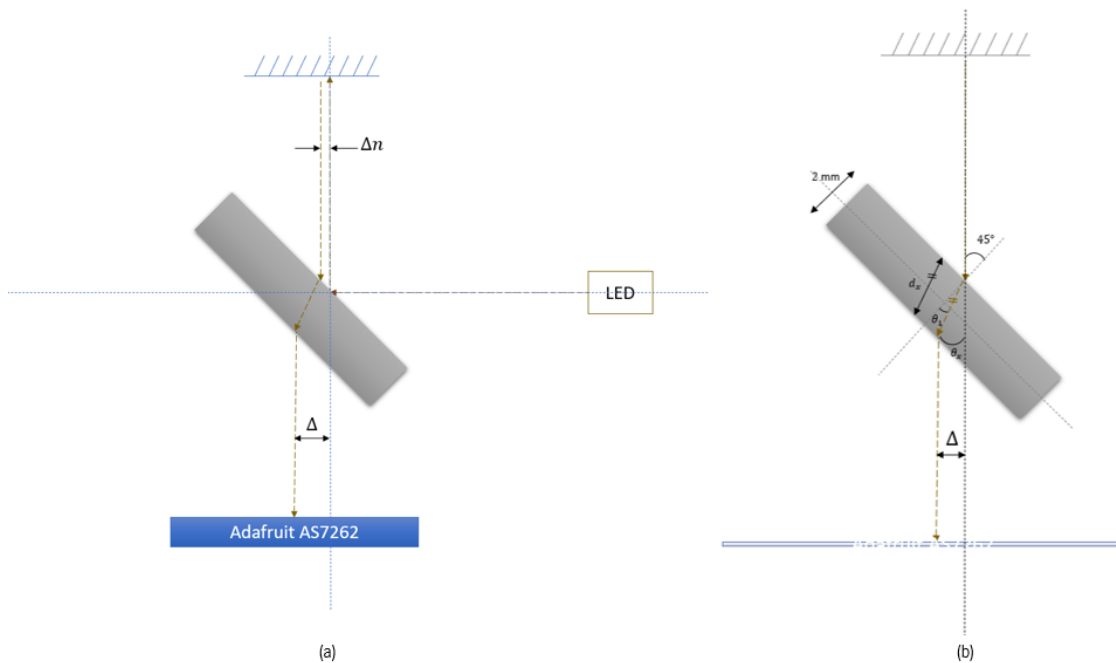


Figure 42 - (a) Schematics of the shift in the optical path. (b) Representation of not negligible optical path shift and fundamental trigonometry to calculate it.

$$n_{air} \sin 45^\circ = n_{N-BK7} \sin \theta_1 \quad (20)$$

$$n_{air} = 1$$

$$\theta_x = 45^\circ - \theta_1 \quad (21)$$

$$\cos \theta_1 = \frac{2}{d_x} \quad (22)$$

$$\sin \theta_x = \frac{\Delta}{d_x} \quad (23)$$

According to the presented equations (20 - 23), it is possible to calculate that the shift Δ will be approximately 0.65 mm. For this purpose, a 0.7 mm shift was performed on the front of the Adafruit AS7262 holder, with a new design in *AutoCAD*, cf. Figure 43, so that the photodetector, as well as the light beam, are deflected and aligned.

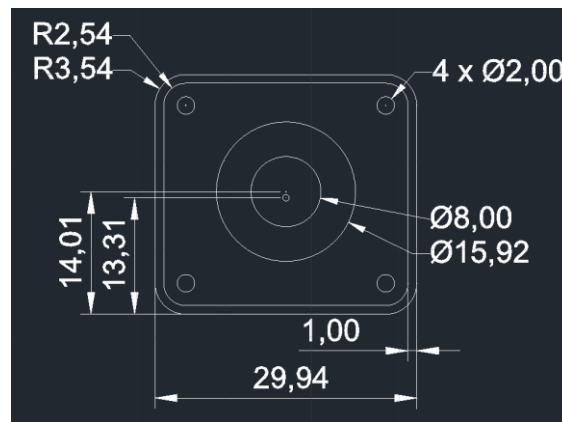


Figure 43 - *AutoCAD* design of the front side of the holder to Adafruit AS7262.

This new holder consists of an update of the holder previously manufactured for Adafruit AS7262, which was manufactured by micromilling using an 8 mm thick plate of PMMA. This new holder has two sides. On one side, back, presents the same design already described on chapter 3.2.5. On the other side, front, there is a holder that fits the base of the cube of the *NanoBank* frame and is tightened with screws. This holder consists of a cylinder with approximately the same thickness as the faces of the cube. The PMMA cylinder is centered in the centre and then deflected 0.7 mm to compensate the shift that the light undergoes.

3.3.5. PMMA microchip

A new microchamber was manufactured using the same manufacturing method and material as presented before in chapter 3.1.2, so that it can be positioned on the base cube with 4 screws in the round openings, as shown in Figure 44 in the AutoCAD design. The inlet and outlet of the chip were positioned outside the area of the manufactured pinhole (which works as an optical path stop).

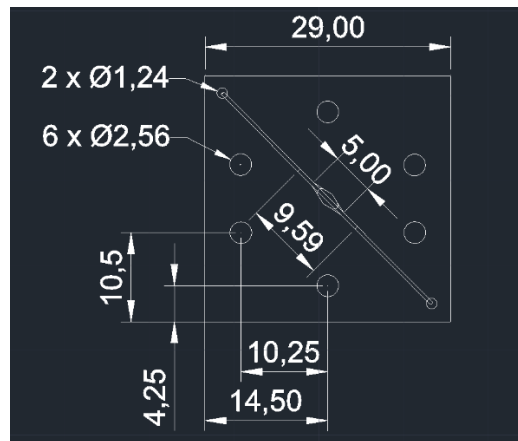


Figure 44 - *AutoCAD* design of PMMA chip of 1 mm microchamber of the sensor.

3.3.6. Sensor and acquisition on PCB

A PCB was designed in *Eagle*, Figure 45, and then manufactured to implement the connections between Arduino Micro and Adafruit AS7262. In this way, both Adafruit sensors are paired as a single device, Figure 46, ready to be functional and connected through the user with a USB cable.

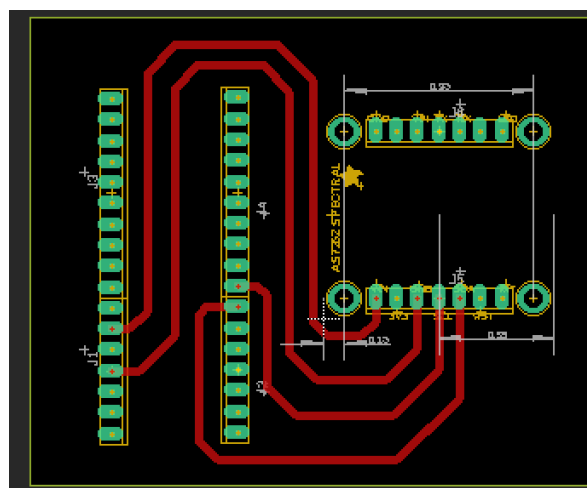


Figure 45 - *Eagle* design of sensor PCB board.

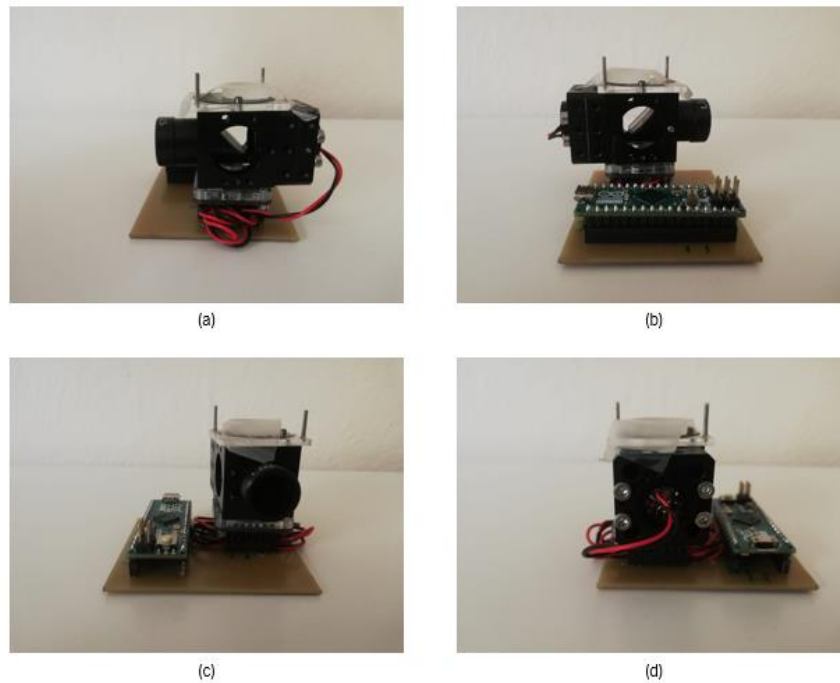


Figure 46 - Sensor viewed from (a) right side, (b) left side, (c) front and (d) back.

3.3.7. Interface algorithm and software

In this chapter the explanation of the code used in the interface is given (full code in Appendix V). The interface was created in the *Processing* software, using Java language. The explanation is given using information that can be imported into the processing website database.

The presented interface consists of a small window to be integrated in the monitoring of an OoC system, to observe the current pH within the 1 mm microchamber, being able to inform users and researchers of the OoC device, when it is necessary to renew the medium for cell culture. It is also possible to observe the transmittance variation over time.

Briefly, “Control P5.*” is a necessary library with Controllers to build a graphical user interface on top of processing sketch, which includes sliders, checkboxes, amongst others, and can be easily added to a processing sketch. The “processing.serial.*” is the serial class for sending and receiving data using the serial communication protocol, good to be adapted to Arduino’s serial communication.

After the communication object has been created and the data is communicated, the global variables are created. “Pfont” is the font class for Processing, which uses fonts with the *.v/w* font format (uses images for each letter). “setup” is the first function created from the interface that

opens the commutation port and set the baudrate (9600) of the communication.

The "settings" function is created to define some of the graphical settings of the operative window to the user. This is a public void function. The ON and DISPLAY, "button" and "button2" buttons are also created, respectively. The ON button switches on the input values for the interface and the start of the pH reading, which is initially 0, as default. The DISPLAY button starts the transmittance response over time and the pH 6 value corresponds to the initial reference, when the transmittance is total.

The "draw" function consists of two parts. The first part is programmed to draw the ON and DISPLAY buttons and their colours are defined with the "fill" function. If the data is being received, the program reads these values "myPort.readStringUnt" and they are saved in the variable "val" and the variable is printed in the console "println(val)". When the mouse passes the DISPLAY button the variable "val" is saved as integer in the variable "ref", to be used in the second part of the "draw" function.

Data that are not stored under the variable "val" are stored under the variable "green", then standardised and stored under the variable "g". This normalization is done by dividing the values by their own value and then multiplied by 100, to obtain the transmittance in percent for easy readability and comparison, and pH value assignment in the code. The variable "r" is created for the pH value and is 0.000 by default and will present a certain value (pH) to the user, according to the transmission value, "g", of the sample in the microchamber. Each interval corresponds to a certain pH value and will only be set after the sensor operation have been checked and finally measured.

When the mouse hovers over the ON button, the data is available again. The graphical representation of the transmission has its color defined with the "stroke" function and is defined with the "line" function, which updates its "prev" value with each data that the software receives. The value of the "prev" variable is a 1 in 1 count and serves as the advance of the x coordinate value of the transmittance graph. The variable "f" creates the font with font Arial and size 16. The texts of the buttons are superimposed on the rectangle of the button with the function "text", positioned in a determinate GUI coordinate (x,y) . The colours of the letters and the pH value box are defined with the function "fill". Finally, and if a reading is executed in which the data occupy the whole window, the transmittance profile (line) starts again at the beginning, in the coordinate $x=0$.

Chapter IV - Results and Discussion

4.1. Macroscopic measurements of pH solutions

4.1.1. Preparation of pH buffer solutions with phenol red

The concentration of phenol red that commercial cell culture medium normally presents is 1.1 mg/L (Basel et al., 1982). To obtain stable pH solutions, without the need for cleanroom environments, several phosphate buffer solutions were prepared (Works, 2018), and mixed with phenol red at the defined concentration of 1.1 mg/L.

Briefly, to prepare 100 mL of a 0.1 M phosphate buffer, is necessary to mix a volume of 0.2 M of sodium phosphate dibasic dodecahydrate ($\text{Na}_2\text{HPO}_4 \cdot 12\text{H}_2\text{O}$, FW = 358.14), solution A, with a volume of 0.2 M sodium phosphate monobasic monohydrate ($\text{NaH}_2\text{PO}_4 \cdot \text{H}_2\text{O}$, FW = 138.01), solution B, and dilute 1:1 v/v with deionised water. The proportion of solution A and B, gives the pH value, as shown in Table 5.

Table 5 - Phosphate buffer for different pH values (Works, 2018)

pH at 25°C	Solution A (mL)	Solution B (mL)
5.8	4.0	46.0
6.0	6.15	43.85
6.2	9.25	40.75
6.4	13.25	36.75
6.6	18.75	31.25
6.8	24.5	25.5
7.0	30.5	19.5
7.2	36	14
7.4	40.5	9.5
7.6	43.5	6.5
7.8	45.75	4.25
8.0	47.35	2.65

To make a reasonable amount of stock solutions, A and B, 500 mL of each stock solutions were prepared. Therefore, for solutions A and B, with a concentration of 0.2 mol/L, 35.816 g and 13.799 g were weighed, respectively.

The quantities for phenol red and sodium phosphate dibasic dihydrate and sodium phosphate monobasic monohydrate were made in the Sartorius professional weighing laboratory scale. The quantity of phenol red was weighed on this same scale for A and B solutions, 5.5 mg of phenol red powder was weighed and mixed until completely dissolved in the solutions, Figure 47.



Figure 47 - Solutions A and B with phenol red in 500 mL volumetric balloon.

Based on the fact that buffer solutions can change their pH as they are exposed to external conditions, such as humidity and temperature changes for a long time, and stock solutions A and B are more stable, it was decided to add the phenol red directly to these solutions and store them until needed. Stock solutions can be stored for a maximum of one month at a low temperature of 4 °C. Figure 48 presents the final 12 buffer solutions, with pH ranging from 5.8 – 8.0, and their colour change due to the presence of the pH indicator, phenol red.

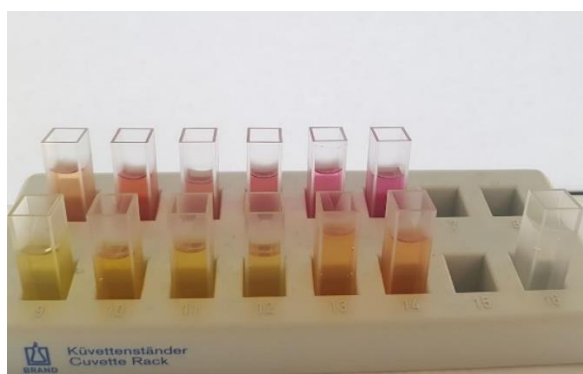


Figure 48 - Buffer solutions and water (reference solution) in 1 cm cuvettes.

4.1.2. Transmittance response acquisition on 1 cm cuvettes – pre-study

The setup for the acquisition of the response over the wavelength range, Figure 49, is easy to assemble and fast in obtaining the response. The light comes from *DH Ocean Optics UV-VIS-NIR*

Fiber Optic Light Source, with a high-power light source MINI Deuterium Tungsten Halogen Source with a 200 - 2000 nm shutter (Ave, n.d.), whose properties are shown in Table 6.

This light is propagated to the dark chamber, through fiber optics, where the cuvettes of different buffer solutions are placed. This camera allows that there is no interference from other light sources, which act as noise in the obtained signal. The light then crosses the buffer solution inside the cuvette, an optical path of 1 cm, and is transmitted again to fiber optics. The light propagates within the optical fiber to the receiver, the spectrometer, which translates into a transmittance signal read and presented to the user at the *OceanView* interface. The operation of the *OceanView* software is shown in the Appendix III.

A spectrometer allows the decomposition of light into different wavelengths. The transmission of light or radiation, in general, is measured on a fluid (liquid or gaseous pores) at different wavelengths. This produces the transmission spectrum that is characteristic of each substance.

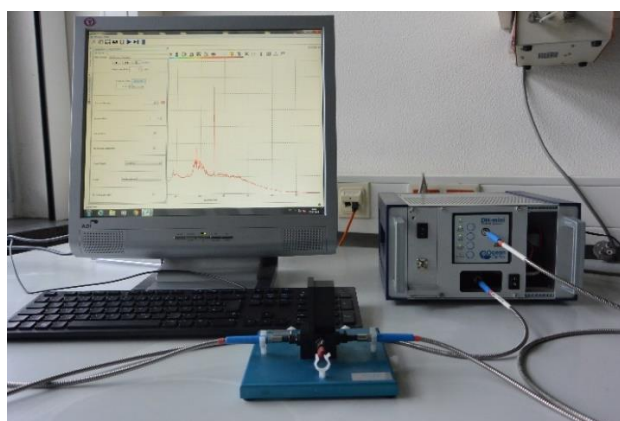


Figure 49 - Acquisition setup for the buffer transmittance response. PC, on the left, camera for placing the buffer, in the middle, and light source and spectrometer, on the right, connected to the camera by optical fiber.

Table 6 - Optical features of DH-MINI Ocean Optics UV-VIS-NIR Fiber Optic Light Source (Ave, n.d.).

Spectral output	200 - 2500 nm
Stability	<0.2% (standard deviation for k=1)
Drift	<0.1%/h
Warm-up time	6 minutes, dependent on ambient conditions
Bulb lifetime (average/guaranteed)	2000 – 1000 h
Output connector	SMA 905
Power consumption	12 W

Each substance has a so-called characteristic wavelength, during which radiation is absorbed. By measuring the transmittance (the ratio of the optical radiation power before and after the light pass through the sample), the substance itself can be determined, or in this case, the pH of the sample in study. The obtained results are presented in Table 7.

4.2. Microfluidic chamber measurements

In order to have an expected transmittance response value in a 1 mm microchamber, through transmittance values already obtained for a 1 cm cuvette, a theoretical study was made based on the radiation behavior in microchannels, Figure 50. At the boundary surfaces of the optical waveguides and the microchannels radiation, losses occur due to the millimetre size apparatus.

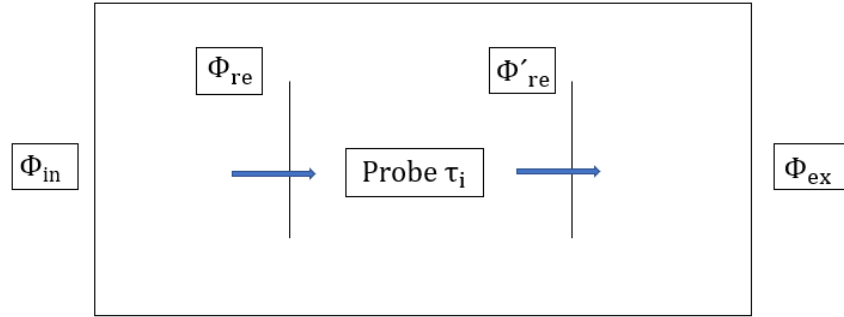


Figure 50 - Radiation flux in microchannel.

Φ_{in} : incident radiant flux (W)

Φ_{ex} : continuous radiant flux (W)

Φ_{re} : loss of reflection upon entry (W)

τ_i : pure transmission (number)

Φ'_{re} : loss of reflection on exit (W)

d: layer thickness of the fluid (mm)

As mentioned, the (gross) transmission factor is measured by $\tau = I/I_0$. However, reflection, $\rho = \Phi_{re}/\Phi_{in}$, and scattering represents losses in the measuring apparatus. Together with the radiation losses (factors), the radiation flux Φ_{ex} at the output, Equation 12:

$$\Phi_{ex} = \Phi_{in} \cdot (1 - \rho) \cdot \tau_i \cdot (1 - \rho) \quad (12)$$

The transmittance describes the ratio of the outgoing to the incoming radiation flow in the medium itself. The "pure" transmission therefore only refers to the weakening by the medium (fluid) itself.

The other attenuation factors are determined by the apparatus. The total factor of attenuation in this present setup is P with $(1 - \rho)^2 = P$. This weakening factor P is determined by an empty

measurement without sample. For this purpose, the deionised solvent, i.e. pure water with $\tau_i = 1$, is pumped through the microchannel. The pure transmission is:

$$\tau_i = \tau/P \quad (13)$$

It follows the equation that calculates the radiation flux in vacuum:

$$\Phi_v = \Phi_{in} \cdot (1 - \rho) \cdot \tau_i \cdot (1 - \rho) \quad (14)$$

From Φ_{ex} and Φ_v :

$$\tau_i = \frac{\Phi_{ex}}{\Phi_v} \quad (15)$$

The pure transmission is directly obtained from the optical power measurement with a sample solution concerning the empty measurement without any sample. The test solution, i.e. with pure water, measured according to the equation τ_i .

The transmission drops exponentially with greater layer thickness d and higher concentration k , it filters out the general weakness law (Equation 16). The absorption coefficient α describes the weakening of light.

$$\Phi_{ex} = \Phi_v \cdot e^{-\alpha \cdot d} \quad (16)$$

α : absorption coefficient in nm

k : concentration in g (sample)/g(solution)

d : layer thickness of the fluid in mm

There is a constant for fluids, the so-called extinction coefficient ε . This is the characteristic substance size.

$$\tau_i = 1 \cdot e^{-\varepsilon \cdot k \cdot d} \quad (17)$$

From this equation and with the results of the complete transmission spectrum for buffer solutions we can predict the transmittance result for the designed microchambers:

$$const = \varepsilon \cdot k = -\frac{\ln \tau_i}{d} \quad (18)$$

For instance, for an 8.0 pH sample the transmittance in a 1 cm cuvette is 24.7 %. It follows:

$$\varepsilon \cdot k = -\frac{\ln 0.241}{1} \approx 1.423$$

Therefore, the transmission level $\tau_{8.0}$ for buffer solution pH 8.0 in a 1 mm chamber can be predicted:

$$\tau_{8.0} = 1 \cdot e^{-1.399 \cdot 0.1} = 0.867$$

In the same way, the transmission level was predicted for all the other buffer solutions. Table 7 lists the transmittance values obtained for the buffer solutions (pH ranging from 5.8- 8.0) measured in a 1 cm cuvette, as well as the theoretical transmittance obtained from equations 17 and 18, for microchambers with 1 and 2 mm.

Table 7 - Measured transmittance for buffer solutions with different pH in a 1 cm cuvette and forecast for 1 mm and 2 mm microchamber.

pH	$\tau_{1cm}(\%)$	τ_{1mm}	τ_{2mm}
5.8	97.72	0.998	0.995
6.0	96.29	0.996	0.992
6.2	93.99	0.994	0.988
6.4	91.54	0.991	0.982
6.6	87.42	0.987	0.973
6.8	80.50	0.979	0.958
7.0	72.62	0.969	0.938
7.2	61.05	0.952	0.906
7.4	49.57	0.932	0.869
7.6	39.76	0.912	0.832
7.8	30.66	0.889	0.789
8.0	24.07	0.867	0.752

4.3. Photodetection spectral behaviour

The typical optical characteristics can be presented with the spectral responsivity of the 6 photodetector channels. Fiber optic light was used, the same used for the measurements in the cuvette with 1 cm for the buffer transmittance response, connected to a monochromator and the light beam guided by an optical fiber to Adafuit AS7262 (this setup is seen partially in the previous Figure 33(d)). In the monochromator an advance in the wavelength of the beam of light from 5 in 5 nm from 280 to 725 nm was performed, making a reading for the intensity response on the 6 channels.

From Figure 51 it is possible to observe the range that each channel presents and the intensity that each one reaches, for the light coming from the light source.

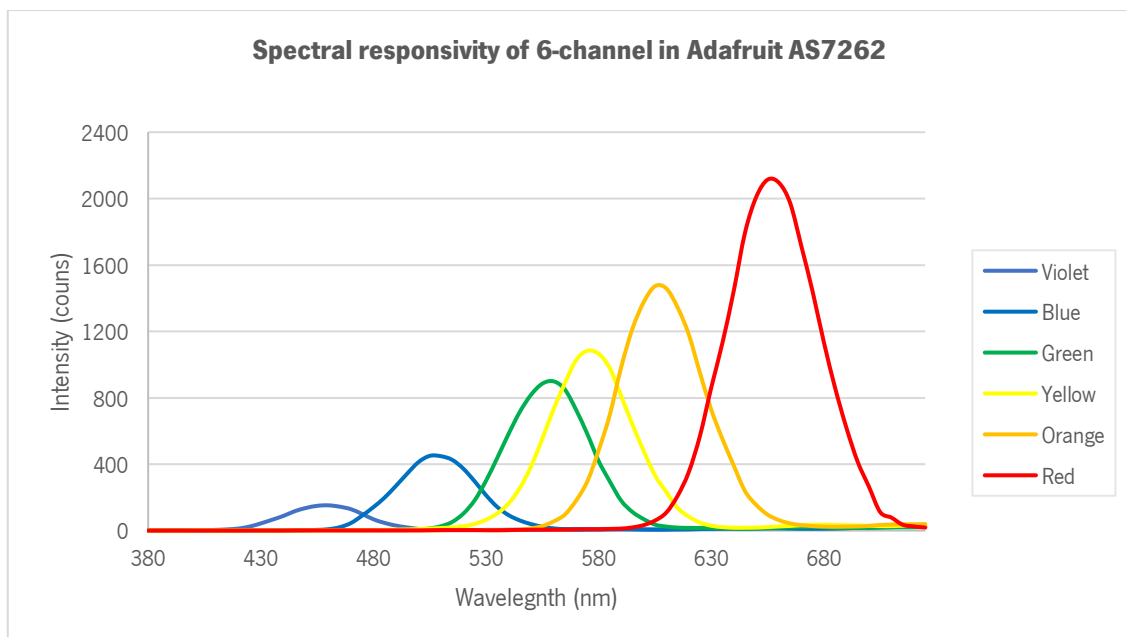


Figure 51 - Graphical representation of the intensity on the 6 channels of Adafuit AS7262 using a white optic fiber light source.

4.4. pH measurements using 1 cm cuvette

In order to verify the pH values from each buffer solution, the measurements have been carried out with a pH meter and a magnetic stirrer with a speed of 570 rpm, cf. Figure 52. The pH errors associated with the deviation from the expected value are less or equal to 1% (values presented in Table 8), which can be considered negligible.

Table 8 - Measures of pH with prepared buffer solutions with error associated and temperature conditions.

$\text{pH}_{\text{theoretical}}$	$\text{pH}_{\text{experimental}}$	Error (%)	$T_{\text{buffer}}(^{\circ}\text{C})$	$T_{\text{room}}(^{\circ}\text{C})$
5.8	5.76 ± 0.01	0.69	21.2	21.5
6.0	5.96 ± 0.01	0.67	21.1	21.4
6.2	6.17 ± 0.01	0.48	21.2	21.4
6.4	6.39 ± 0.01	0.16	21.5	21.3
6.6	6.6 ± 0.01	0	21.5	21.2
6.8	6.82 ± 0.01	0.29	21.4	21.2
7.0	7.0 ± 0.01	0	21.5	21.1
7.2	7.25 ± 0.01	0.69	21.4	21.1
7.4	7.47 ± 0.01	0.95	21.3	21.1
7.6	7.65 ± 0.01	0.66	21.3	21.1
7.8	7.86 ± 0.01	0.79	21.6	21.1
8.0	8.08 ± 0.01	1	21.6	20.9

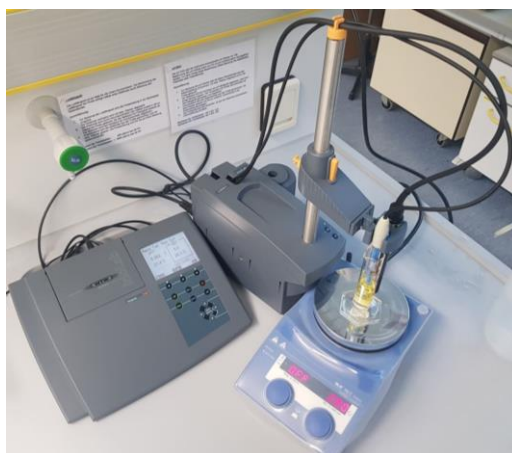


Figure 52 - Setup to measure pH values. A pH meter from inoLab in measuring the pH and temperature conditions of buffer solution in a test tube with a stirrer, placed in an IKA RCT basic magnetic stirrer.

The twelve buffer solutions ranging pH from 5.8 – 8.0, and used in this study, were placed in 1 cm cuvettes to make a pre-study of the transmittance behaviour they present across the optical spectrum, cf. Figure 61. Through this study it is possible to predict the transmittance response of these same solutions to the 1 mm chamber, through analytical calculations.

At high pH, the solution has a visible fuchsia colour that changes to red, then yellow, as the pH decreases. This color change is observed in the variation of the wavelength peaks at 560 and 430 nm. As seen in Figure 53 and discriminated at Table 9, the transmittance peak at 560 nm is very pronounced at pH 8.9, but almost disappears when the pH decreased to 6.0. A smaller peak is observed at 430 nm with acidic pH levels that increase with an increase in the pH (as it becomes more alkaline).

Closer examination of the two transmittance peaks in the solutions, with and without phenol red, reveals an influence from the buffer to the transmittance at 430 nm, whereas the peak at 560 nm seems to not be so much affected. These peaks correspond to peaks of the phenol red absorbance in the buffer solution (Moldes et al., 2004). This suggests that using the 560 nm peak would be more advantageous for the direct calculation of pH.

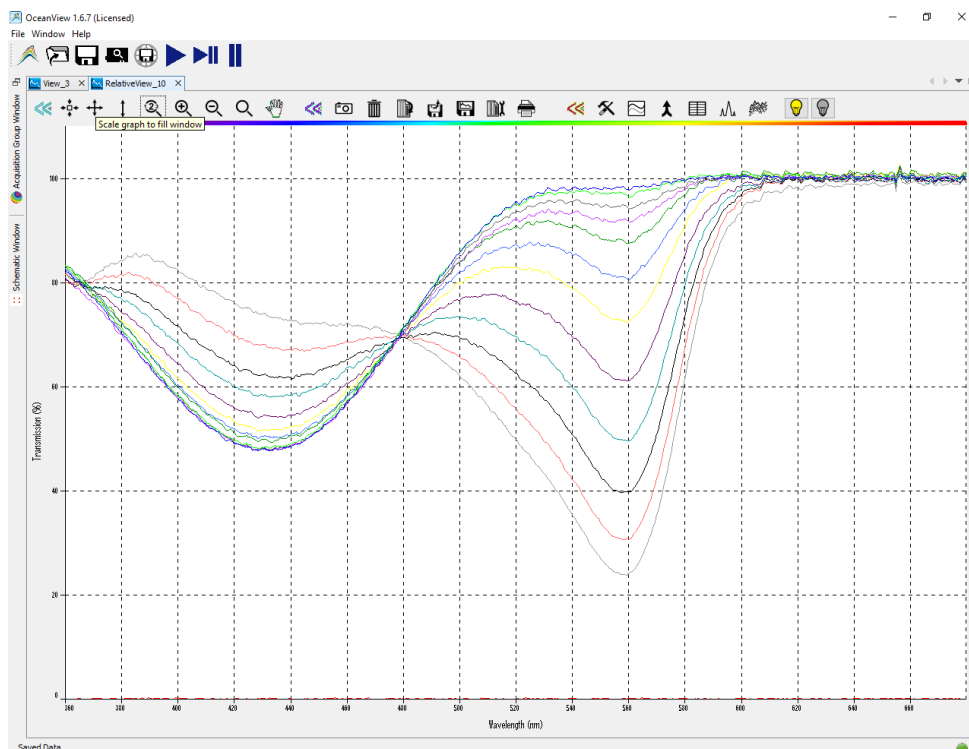


Figure 53 - Transmittance Spectra of complete buffer solutions at different pH levels, obtained with the software *OceanView*.

Table 9 - Transmittance in two peaks of transmittance spectra for the buffer solutions.

pH	<i>T</i>_{430 nm}	<i>T</i>_{560 nm}
5.8	75.93	24.07
6.0	69.74	30.76
6.2	63.91	39.76
6.4	59.74	49.57
6.6	55.61	61.05
6.8	53.25	72.62
7.0	51.81	80.5
7.2	50.94	87.42
7.4	49.71	91.54
7.6	49.31	93.99
7.8	49.16	96.29
8.0	48.97	97.72

4.5. pH measurements using 1 mm chamber

This test was made in a setup in which the microchannel is equipped with two lateral glass fiber connections (light-waveguide=LWL). The chip, designed in AutoCAD, cf. Figure 54, was fabricated in PMMA via micromilling, with a depth of 0.5 mm, whose microchamber consists of a part of the microchannel 1 mm long (detection channel), as similarly described in sub-chapter 3.1. The glass fiber was inserted into the microchip and fixed with optical glue with a small needle, as shown in Figure 55(a).

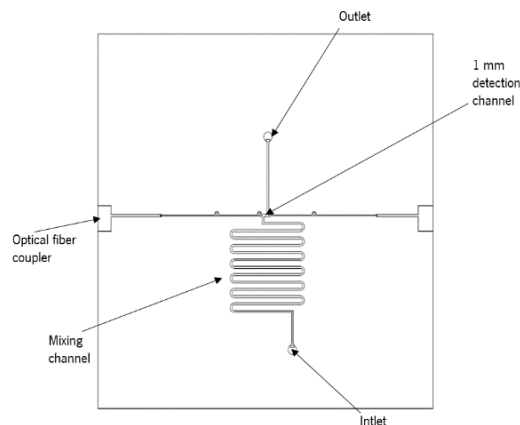


Figure 54 - AutoCAD design of the 1 mm chamber to study the transmittance level for different buffer solutions.

The beam enters via the one optical waveguide, passes through the chip and the sample in the 1 mm microchamber and leaves via the two optical waveguides in a weakened state. The fibers were adhered to the microchip and were fixed with optical glue, Figure 55(c). The same process was used to glue the inlet and outlet tubes to PMMA.

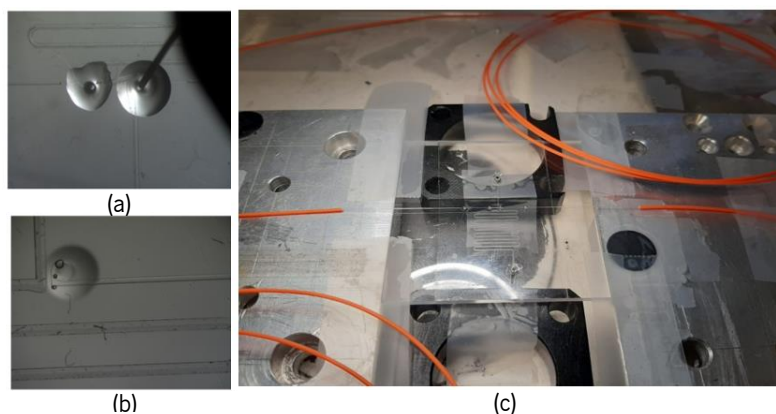


Figure 55 - (a) Method of inserting the glue with a small needle to fix the optical fibers on the chip; (b) fixed optical fiber so that the waveguides are directed to the microchamber; (c) the 1 mm microchamber PMMA microchip with the optical fibers.

The results that are presented in this chapter, are achieved through the setup shown in Figure 56, where at every 10 minutes the flow of pure water and the different buffer solutions is alternated.

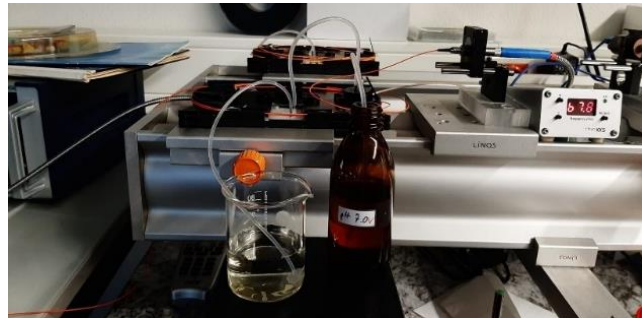


Figure 56 - Setup for the transmittance measurements on the microchamber. The buffer solutions go to the microchip in continuous flow during the whole measurement through a micropump with a frequency near to 100 Hz. The waste liquid is discarded into a beaker.

The different steps presented, as shown in Figure 57, are the intensity response, in counts, for the buffer solutions with pH 5.8, 6.4, 7.0, 7.4 and 8.0 (calibration points in this study). The maximum value read from each of the channels represents the reference intensity value, pure water. The photodetector channels with the highest variation, and with attention to the percentage variation between the reference level and the different levels for each buffer solution, are the green channel and the violet channel (Figure 57). It can be assumed that the read values are stable, and the abrupt variations observed can be due to the presence of bubbles.

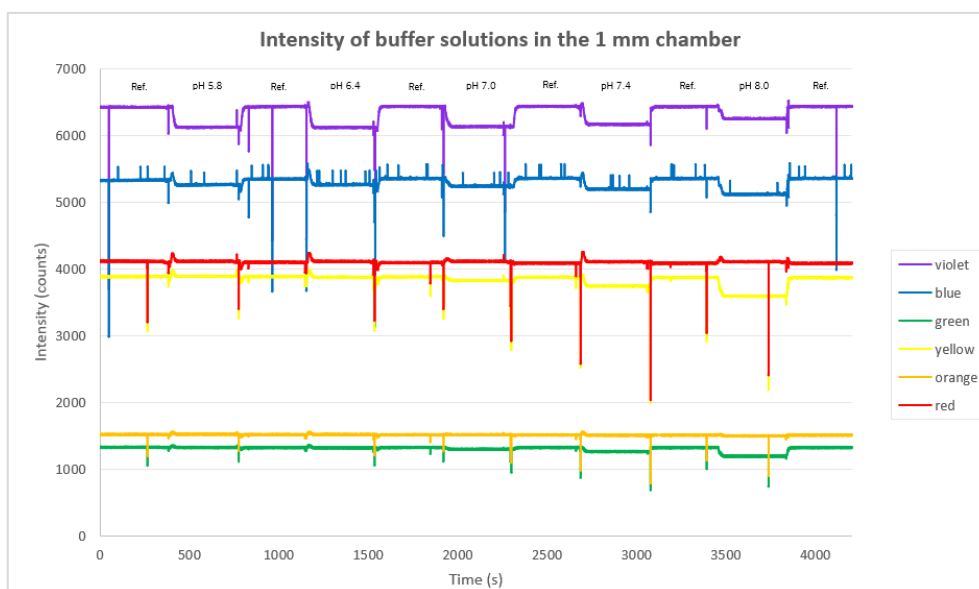


Figure 57 - Intensity of Adafruit AS7262 6-channels for experiment performed for buffer solutions with pH 5.8, 6.4, 7.0, 7.4, 8.0, respectively over time. The experiment is done by alternating the reference sample,

pure water, and buffer solutions, in the 1 mm chamber. Each step corresponds to the response of the buffer solution in relation to the water response (maximum observable value).

The transmittance values are achieved by normalizing the intensity values. The values are divided by the reference value, in this case, the value of pure water. Analysing the transmittance value over the time of the experiment, Figure 58, the violet channel response, increases with the increase in pH. On the other hand, the transmittance read through the green channel, decreases with increasing pH. If we compare these with the transmittance results in % read, by the spectrometer for a 1 cm cuvette, the values agree.

A variation of the transmittance response along the different pH values for these two photodetector channels, cf. Figure 59, shows that between 5.8, 6.0, 6.2 and 6.4 pH, the transmittance variation is too small to have a good accuracy in a sensor.

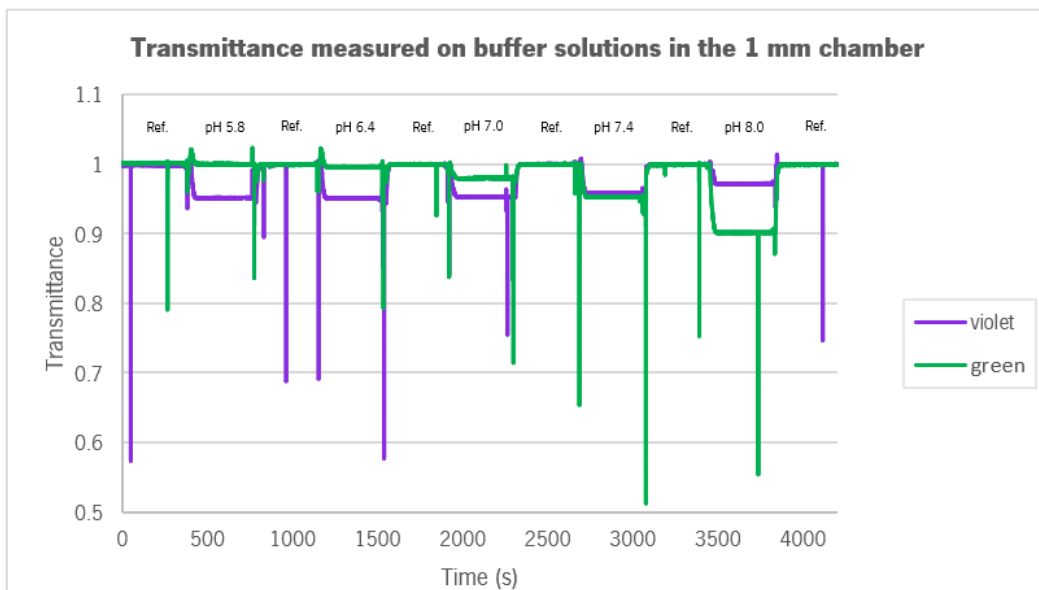


Figure 58 - Transmittance of channels violet and green of Adafruit AS7262 for experiment performed for buffer solutions pH 5.8, 6.4, 7.0, 7.4, 8.0, respectively over time. The experiment is done by alternating the reference sample, pure water and buffer solutions, in the 1 mm chamber. Each step corresponds to the response of the buffer solution in relation to the pure water response (maximum observable value).

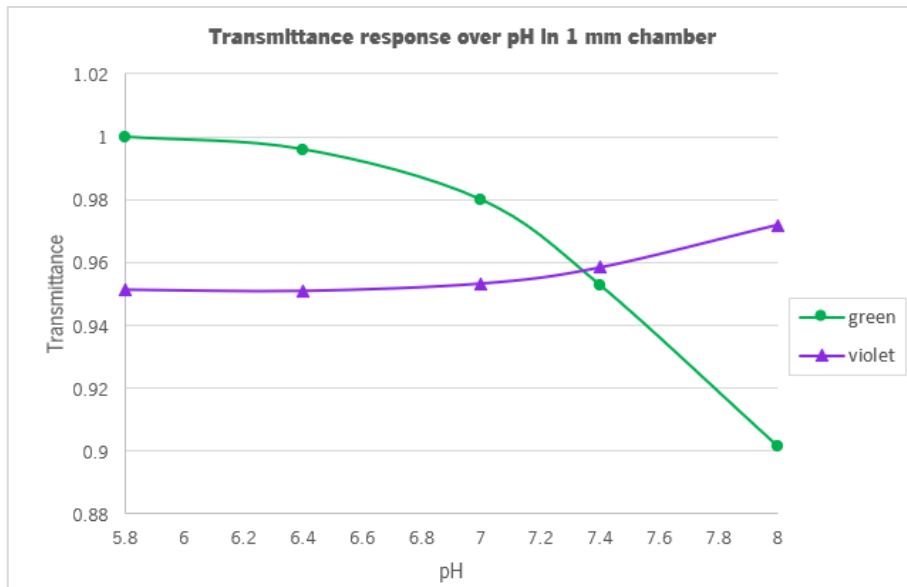


Figure 59 - Transmittance response of channels violet and green of Adafruit AS7262 for pH 5.8 - 8.0 range. The experiment is performed for buffer solutions pH 5.8, 6.4, 7.0, 7.4, 8.0, in the 1 mm chamber, which is done by alternating the reference sample, pure water and buffer solutions.

The error between the theoretical and practical values is less than 3.97%, analysing in detail the Figure 60. These deviations can be explained due to the following factors: (1) The theoretical value comes from considering the transmittance value only in one wave compress, 560nm, in a 1 cm cuvette; and (2) The actual value of the green channel of the photodetector makes an integration in a range of wavelengths and presents only a digital value. Nevertheless, it can be observed from the trend lines, that the behaviour between the theoretical and experimental lines, which characterises the transmittance along the pH, are similar.

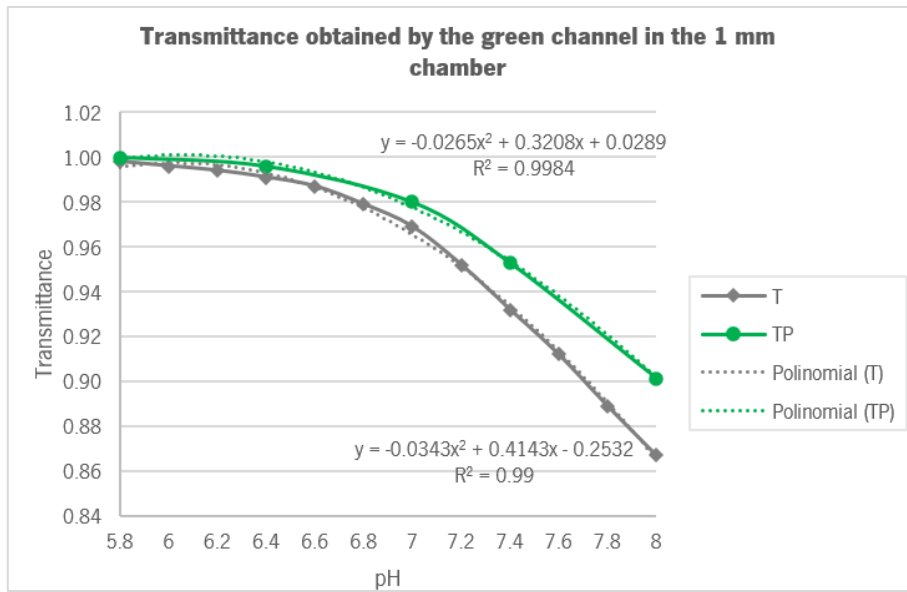


Figure 60 - Expected theoretical response (T) and experimental transmittance response (TP) of green channel of Adafruit AS7262 for pH 5.8 - 8.0 range. A polynomial approach is made to study the error between what is obtained and what is expected, through polynomial equations. The experiment was performed for buffer solutions pH 5.8, 6.4, 7.0, 7.4, 8.0, in the 1 mm chamber, which is done by alternating the reference sample, pure water and buffer solutions.

Overall, it can be concluded that the accuracy for the 1 mm chamber is not enough to distinguish the pH values in a pH 0.2 range. Therefore, it is necessary to increase the optical path in the 1 mm chamber.

4.6. pH measurements using 2 mm chamber

To prove that by doubling the optical path it is possible to have enough accuracy before proceeding with the development of the sensor, the same test as performed in the chapter 4.5, was performed for a 2 mm chamber, cf. Figure 61.

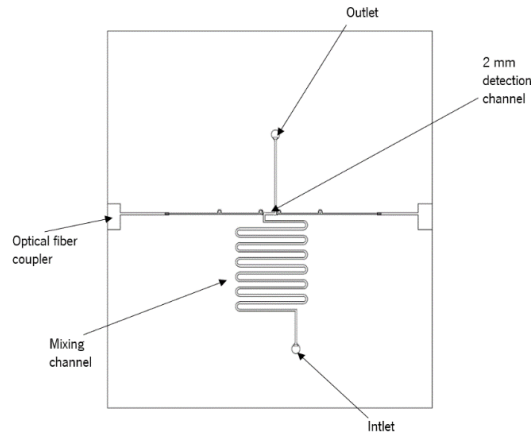


Figure 61 - AutoCAD design of the 2 mm chamber to study the transmittance level for different buffer solutions.

The photodetector channels with the highest sensitivity are the violet, blue, green and yellow channels, Figure 62, taking the same considerations into account when choosing photodetector channels for the 1 mm camera. Contrary to the response of the 1 mm camera, this can have a higher number of channels with a reasonable response.

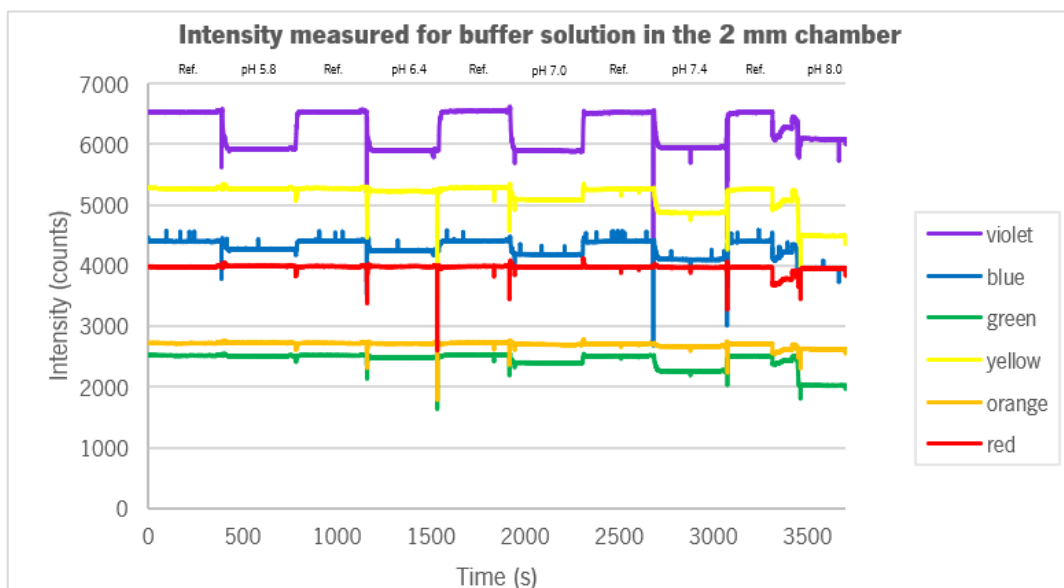


Figure 62 - Intensity of Adafruit AS7262 6-channels for the experiment performed with buffer solutions of pH 5.8, 6.4, 7.0, 7.4, 8.0, respectively, and over time. The experiment is done by alternating the reference

sample, pure water and buffer solutions, in the 2 mm chamber. Each step corresponds to the response of the buffer solution in relation to the pure water response (maximum observable value).

The intensity is then normalised and translated into the transmittance that these four channels present for the five buffer solutions, Figure 63.

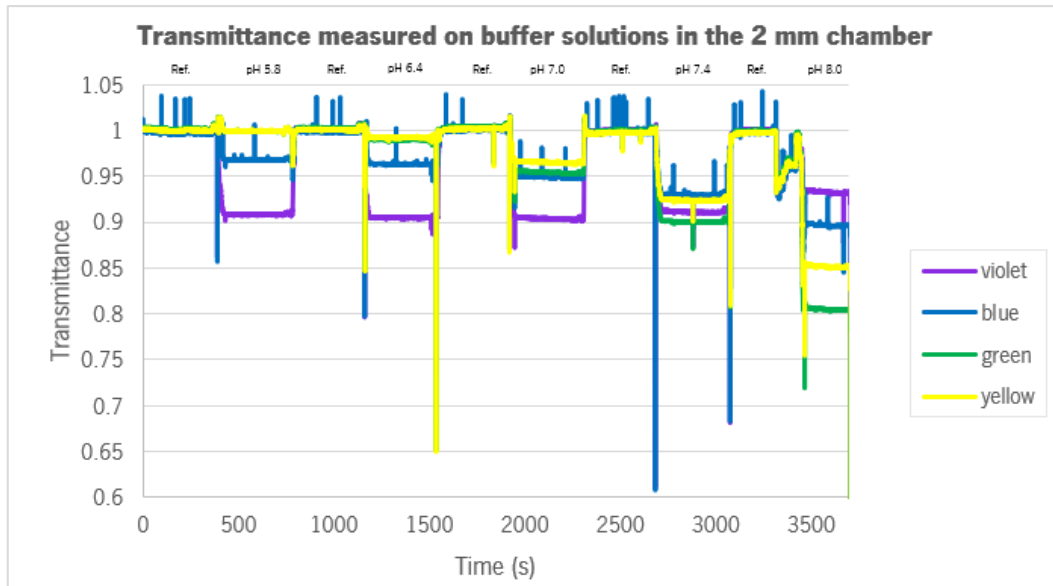


Figure 63 - Transmittance of channels violet, blue, green and yellow of Adafruit AS7262 for experiment performed with buffer solutions pH 5.8, 6.4, 7.0, 7.4, 8.0, respectively, over time. The experiment is done by alternating the reference sample, pure water and buffer solutions, in the 2 mm chamber. Each step corresponds to the response of the buffer solution in relation to the pure water response (maximum observable value).

From the transmittance response over the time of the experiment, it is presented the transmittance response corresponding to the different pH values, for the four chosen channels, Figure 64.

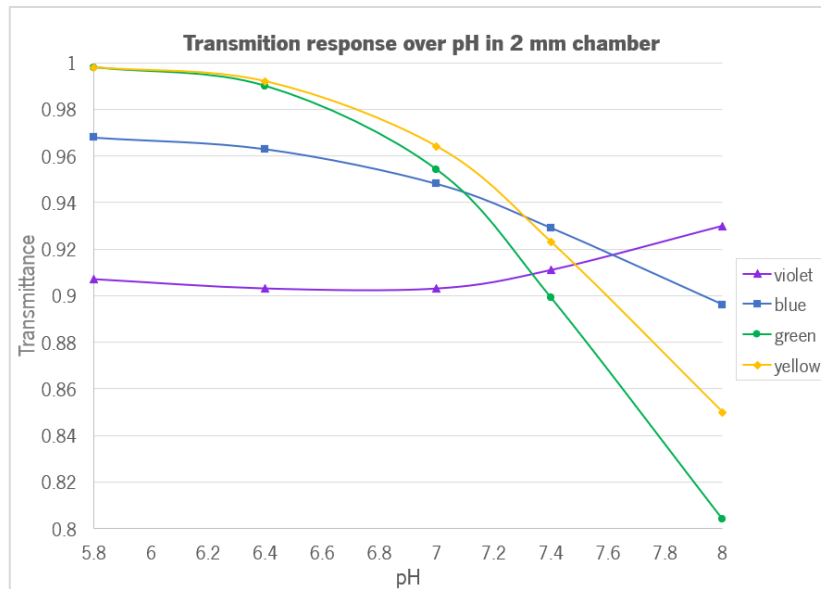


Figure 64 - Transmittance response of channels violet, blue, green and yellow of Adafruit AS7262 for pH 5.8 - 8.0 range. The experiment is performed for buffer solutions pH 5.8, 6.4, 7.0, 7.4, 8.0, in the 2 mm chamber, which is done by alternating the reference sample, pure water and buffer solutions.

The transmittance range is increased by increasing the optical path. The green channel demonstrates once again to be the best channel for the sensor integration. It can be stated that an optical path of 2 mm allows the sensor to obtain sufficient precision to distinguish the different transmittance values, which correspond to the different pH values, ranging 0.2 pH between the different samples.

The error between the predicted value for the 2 mm chamber and the experimental value obtained, is less than 6.91% (this error is obtained for the 8.0 pH buffer solution, analysing the Figure 65). Again, different factors lead to this deviation.

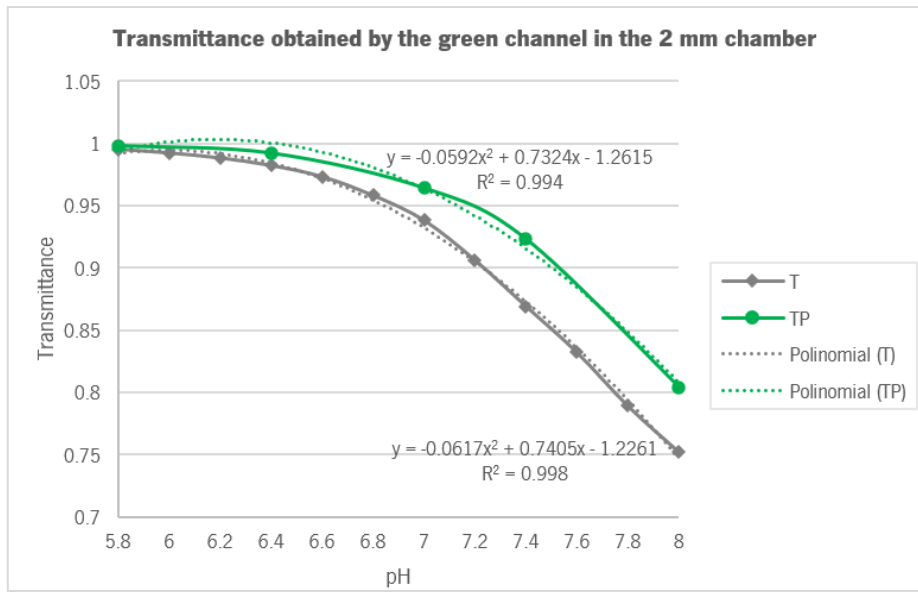


Figure 65 - Expected theoretical response (T) and experimental transmittance response (TP) of green channel of Adafruit AS7262 for pH 5.8 - 8.0 range. A polynomial approach is made to study the error between what is obtained and what is expected, through polynomial equations. The experiment is performed for buffer solutions pH 5.8, 6.4, 7.0, 7.4, 8.0, in the 2 mm chamber, which is done by alternating the reference sample, pure water and buffer solutions.

4.7. pH measurements using beam-splitter sensor

4.7.1. Stability and signal noise

To analyse the stability of the sensor, the reference level of the 6 photodetector channels was measured. It consists of a measurement of the standard intensity response and transmittance level that the channels read for pure water, pumped into the microchip with the *neMESYS* syringe pump at 20 $\mu\text{L}/\text{min}$.

The common range for the green, yellow, orange and red channels was 0.002 during the measurement, as it can be seen in the noise signal behaviour, Figure 66. This response demonstrates good sensor stability and accuracy. The violet and blue channels take longer to stabilize, but after reaching the final reference intensity level, are stable as the other four channels.

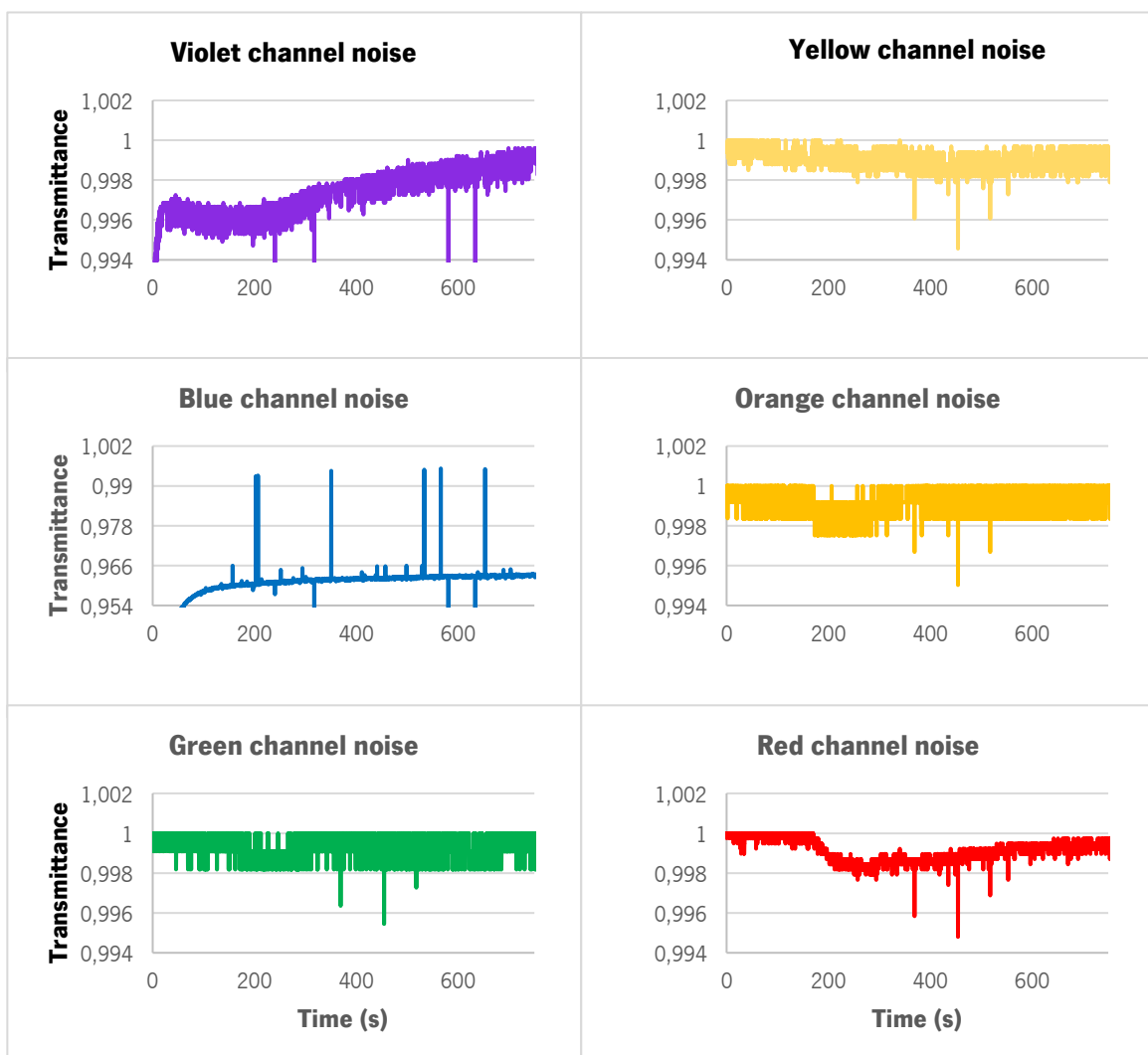


Figure 66 - Noise signal of the channels of photodetector of Adafruit AS7262.

4.7.2. Proof of operation

Three solutions, as shown in Figure 67, were prepared from red food coloring ink to check if the sensor has a response that corresponds to that measured in a 1 cm cuvette on the spectrometer using the optical cover setup already described in sub-chapter 4.1.2. These three solutions were used instead of the solutions with different pH as they have quite different transmittance spectra, Figure 68, and can therefore be used with references for calibration and testing of the sensor.

The first solution, solution 1, was prepared with red food coloring ink and pure water in a 4:1 ratio (v/v). The second solution, solution 2, was a dilution from the first solution with pure water in a 4:1 ratio (v/v). The third solution, solution 3, was a dilution from the second solution with pure water in the proportion of 4:1 (v/v).



Figure 67 - Solutions 1, 2 and 3 prepared with red food coloring ink and pure water, 4:1, 8:1, 12:1, respectively.

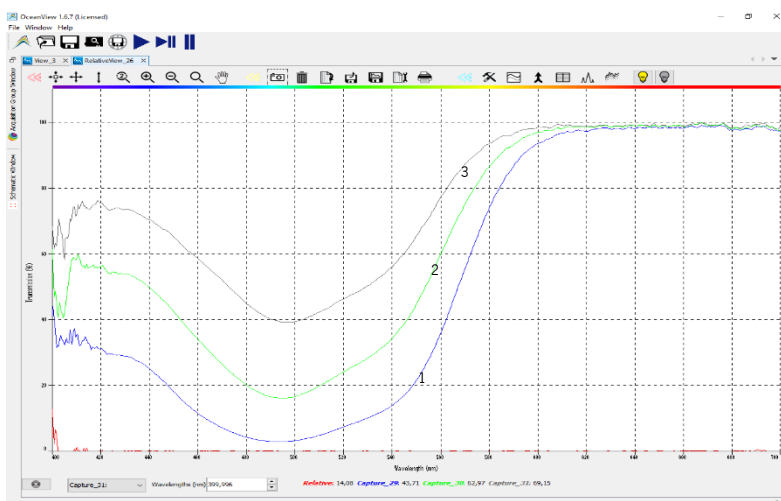


Figure 68 - Transmittance Spectra of red food colouring ink solutions 1, 2 and 3, obtained with the software *OceanView*.

The behaviour of the values of the work for the third step in Figure 69, corresponding to solution 3, and corresponding to those obtained in the 1 cm cuvette, using the mathematical analysis made in the chapter 4.2. of the 1 and 2 mm chamber forecast result. For solution 2, the step does not correspond to reality, because the different channels of the photodetector in the Adafruit AS7262 do not obtain the same level of transmittance, as this would mean that the transmittance value would be the same for 6 different wavelengths, which is not true. This error can be due to bad measurements, with bubbles in the fluid, causing noise that overlaps with the signal to be measured.

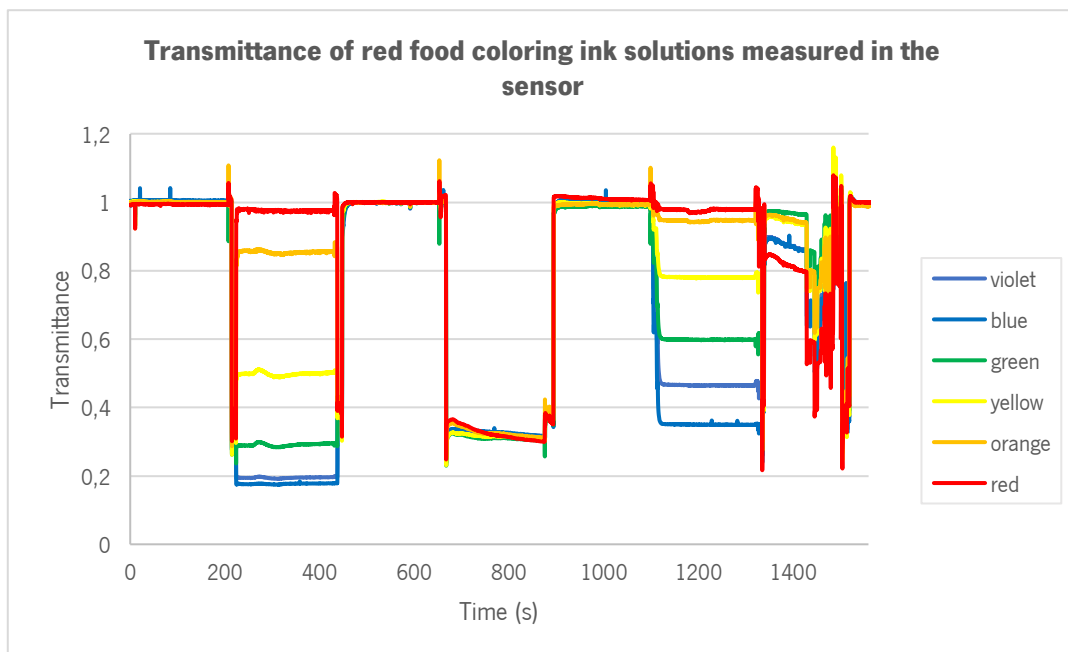


Figure 69 - Transmittance obtained with the sensor for experiment performed with red food coloured ink solution, first, second and third solution, respectively over time. The experiment is done by alternating the reference sample, pure water, and red food coloured ink solution, pumping the fluids using *neMESYS* syringe pump at a flowrate of 20 $\mu\text{L}/\text{min}$. Each step corresponds to the response of the solutions in relation to the pure water response (maximum observable value).

In the first step, corresponding to solution 1, it was verified that the minimum transmittance that the sensor acquires is 0.17 (17%), because according to the results obtained by the spectrometer, the transmittance of the most concentrated solution should be lower for the microchamber. To verify that the lowest measured transmittance value is 17%, a test was made with a black sample, Figure 70. A solution was then made with black food coloring ink and pure water in the proportion of 1:10.

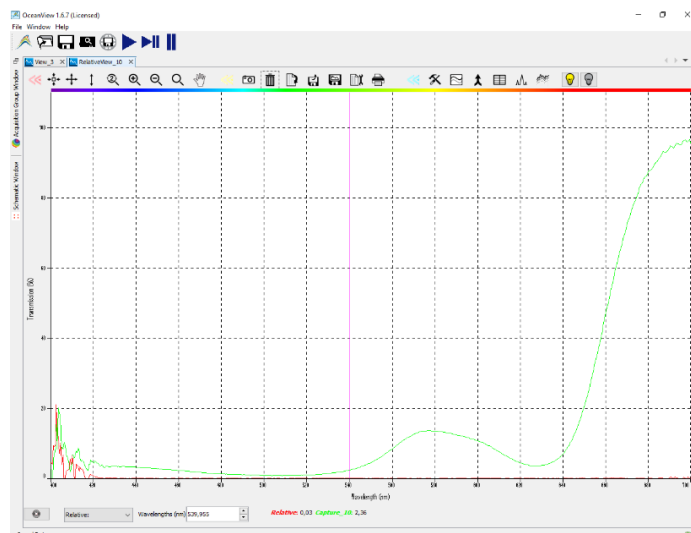


Figure 70 - Transmittance Spectra of black food colouring ink solution, obtained with the software *OceanView*.

After three alternate measurements of pure water and the solution prepared with pure water and black cake ink, it is possible to conclude that the sensor is workable in the acquisition of transmittance between 17% and 100%, Figure 71. For the different pH samples this is not a factor that leads to defer or neglect the results, since the highest fixed transmittance is at 0.8 (80%).

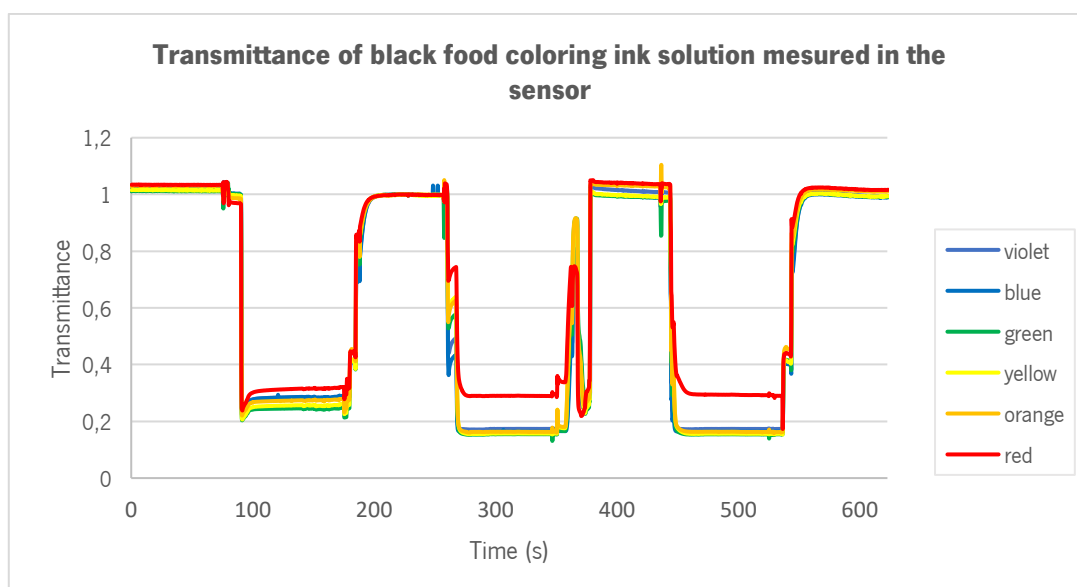


Figure 71 - Transmittance obtained with the sensor for experiment performed with black food coloured ink solution (black food colouring ink and pure water in the proportion of 1:10), over time. The experiment was done by alternating the reference sample, pure water, and black food coloured ink solution, pumping the fluids using *neMESYS* syringe pump at a flowrate of 20 $\mu\text{L}/\text{min}$.. Each step corresponds to the response of the same solution in relation to the pure water response (maximum observable value).

The result of the values obtained for the transmittance with the black solution is then compared with the measurement of the transmittance response of the reference, the pure water, without the mirror in the setup, Figure 72.

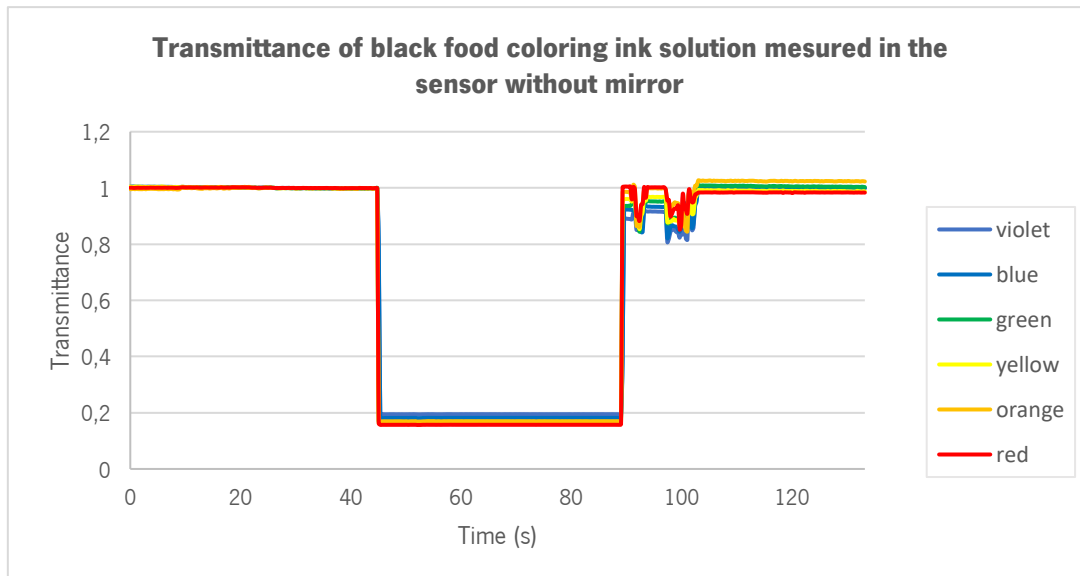


Figure 72 - Transmittance obtained with the sensor without mirror for experiment performed with black food coloured ink solution (black food colouring ink and pure water in the proportion of 1:10), over time. The experiment was done by alternating the reference sample, pure water, and black food coloured ink solution, pumping the fluids using *neMESYS* syringe pump at a flowrate of 20 $\mu\text{L}/\text{min}$. The step corresponds to the response of the same solution in relation to the pure water response (maximum observable value).

From this, it is possible to reach an important conclusion on the small limiting factor of the sensor in this application. Compared to the minimum transmittance that can be measured by the photodetector channels, a study made with the black inked sample, the minimum transmittance signal obtained is due to the light that is reflected by the background of the microchamber, due to the PMMA material.

4.7.3. Final measurements

The final sensor measurements for the 12 different buffer solutions with pH 5.8, 6.0, 6.2, 6.4, 6.6, 6.7, 6.8, 7.0, 7.2, 7.4, 7.6, 7.8 and 8.0 are presented herein.

Figure 73 represents the transmittance value measured by the green channel of the Adafruit AS7263 photodetector over the time of the experiment. Each step corresponds to a different solution and again the maximum (reference) value is pure water.

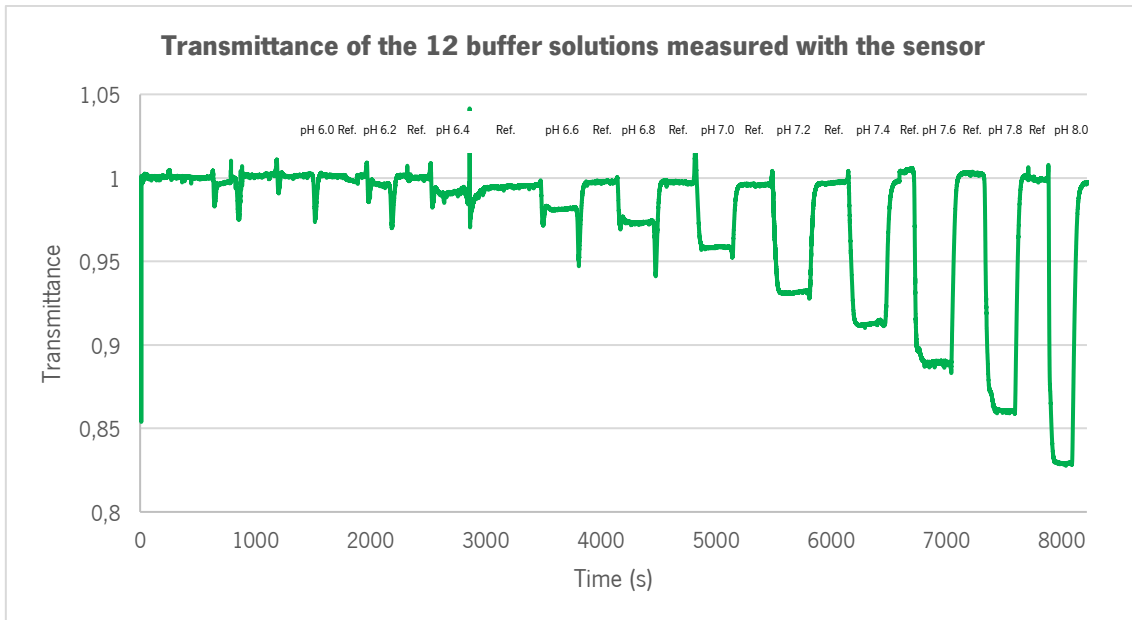


Figure 73 - Transmittance obtained with the sensor for experiment performed with buffer solutions pH 5.8, 6.0, 6.2, 6.4, 6.6, 6.8, 7.0, 7.2, 7.4, 7.6, 7.8 and 8.0, respectively, over time. The experiment was done by alternating the reference sample, pure water and buffer solutions, in the 1 mm chamber, pumping the fluids using *neMESYS* syringe pump at a flowrate of 20 $\mu\text{L}/\text{min}$. Each step corresponds to the response of the buffer solution in relation to the pure water response (maximum observable value).

It is possible to take a reading from the buffer solution with pH 6.0, if we attribute it to the transmittance result 100%. The buffer solution of 6.2 presents transmittance of 99%, pH 6.4, 98.5%, pH 6.6, 98%, pH 6.8, 97%, pH 7.0, 95.5%, pH 7.2, 93%, pH 7.4, 91%, pH 7.6, 89%, pH 7.8, 86% and pH 8.0, 83%, respectively. The range that the sensor can measure is pH between 6.0 - 8.0, with a step of 0.2 pH. A pH table, Table 10, list the values obtained for each level of absorption/transmittance.

Table 10 - Transmittance and absorption values for the buffer solutions in the pH range 6.0 - 8.0, with a step of pH 0.2 obtained with the sensor.

pH	Transmittance (%)	Absorption (%)
6.0	100	0
6.2	99	1
6.4	98.5	1.5
6.6	98	2
6.8	97	3
7.0	95.5	4.5
7.2	93	7
7.4	91	9
7.6	89	11
7.8	86	14
8.0	83	17

A signal regression model, represented as the dot blue line in Figure 74, was applied to the data and shows a good accuracy (pH 6.0 – 8.0, $R^2 = 0.936$). As a result, the linear fit may offer a simpler model for pH estimations in this sensor. This will depend upon the desired conditions and operation of the sensor. It has a sensitivity of 8.5%/pH (1.7%/step), in terms of transmittance response, with step of 0.2 pH units.

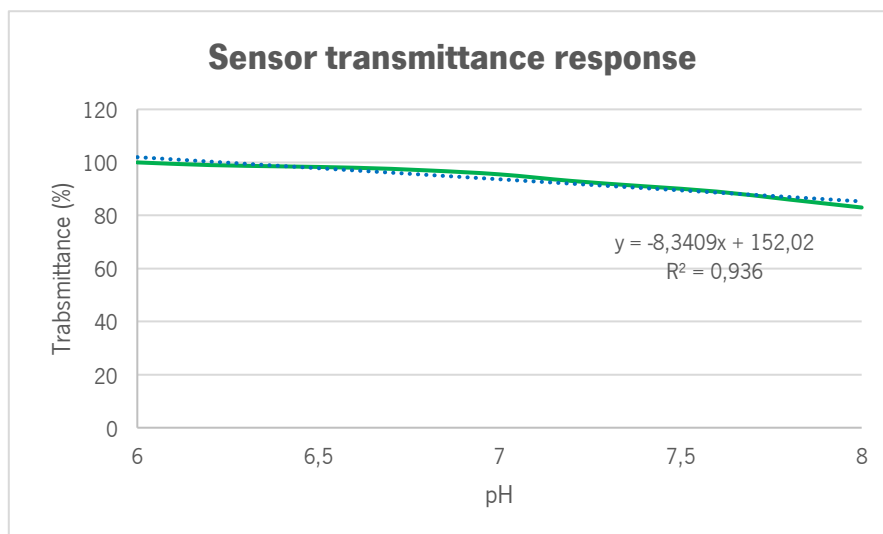
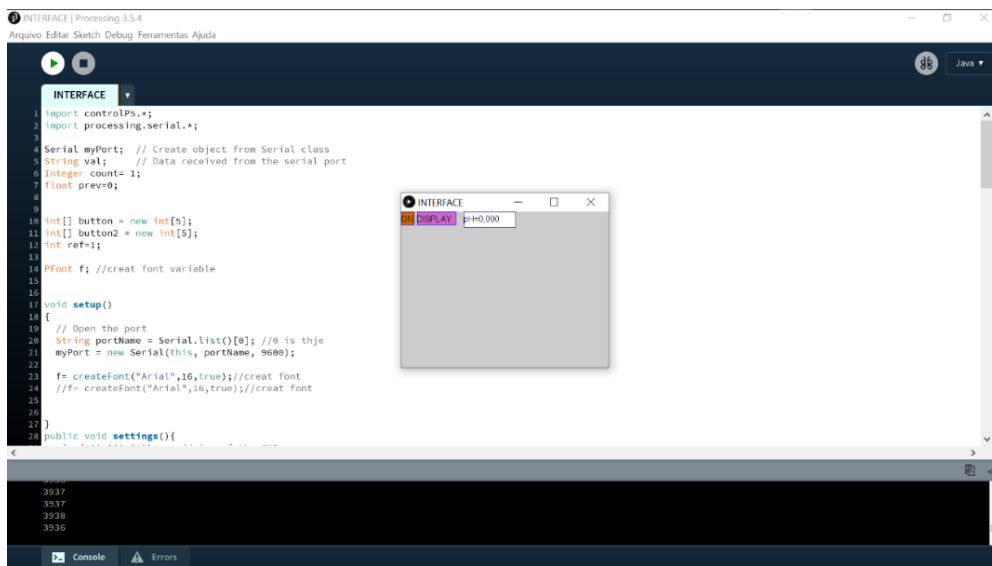


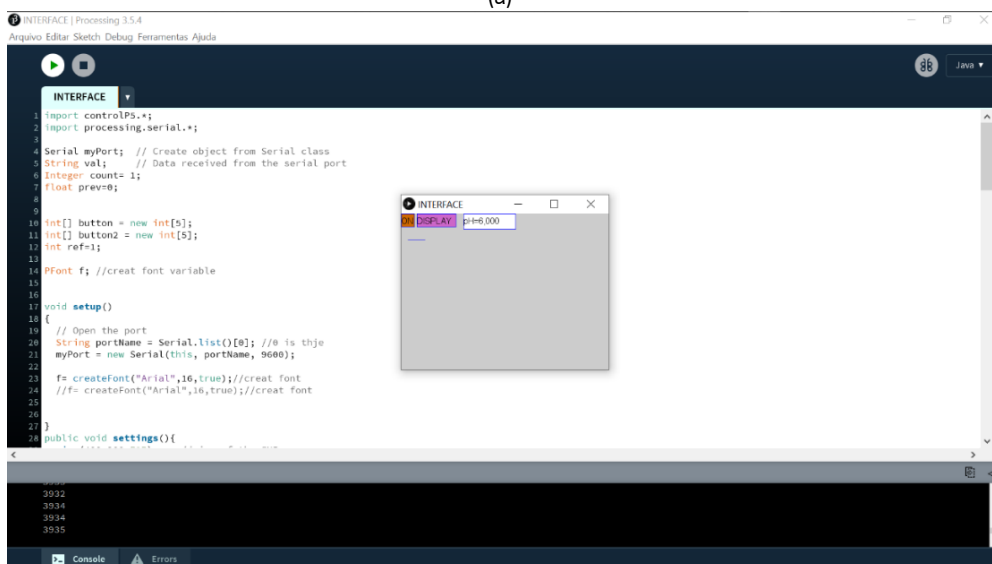
Figure 74 - Sensor transmittance response over the range pH 6.0 - 8.0, with a sensitivity of 1.7%/0.2 pH and a linear regression that shows an accuracy around 94% .

4.7.4. User interface

After the values that each solution presents in the sensor are known, it is possible to calibrate the sensor, according to the sub-chapter 4.5. Therefore, to each interval of the variable "g" of the interface code, the transmittance values obtained in the final measurements are assigned. It is possible to prove that the sensor works, and that the user obtains the sample pH response, as well as the behaviour of the sample transmittance throughout the measurements. In Figure 75(a) it is observed that the read pH is 0 by default, as it is not making measurements. Introducing pure water into the microchamber is verified that the read value is the pH 6.0 with the highest possible transmittance, Figure 75(b).



(a)



(b)

Figure 75 - Interface aspect for (a) solution with pH outside the pH 6.0-8.0 range, and for (b) the zero level (pH=6.0).

Chapter V - Conclusion and Future applications

5.1. Final remarks

The purpose of this project was to develop an optical sensor, with the potentiality to be further integrated in an Organ-on-a-Chip (OoC), capable to measure pH in a range between 6.0 - 8.0 with pH steps of 0.2, in a 1 mm microchamber, using spectrophotometry, especial optical absorption. The microchamber defines the volume where the medium for cell culture can flow to feed the tissues or organs being cultured. To achieve the objective of the work, buffer solutions with a colorimetric indicator, phenol red, were used. The concentration of phenol red in the solutions was selected to be the same as the one found in the commercial culture cell media.

To study the optical absorption and transmittance behaviour for solutions with different pH, a 1 mm deep PMMA microchamber was fabricated using the micromilling process. Every fabrication process has challenges and limitations that need to be addressed. Over this milling process a few challenges and setbacks appeared as expected. During the procedure, there were problems with broken tools and irregular microchannels during the milling. The zero on *z* axis sometimes was not defined with accuracy, the speed configuration during the NC coding and insufficient application of cooling agent, led to the most seen errors.

One of the major problems in using PMMA microdevices, such as the microchambers used in this research, is the appearance of several bubbles, which make it difficult to read assays without disturbances and associated errors. After several experiments with the 1 mm microchamber, which led to the presentation of a stable transmittance reading in this study, it was understood that the optical path needed to be increased. Increasing the optical path leads to an increase in the intensity readings and a higher difference in transmittance between different solutions with different pH and, consequently, the accuracy that a sensor can measure is improved as well. Therefore, the same study was done for a 2 mm microchamber to prove the veracity of this idea.

After it was proven that the optical path of the pH sensor, integrated in a 1 mm microchannel, was not sufficient to have a signal difference between the transmittance value read in the pH range of interest tested with different buffer solutions, it was necessary to think and study an innovative setup where we could increase the optical path in the microchamber without change the settled dimensions. From this need emerged a beam-splitter setup with incorporation of a mirror. Without changes in the 1 mm microchamber, we were able to acquire the same values that are read in a 2 mm microchamber.

In the elaboration of this sensor, were present many processes and studies. The choice of light source was crucial for the advance of the initial readings in the microchambers. When it was defined that a white light LED would be used as the light source, the optical fibers and the DH-MINI Ocean Optics UV-VIS-NIR Fiver Optic Light Source could be used, because the behaviour is identical, on the grounds that both are white light sources. The signal acquisition was made with a revolutionary photodetector already present in an Adafruit digital sensor. The implementation of this type of digital detection in the sensor makes this innovative and easy to project. There have been several *Eagle* PCB design and subsequent soldering of components, in laboratory work. The acquisition of signal to the computer to read was done between Adafruit AS7262 and an Arduino Micro board, which is easy to program with existing libraries.

The choice of a NanoBank structure allowed us to reduce the sensor size to a few small units in centimetres that can be implemented in a future OoC device. An interface was later created in Processing so that each transmittance value was related to a pH level. It was possible to quantify, with the buffers used, pH below the commercial range (6.8 - 8.2), using only the green wavelength range of the Adafruit AS7262 photodetector chip with a sensitivity of 8.5%/pH in terms of transmittance response.

This sensor can in the future be applied for measurements of other parameters than pH (such as presence of nano-waste in fluids) and applied to many more devices in addition to OoC, as it is a sensor that can be easily calibrated and then the transmittance read value can be related to a new characteristic via the interface created for the user. A sensor based on the beam-splitter phenomenon makes this a type of sensor very interesting to be implemented in advanced microfluidic devices, thus to be further studied and improved.

References

- Abitan, H., Bohr, H., & Buchhave, P. (2008). Correction to the Beer-Lambert-Bouguer law for optical absorption. *Applied Optics*, 47(29), 5354–5357. <https://doi.org/10.1364/AO.47.005354>
- Absolonova, M., Beilby, M. J., Sommer, A., Hoepflinger, M. C., & Foissner, I. (2018). Surface pH changes suggest a role for H⁺/OH⁻ channels in salinity response of *Chara australis*. *Protoplasma*, 255(3), 851–862. <https://doi.org/10.1007/s00709-017-1191-z>
- Abu-Thabit, N. Y. (2018). Near-Infrared pH Sensor Based on a SPEEK–Polyaniline Polyelectrolyte Complex Membrane. *Proceedings*. https://doi.org/10.3390/iocn_2018-1-05493
- AG, A. (2014). Arduino Micro. *Arduino-ArduinoBoardMicro*, Cdc, 1–7. <https://doi.org/10.1007/s13398-014-0173-7.2>
- Ahadian, S., Civitarese, R., Bannerman, D., Mohammadi, M. H., Lu, R., Wang, E., Davenport-Huyer, L., Lai, B., Zhang, B., Zhao, Y., Mandla, S., Korolj, A., & Radisic, M. (2018). Organ-On-A-Chip Platforms: A Convergence of Advanced Materials, Cells, and Microscale Technologies. In *Advanced Healthcare Materials*. <https://doi.org/10.1002/adhm.201700506>
- Al-Qaysi, W. W., & Duerkop, A. (2019). Sensor and sensor microtiterplate with expanded pH detection range and their use in real samples. *Sensors and Actuators, B: Chemical*. <https://doi.org/10.1016/j.snb.2019.126848>
- Alam, A. U., Qin, Y., Nambiar, S., Yeow, J. T. W., Howlader, M. M. R., Hu, N. X., & Deen, M. J. (2018). Polymers and organic materials-based pH sensors for healthcare applications. In *Progress in Materials Science*. <https://doi.org/10.1016/j.pmatsci.2018.03.008>
- Alemohammad, H., Liang, R., Yilman, D., Azhari, A., Mathers, K., Chang, C., Chan, B., & Pope, M. A. (2018). Fiber optic sensors for harsh environments: Environmental, hydrogeological, and chemical sensing applications. *Optics InfoBase Conference Papers*. <https://doi.org/10.1364/ofs.2018.tub4>
- Altuglas International. (2006). *Plexyglass Acrylic Sheet Information and Physical Properties*. <http://www.plexiglas.com/export/sites/plexiglas/.content/medias/downloads/sheet-docs/plexiglas-general-information-and-physical-properties.pdf>
- ams AG. (2016). *6-Channel Visible*. 1–47.

Antohe, V. A., Radu, A., & Stefan, M. (2011). Circuit Modeling on Polyaniline Functionalized Capacitors for pH Sensing. *IEEE Transactions on Nanotechnology*. <https://doi.org/10.1109/TNANO.2011.2136384>

Aoi, W., & Marunaka, Y. (2014). Importance of pH Homeostasis in Metabolic Health and Diseases: Crucial Role of Membrane Proton Transport. In *BioMed Research International*. <https://doi.org/10.1155/2014/598986>

Arifin, A., Hardianti, Yunus, M., & Dewang, S. (2019). Application of plastic optical fiber material as pH measurement sensor using loop configuration. *Journal of Physics: Conference Series*. <https://doi.org/10.1088/1742-6596/1317/1/012047>

Ave, D. (n.d.). *DH - mini UV - Vis - NIR Deuterium - Halogen Light Source with Shutter Installation and Operation Manual*.

Axner, O., Schmidt, F. M., Foltynowicz, A., Gustafsson, J., Omenetto, N., & Winefordner, J. D. (2006). Absorption spectrometry by narrowband light in optically saturated and optically pumped collision and doppler broadened gaseous media under arbitrary optical thickness conditions. *Applied Spectroscopy*. <https://doi.org/10.1366/000370206778999049>

Ayuso, J. M., Virumbrales-Munoz, M., McMinn, P. H., Rehman, S., Gomez, I., Karim, M. R., Trusttchel, R., Wisinski, K. B., Beebe, D. J., & Skala, M. C. (2019). Tumor-on-A-chip: A microfluidic model to study cell response to environmental gradients. *Lab on a Chip*, *19*(20), 3461–3471. <https://doi.org/10.1039/c9lc00270g>

Barczak, M., McDonagh, C., & Wencel, D. (2016). Micro- and nanostructured sol-gel-based materials for optical chemical sensing (2005–2015). In *Microchimica Acta*. <https://doi.org/10.1007/s00604-016-1863-y>

Barkoula, N. M., Alcock, B., Cabrera, N. O., & Peijs, T. (2008). Flame-Retardancy Properties of Intumescent Ammonium Poly(Phosphate) and Mineral Filler Magnesium Hydroxide in Combination with Graphene. *Polymers and Polymer Composites*, *16*(2), 101–113. <https://doi.org/10.1002/pc>

Basel, C. L., Defreese, J. D., & Whittemore, D. O. (1982). Interferences in Automated Phenol Red Method for Determination of Bromide in Water. *Analytical Chemistry*. <https://doi.org/10.1021/ac00249a041>

Bassous, E., Taub, H. H., & Kuhn, L. (1977). Ink jet printing nozzle arrays etched in silicon. *Applied*

Physics Letters. <https://doi.org/10.1063/1.89587>

Belattar, S., Debbache, N., Ghoul, I., Sehili, T., & Abdessemed, A. (2018). Photodegradation of phenol red in the presence of oxyhydroxide of Fe(III) (Goethite) under artificial and a natural light. *Water and Environment Journal*. <https://doi.org/10.1111/wej.12333>

Bergveld, P. (2003). Thirty years of ISFETOLOGY: What happened in the past 30 years and what may happen in the next 30 years. *Sensors and Actuators, B: Chemical*. [https://doi.org/10.1016/S0925-4005\(02\)00301-5](https://doi.org/10.1016/S0925-4005(02)00301-5)

Bernini, U., Carbonara, G., Malinconico, M., Mormile, P., Russo, P., & Volpe, M. G. (1992). Investigation of the optothermal properties of a new polymeric blend: polymethyl-methacrylate–poly(ethylene-co-vinylacetate). *Applied Optics*. <https://doi.org/10.1364/ao.31.005794>

Berthois, Y., Katzenellenbogen, J. A., & Katzenellenbogen, B. S. (1986). Phenol red in tissue culture media is a weak estrogen: Implications concerning the study of estrogen-responsive cells in culture. *Proceedings of the National Academy of Sciences of the United States of America*. <https://doi.org/10.1073/pnas.83.8.2496>

Boysen, R. I., Schwarz, L. J., Nicolau, D. V., & Hearn, M. T. W. (2017). Molecularly imprinted polymer membranes and thin films for the separation and sensing of biomacromolecules. In *Journal of Separation Science*. <https://doi.org/10.1002/jssc.201600849>

Capel-Cuevas, S., Cuéllar, M. P., de Orbe-Payá, I., Pegalajar, M. C., & Capitán-Vallvey, L. F. (2010). Full-range optical pH sensor based on imaging techniques. *Analytica Chimica Acta*, 681(1–2), 71–81. <https://doi.org/10.1016/j.aca.2010.09.033>

Cogan, D., Cleary, J., Fay, C., Rickard, A., Jankowski, K., Phelan, T., Bowkett, M., & Diamond, D. (2014). The development of an autonomous sensing platform for the monitoring of ammonia in water using a simplified Berthelot method. *Analytical Methods*. <https://doi.org/10.1039/c4ay01359j>

Cuypers, P., Stephen, A., von Freyberg, A., Goch, G., & Vollertsen, F. (2010). Modellgestützte prozessplanung zur laserchemischen herstellung von mikroumformwerkzeugen. *Technisches Messen*. <https://doi.org/10.1524/teme.2010.0053>

Czugala, M., Fay, C., O'Connor, N. E., Corcoran, B., Benito-Lopez, F., & Diamond, D. (2013). Portable integrated microfluidic analytical platform for the monitoring and detection of nitrite.

Talanta. <https://doi.org/10.1016/j.talanta.2013.07.058>

Davies-Colley, R. J., & Vant, W. N. (1987). Absorption of light by yellow substance in freshwater lakes. *Limnology and Oceanography*. <https://doi.org/10.4319/lo.1987.32.2.0416>

De Los Ríos, A. P., & Fernández, F. J. H. (2014). Ionic Liquids in Separation Technology. In *Ionic Liquids in Separation Technology*. <https://doi.org/10.1016/C2013-0-00056-4>

Del Pup, L., Belloni, A. S., Carraro, G., De Angeli, S., Parnigotto, P. P., & Nussdorfer, G. G. (2003). Adrenomedullin is expressed in cord blood hematopoietic cells and stimulates their clonal growth. *International Journal of Molecular Medicine*. <https://doi.org/10.3892/ijmm.11.2.157>

Donald Voet, Judith G. Voet, C. W. P.-S. C. to A. F. of B. (2012). (2016). Fundamentals of Biochemistry; Life At The Molecular Level. In *Wiley*.

Edmondson, R., Broglie, J. J., Adcock, A. F., & Yang, L. (2014). Three-dimensional cell culture systems and their applications in drug discovery and cell-based biosensors. In *Assay and Drug Development Technologies*. <https://doi.org/10.1089/adt.2014.573>

Ejeian, F., Azadi, S., Razmjou, A., Orooji, Y., Kottapalli, A., Ebrahimi Warkiani, M., & Asadnia, M. (2019). Design and applications of MEMS flow sensors: A review. In *Sensors and Actuators, A: Physical*. <https://doi.org/10.1016/j.sna.2019.06.020>

Fleischer, J., & Kotschenreuther, J. (2007). The manufacturing of micro molds by conventional and energy-assisted processes. *International Journal of Advanced Manufacturing Technology*. <https://doi.org/10.1007/s00170-006-0596-1>

Florea, L., Fay, C., Lahiff, E., Phelan, T., O'Connor, N. E., Corcoran, B., Diamond, D., & Benito-Lopez, F. (2013). Dynamic pH mapping in microfluidic devices by integrating adaptive coatings based on polyaniline with colorimetric imaging techniques. *Lab on a Chip*. <https://doi.org/10.1039/c2lc41065f>

Fonollosa, J., Fernández, L., Gutiérrez-Gálvez, A., Huerta, R., & Marco, S. (2016). Calibration transfer and drift counteraction in chemical sensor arrays using Direct Standardization. *Sensors and Actuators, B: Chemical*. <https://doi.org/10.1016/j.snb.2016.05.089>

Freeman, M. L., Raaphorst, G. P., Hopwood, L. E., & Dewey, W. C. (1980). The effect of pH on cell lethality induced by hyperthermic treatment. *Cancer*. [https://doi.org/10.1002/1097-0142\(19800501\)45:9<2291::AID-CNCR2820450912>3.0.CO;2-X](https://doi.org/10.1002/1097-0142(19800501)45:9<2291::AID-CNCR2820450912>3.0.CO;2-X)

- Friedrich, C. R., & Vasile, M. J. (1996). Development of the micromilling process for high-aspect-ratio microstructures. *Journal of Microelectromechanical Systems*. <https://doi.org/10.1109/84.485213>
- Gaur, S. S., Singh, P. K., Gupta, A., Singh, R., & Kumar, Y. (2018). Synthesis and Analysis of Planar Optical Waveguides as pH Sensors. *Recent Innovations in Chemical Engineering (Formerly Recent Patents on Chemical Engineering)*. <https://doi.org/10.2174/2405520411666180306155326>
- Gerischer, H. (1963). Reference Electrodes: Theory and Practice, herausgeg. von D. J. G. Ives und G. J. Janz. Academic Press, New York—London 1961. 1. Aufl., XI, 651 S., zahlr. Abb. und Tab., geb. £ 7.3.—. *Angewandte Chemie*. <https://doi.org/10.1002/ange.19630751838>
- Geschke, O., Klank, H., & Tellemann, P. (2004). Microsystem Engineering of Lab-on-a-Chip Devices. In *Engineering*. <https://doi.org/10.1373/clinchem.2004.033696>
- Ghadi, H., Murkute, P., Patil, S., & Chakrabarti, S. (2020). Zinc Magnesium Oxide-Based Nanorods for High-Precision pH Sensing. *IEEE Sensors Journal*. <https://doi.org/10.1109/JSEN.2020.2964995>
- Gicevicius, M., Kucinski, J., Ramanaviciene, A., & Ramanavicius, A. (2019). Tuning the optical pH sensing properties of polyaniline-based layer by electrochemical copolymerization of aniline with o-phenylenediamine. *Dyes and Pigments*. <https://doi.org/10.1016/j.dyepig.2019.04.002>
- Gill, E., Arshak, K., Arshak, A., & Korostynska, O. (2008). Mixed metal oxide films as pH sensing materials. *Microsystem Technologies*. <https://doi.org/10.1007/s00542-007-0435-9>
- Gillies, R. J., Verduzco, D., & Gatenby, R. A. (2012). Evolutionary dynamics of carcinogenesis and why targeted therapy does not work. *Nature Reviews Cancer*, *12*(7), 487–493. <https://doi.org/10.1038/nrc3298>
- Gong, J., & Krishnan, S. (2019). Mathematical modeling of dye-sensitized solar cells. In *Dye-Sensitized Solar Cells: Mathematical Modelling, and Materials Design and Optimization*. <https://doi.org/10.1016/B978-0-12-814541-8.00002-1>
- Gorji, M., Sadeghianmaryan, A., Rajabinejad, H., Nasherolahkam, S., & Chen, X. (2019). Development of highly pH-sensitive hybrid membranes by simultaneous electrospinning of amphiphilic nanofibers reinforced with graphene oxide. *Journal of Functional Biomaterials*. <https://doi.org/10.3390/jfb10020023>

- Gotor, R., Ashokkumar, P., Hecht, M., Keil, K., & Rurack, K. (2017). Optical pH Sensor Covering the Range from pH 0-14 Compatible with Mobile-Device Readout and Based on a Set of Rationally Designed Indicator Dyes. *Analytical Chemistry*. <https://doi.org/10.1021/acs.analchem.7b01903>
- Granja, S., Tavares-Valente, D., Queirós, O., & Baltazar, F. (2017). Value of pH regulators in the diagnosis, prognosis and treatment of cancer. In *Seminars in Cancer Biology*. <https://doi.org/10.1016/j.semcancer.2016.12.003>
- Grayson, A. C. R., Shawgo, R. S., Johnson, A. M., Flynn, N. T., Li, Y., Cima, M. J., & Langer, R. (2004). A BioMEMS review: MEMS technology for physiologically integrated devices. *Proceedings of the IEEE*. <https://doi.org/10.1109/JPROC.2003.820534>
- Ham, R. G., & McKeenan, W. L. (1979). [5] Media and growth requirements. *Methods in Enzymology*, 58, 44–93. [https://doi.org/10.1016/S0076-6879\(79\)58126-9](https://doi.org/10.1016/S0076-6879(79)58126-9)
- Harink, B., Le Gac, S., Truckenmüller, R., Van Blitterswijk, C., & Habibovic, P. (2013). Regeneration-on-a-chip? the perspectives on use of microfluidics in regenerative medicine. *Lab on a Chip*, 13(18), 3512–3528. <https://doi.org/10.1039/c3lc50293g>
- Hasanah, U., Setyowati, M., Efendi, R., Muslem, M., Md Sani, N. D., Safitri, E., Heng, L. Y., & Idroes, R. (2019). Preparation and characterization of a pectin membrane-based optical pH sensor for fish freshness monitoring. *Biosensors*. <https://doi.org/10.3390/bios9020060>
- Howe, R. T., & Muller, R. S. (1986). Resonant-Microbridge Vapor Sensor. *IEEE Transactions on Electron Devices*. <https://doi.org/10.1109/T-ED.1986.22519>
- Huang, W. D., Cao, H., Deb, S., Chiao, M., & Chiao, J. C. (2011). A flexible pH sensor based on the iridium oxide sensing film. In *Sensors and Actuators, A: Physical*. <https://doi.org/10.1016/j.sna.2011.05.016>
- Huang, X., & Brittain, W. J. (2001). Synthesis and characterization of PMMA nanocomposites by suspension and emulsion polymerization. *Macromolecules*. <https://doi.org/10.1021/ma001670s>
- Hughes, H. K. (1963). Beer's Law and the Optimum Transmittance in Absorption Measurements. *Applied Optics*. <https://doi.org/10.1364/ao.2.000937>
- Hupert, M. L., Guy, W. J., Llopis, S. D., Shadpour, H., Rani, S., Nikitopoulos, D. E., & Soper, S. A. (2007). Evaluation of micromilled metal mold masters for the replication of microchip

electrophoresis devices. *Microfluidics and Nanofluidics*. <https://doi.org/10.1007/s10404-006-0091-x>

Ian Freshney, R. (2015). Culture of Animal Cells - A Manual of Basic Technique and Specialized Applications: In *John Wiley & Sons, Incorporated*.

Islam, S., Bakhtiar, H., Shukri, W. N. W., Aziz, M. S. abd, Riaz, S., & Naseem, S. (2019). Optically active-thermally stable multi-dyes encapsulated mesoporous silica aerogel: A potential pH sensing nanomatrix. *Microporous and Mesoporous Materials*. <https://doi.org/10.1016/j.micromeso.2018.07.049>

Islam, S., Bidin, N., Riaz, S., Krishnan, G., & Naseem, S. (2016). Sol-gel based fiber optic pH nanosensor: Structural and sensing properties. *Sensors and Actuators, A: Physical*. <https://doi.org/10.1016/j.sna.2015.12.003>

Jin, Z., Su, Y., & Duan, Y. (2000). Improved optical pH sensor based on polyaniline. *Sensors and Actuators, B: Chemical*, 71(1–2), 118–122. [https://doi.org/10.1016/S0925-4005\(00\)00597-9](https://doi.org/10.1016/S0925-4005(00)00597-9)

John M. Senior. (2009). Optical Fiber Communications Principles and Practice Third Edition. In *Online Information Review*. <https://doi.org/10.1108/14684520710747257>

Joshi, V. S., Sheet, P. S., Cullin, N., Kreth, J., & Koley, D. (2017). Real-Time Metabolic Interactions between Two Bacterial Species Using a Carbon-Based pH Microsensor as a Scanning Electrochemical Microscopy Probe. *Analytical Chemistry*. <https://doi.org/10.1021/acs.analchem.7b03050>

Jović, M., Hidalgo-Acosta, J. C., Lesch, A., Costa Bassetto, V., Smirnov, E., Cortés-Salazar, F., & Girault, H. H. (2018). Large-scale layer-by-layer inkjet printing of flexible iridium-oxide based pH sensors. *Journal of Electroanalytical Chemistry*. <https://doi.org/10.1016/j.jelechem.2017.11.032>

Kakkar, A., Traverso, G., Farokhzad, O. C., Weissleder, R., & Langer, R. (2017). Evolution of macromolecular complexity in drug delivery systems. In *Nature Reviews Chemistry*. <https://doi.org/10.1038/s41570-017-0063>

Kazushige Sogawa, and M. D. P. (1970). NII-Electronic Library Service. *Chemical Pharmaceutical Bulletin*, 43, 2091. <http://www.mendeley.com/research/geology-volcanic-history-eruptive-style-yakedake-volcano-group-central-japan/>

- Kermis, H. R., Kostov, Y., & Rao, G. (2003). Rapid method for the preparation of a robust optical pH sensor. *Analyst*, *128*(9), 1181–1186. <https://doi.org/10.1039/b304902g>
- Kocsis, L., Herman, P., & Eke, A. (2006). The modified Beer-Lambert law revisited. *Physics in Medicine and Biology*. <https://doi.org/10.1088/0031-9155/51/5/N02>
- Korostynska, O., Arshak, K., Gill, E., & Arshak, A. (2007). Review on state-of-the-art in polymer based pH sensors. In *Sensors*.
- Krimpenis, A. A., Fountas, N. A., Ntalianis, I., & Vaxevanidis, N. M. (2014). CNC micromilling properties and optimization using genetic algorithms. *International Journal of Advanced Manufacturing Technology*. <https://doi.org/10.1007/s00170-013-5248-7>
- Kubby, J. A. (2011). A Guide to Hands-on MEMS Design and Prototyping. In *A Guide to Hands-on MEMS Design and Prototyping*. <https://doi.org/10.1017/cbo9780511984662>
- Kurzweil, P. (2009). Metal oxides and ion-exchanging surfaces as pH sensors in liquids: State-of-the-art and outlook. In *Sensors (Switzerland)*. <https://doi.org/10.3390/s90604955>
- Li, Z., Jupp, D. L. B., Strahler, A. H., Schaaf, C. B., Howe, G., Hewawasam, K., Douglas, E. S., Chakrabarti, S., Cook, T. A., Paynter, I., Saenz, E. J., & Schaefer, M. (2016). Radiometric calibration of a dual-wavelength, full-waveform terrestrial lidar. *Sensors (Switzerland)*. <https://doi.org/10.3390/s16030313>
- LINOS Microbench, Bench and Rail Systems*. (n.d.). www.qioptiq-shop.com.
- Liu, X., Su, Y., Tian, H., Yang, L., Zhang, H., Song, X., & Foley, J. W. (2017). Ratiometric Fluorescent Probe for Lysosomal pH Measurement and Imaging in Living Cells Using Single-Wavelength Excitation. *Analytical Chemistry*. <https://doi.org/10.1021/acs.analchem.7b00754>
- Madou, M., & Morrison, S. (1989). Chemical Sensing with Solid State Devices. In *Chemical Sensing with Solid State Devices*. <https://doi.org/10.1016/c2009-0-22258-6>
- Mahboubeh Vafi, Rounaghi, G. H., Es'haghi, Z., & Moradi, Z. (2019). Design and Application of an Optical pH Sensor Based on Thionine Doped Modified Sol–Gel Film. *Russian Journal of Physical Chemistry A*. <https://doi.org/10.1134/S0036024419070173>
- Mallik, S., Chowdhury, D., & Chhstopadhyay, M. (2019). Development and performance analysis of a low-cost MEMS microphone-based hearing aid with three different audio amplifiers. *Innovations*

in Systems and Software Engineering. <https://doi.org/10.1007/s11334-019-00325-7>

Manjakkal, L., Cvejic, K., Kulawik, J., Zaraska, K., & Szwagierczak, D. (2014). A comparative study of potentiometric and conductimetric thick film pH Sensors made of RuO₂ Pastes. *Sensor Letters*. <https://doi.org/10.1166/sl.2014.3377>

Manjakkal, L., Shakthivel, D., & Dahiya, R. (2018). Flexible Printed Reference Electrodes for Electrochemical Applications. *Advanced Materials Technologies*. <https://doi.org/10.1002/admt.201800252>

Manjakkal, L., Szwagierczak, D., & Dahiya, R. (2020). Metal oxides based electrochemical pH sensors: Current progress and future perspectives. In *Progress in Materials Science*. <https://doi.org/10.1016/j.pmatsci.2019.100635>

Mersagh Dezfuli, S., & Sabzi, M. (2019). Deposition of self-healing thin films by the sol–gel method: a review of layer-deposition mechanisms and activation of self-healing mechanisms. *Applied Physics A: Materials Science and Processing*. <https://doi.org/10.1007/s00339-019-2854-8>

Met, A. (1987). *J. M. Bonga et al. (eds.), Cell and Tissue Culture in Forestry © Martinus Nijhoff Publishers, Dordrecht 1987. 56, 92–136.*

Mitschke, F. (2010). Fiber optics: Physics and technology. In *Fiber Optics: Physics and Technology*. <https://doi.org/10.1007/978-3-642-03703-0>

Mittal, A., Kaur, D., Malviya, A., Mittal, J., & Gupta, V. K. (2009). Adsorption studies on the removal of coloring agent phenol red from wastewater using waste materials as adsorbents. *Journal of Colloid and Interface Science*. <https://doi.org/10.1016/j.jcis.2009.05.016>

Mohan, C. (2003). <Buffers_Calbiochem.Pdf>. *Calbiochem*.

Moldes, D., Lorenzo, M., & Sanromán, M. Á. (2004). Degradation or polymerisation of Phenol Red dye depending to the catalyst system used. *Process Biochemistry*. <https://doi.org/10.1016/j.procbio.2003.09.004>

Morris, D., Coyle, S., Wu, Y., Lau, K. T., Wallace, G., & Diamond, D. (2009). Bio-sensing textile based patch with integrated optical detection system for sweat monitoring. *Sensors and Actuators, B: Chemical*. <https://doi.org/10.1016/j.snb.2009.02.032>

Morsy, M. K., Zór, K., Kostesha, N., Alstrøm, T. S., Heiskanen, A., El-Tanahi, H., Sharoba, A.,

Papkovsky, D., Larsen, J., Khalaf, H., Jakobsen, M. H., & Emnéus, J. (2016). Development and validation of a colorimetric sensor array for fish spoilage monitoring. *Food Control*. <https://doi.org/10.1016/j.foodcont.2015.07.038>

Moya, M., Tran, D., & George, S. C. (2013). An integrated in vitro model of perfused tumor and cardiac tissue. *Stem Cell Research and Therapy*, 4(SUPPL.1), 1–6. <https://doi.org/10.1186/scrt376>

Novak, L., Neuzil, P., Pipper, J., Zhang, Y., & Lee, S. (2007). An integrated fluorescence detection system for lab-on-a-chip applications. *Lab on a Chip*. <https://doi.org/10.1039/b611745g>

Ozturk, S. S., & Palsson, B. O. (1990). Chemical Decomposition of Glutamine in Cell Culture Media: Effect of Media Type, pH, and Serum Concentration. *Biotechnology Progress*. <https://doi.org/10.1021/bp00002a005>

Park, H. J., Yoon, J. H., Lee, K. G., & Choi, B. G. (2019). Potentiometric performance of flexible pH sensor based on polyaniline nanofiber arrays. *Nano Convergence*. <https://doi.org/10.1186/s40580-019-0179-0>

Pawar, E. (2016). A Review Article on Acrylic PMMA. *IOSR Journal of Mechanical and Civil Engineering (IOSR-JMCE) e-ISSN*. <https://doi.org/10.1182/blood-2006-06-029850>.The

Pcr, A., & Kit, L. (2012). Data Sheet Data Sheet. *고생물학회지*, September 2004, 0–1. http://www.papersearch.net/view/detail.asp?detail_key=10000715

Perez De Vargas Sansalvador, I. M., Fay, C. D., Cleary, J., Nightingale, A. M., Mowlem, M. C., & Diamond, D. (2016). Autonomous reagent-based microfluidic pH sensor platform. *Sensors and Actuators, B: Chemical*. <https://doi.org/10.1016/j.snb.2015.11.057>

Persi, E., Duran-Frigola, M., Damaghi, M., Roush, W. R., Aloy, P., Cleveland, J. L., Gillies, R. J., & Ruppin, E. (2018). Systems analysis of intracellular pH vulnerabilities for cancer therapy. *Nature Communications*, 9(1). <https://doi.org/10.1038/s41467-018-05261-x>

Petersen, K. E. (1982). Silicon as a Mechanical Material. *Proceedings of the IEEE*. <https://doi.org/10.1109/PROC.1982.12331>

Phelan, K., & May, K. M. (2017). Mammalian cell tissue culture techniques. *Current Protocols in Molecular Biology*. <https://doi.org/10.1002/cpmb.31>

Pradela-Filho, L. A., Andreotti, I. A. A., Carvalho, J. H. S., Araújo, D. A. G., Orzari, L. O., Gatti, A., Takeuchi, R. M., Santos, A. L., & Janegitz, B. C. (2020). Glass varnish-based carbon conductive ink: A new way to produce disposable electrochemical sensors. *Sensors and Actuators, B: Chemical*. <https://doi.org/10.1016/j.snb.2019.127433>

Press, P. (1991). *Life Sciences, Vol. 48, pp. 245-252 Printed in the U.S.A. Pergamon Press. 48(c), 245–252.*

Qin, Q., Tao, J., & Yang, Y. (2010). Preparation and characterization of polyaniline film on stainless steel by electrochemical polymerization as a counter electrode of DSSC. *Synthetic Metals*. <https://doi.org/10.1016/j.synthmet.2010.03.003>

Qin, Y., Kwon, H. J., Howlader, M. M. R., & Deen, M. J. (2015). Microfabricated electrochemical pH and free chlorine sensors for water quality monitoring: Recent advances and research challenges. In *RSC Advances*. <https://doi.org/10.1039/c5ra11291e>

Ren, Z., Chang, Y., Ma, Y., Shih, K., Dong, B., & Lee, C. (2020). Leveraging of MEMS Technologies for Optical Metamaterials Applications. In *Advanced Optical Materials*. <https://doi.org/10.1002/adom.201900653>

Rodrigues, R. O., Pinho, D., Faustino, V., & Lima, R. (2015). A simple microfluidic device for the deformability assessment of blood cells in a continuous flow. *Biomedical Microdevices*. <https://doi.org/10.1007/s10544-015-0014-2>

Rojas, F. S., Ojeda, C. B., & Pavon, J. M. C. (1988). Derivative ultraviolet-visible region absorption spectrophotometry and its analytical applications. *Talanta*. [https://doi.org/10.1016/0039-9140\(88\)80179-6](https://doi.org/10.1016/0039-9140(88)80179-6)

Rovati, L., Cattini, S., Fabbri, P., & Ferrari, L. (2018). Fluorescence pH Sensor Based on Polymer Film. *2018 International Flexible Electronics Technology Conference, IFETC 2018*. <https://doi.org/10.1109/IFETC.2018.8583976>

Sadig, H. R., & Cheng, L. (2020). Applying a Novel Polymeric Precursor Derived by Capillary-Gravitational Coating in Fabrication of Nanostructured Tri-metal Oxide Based pH Sensing Electrode. *IEEE Sensors Journal*. <https://doi.org/10.1109/jsen.2020.3001310>

Safavi, A., & Bagheri, M. (2003). Novel optical pH sensor for high and low pH values. *Sensors and Actuators, B: Chemical*. [https://doi.org/10.1016/S0925-4005\(03\)00039-X](https://doi.org/10.1016/S0925-4005(03)00039-X)

- Schäferling, M. (2016). Nanoparticle-based luminescent probes for intracellular sensing and imaging of pH. In *Wiley Interdisciplinary Reviews: Nanomedicine and Nanobiotechnology*. <https://doi.org/10.1002/wnan.1366>
- Seifan, M., Samani, A. K., & Berenjian, A. (2017). New insights into the role of pH and aeration in the bacterial production of calcium carbonate (CaCO₃). *Applied Microbiology and Biotechnology*. <https://doi.org/10.1007/s00253-017-8109-8>
- Shaegh, S. A. M., De Ferrari, F., Zhang, Y. S., Nabavinia, M., Mohammad, N. B., Ryan, J., Pourmand, A., Laukaitis, E., Sadeghian, R. B., Nadhman, A., Shin, S. R., Nezhad, A. S., Khademhosseini, A., & Dokmeci, M. R. (2016). A microfluidic optical platform for real-time monitoring of pH and oxygen in microfluidic bioreactors and organ-on-chip devices. *Biomicrofluidics*, 10(4). <https://doi.org/10.1063/1.4955155>
- Shen, C., Zhang, Y., Tang, J., Cao, H., & Liu, J. (2019). Dual-optimization for a MEMS-INS/GPS system during GPS outages based on the cubature Kalman filter and neural networks. *Mechanical Systems and Signal Processing*. <https://doi.org/10.1016/j.ymssp.2019.07.003>
- Shimizu, S., Matsuoka, Y., Shinohara, Y., Yoneda, Y., & Tsujimoto, Y. (2001). Essential role of voltage-dependent anion channel in various forms of apoptosis in mammalian cells. *Journal of Cell Biology*. <https://doi.org/10.1083/jcb.152.2.237>
- Smith, C. S. (1954). Piezoresistance effect in germanium and silicon. *Physical Review*. <https://doi.org/10.1103/PhysRev.94.42>
- Son, M., Ahn, S. J., Guo, Q., Burne, R. A., & Hagen, S. J. (2012). Microfluidic study of competence regulation in *Streptococcus mutans*: Environmental inputs modulate bimodal and unimodal expression of comX. *Molecular Microbiology*. <https://doi.org/10.1111/j.1365-2958.2012.08187.x>
- Sørensen, T. J., Rosenberg, M., Frankær, C. G., & Laursen, B. W. (2019). An Optical pH Sensor Based on Diazaoxatriangulenium and Isopropyl-Bridged Diazatriangulenium Covalently Bound in a Composite Sol–Gel. *Advanced Materials Technologies*. <https://doi.org/10.1002/admt.201800561>
- Spencer Lima, L. (2013). Lei de Lambert–Beer. *Revista de Ciência Elementar*. <https://doi.org/10.24927/rce2013.047>

- Srinivasan Damodaran, Kirk L. Parkin, O. R. F. (2010). Química de los Alimentos de Fennema. In *Química de Alimentos de Fennema*.
- Swinehart, D. F. (1962). The Beer-Lambert law. In *Journal of Chemical Education*.
<https://doi.org/10.1021/ed039p333>
- TAYLOR, A. C. (1962). Responses of cells to pH changes in the medium. *The Journal of Cell Biology*, 15(2), 201–209. <https://doi.org/10.1083/jcb.15.2.201>
- Terry, S. C., Herman, J. H., & Angell, J. B. (1979). A Gas Chromatographic Air Analyzer Fabricated on a Silicon Wafer. *IEEE Transactions on Electron Devices*. <https://doi.org/10.1109/T-ED.1979.19791>
- Timbó, Á. P., Pinto, P. V. F., Pinho, H. A., De Moura, L. P., Chretien, J. B., Viana, F. W., Filho, R. G. D., Da Silva, E. B., Da Silva, M. E. R., Menezes, J. W. M., Guimarães, G. D. F., & Fraga, W. B. (2016). PH optical sensor based on thin films of sol-gel with bromocresol purple. *Sensors and Actuators, B: Chemical*. <https://doi.org/10.1016/j.snb.2015.09.066>
- Ullmann, G. M., & Bombarda, E. (2013). PKa values and redox potentials of proteins. What do they mean? *Biological Chemistry*. <https://doi.org/10.1515/hsz-2012-0329>
- Vis-nir, S. (2020). *Strahlteilerplatten VIS-NIR, rechteckig*. 1–2.
- Vogelmann, T. C., & Evans, J. R. (2002). Profiles of light absorption and chlorophyll within spinach leaves from chlorophyll fluorescence. *Plant, Cell and Environment*.
<https://doi.org/10.1046/j.1365-3040.2002.00910.x>
- Vullev, V. I., Wan, J., Heinrich, V., Landsman, P., Bower, P. E., Xia, B., Millare, B., & Jones, G. (2006). Nonlithographic fabrication of microfluidic devices. *Journal of the American Chemical Society*. <https://doi.org/10.1021/ja061776o>
- Warburg, Posener, N. (1924). Über den Stoffwechsel der Carcinomzelle_Warburg_1924-1.pdf. In *Klin Wochenschr Berl* (Vol. 4, pp. 310–343).
- Warrick, J., Meyvantsson, I., Ju, J., & Beebe, D. J. (2007). High-throughput microfluidics: Improved sample treatment and washing over standard wells. *Lab on a Chip*, 7(3), 316–321.
<https://doi.org/10.1039/b613350a>
- Webb, B. A., Chimenti, M., Jacobson, M. P., & Barber, D. L. (2011). Dysregulated pH: A perfect

- storm for cancer progression. *Nature Reviews Cancer*, 11(9), 671–677. <https://doi.org/10.1038/nrc3110>
- Wei, W., Zeng, Z., Liao, W., Chim, W. K., & Zhu, C. (2020). Extended Gate Ion-Sensitive Field-Effect Transistors Using Al₂O₃/Hexagonal Boron Nitride Nanolayers for pH Sensing. *ACS Applied Nano Materials*. <https://doi.org/10.1021/acsnm.9b02037>
- Wencel, D., Abel, T., & McDonagh, C. (2014). Optical chemical pH sensors. In *Analytical Chemistry*. <https://doi.org/10.1021/ac4035168>
- Whitesides, G. M. (2006). The origins and the future of microfluidics. In *Nature*. <https://doi.org/10.1038/nature05058>
- Wikswow, J. P., Curtis, E. L., Eagleton, Z. E., Evans, B. C., Kole, A., Hofmeister, L. H., & Matloff, W. J. (2013). Scaling and systems biology for integrating multiple organs-on-a-chip. *Lab on a Chip*, 13(18), 3496–3511. <https://doi.org/10.1039/c3lc50243k>
- Woolley, J. T. (1971). Reflectance and Transmittance of Light by Leaves. *Plant Physiology*. <https://doi.org/10.1104/pp.47.5.656>
- Works, H. I. (2018). *Buffers for Biochemical Reactions What a Buffer System Is and How It Works What Makes a " Good " Buffer*. 1–13. <https://doi.org/10.3978/j.issn.2072-1439.2014.10.28>
- Worlinsky, J. L., Halepas, S., Ghandehari, M., Khalil, G., & Brückner, C. (2015). High pH sensing with water-soluble porpholactone derivatives and their incorporation into a Nafion® optode membrane. *The Analyst*. <https://doi.org/10.1039/c4an01462f>
- Wu, Lin, J. L., Wang, J., Cui, Z., & Cui, Z. (2009). Development of high throughput optical sensor array for on-line pH monitoring in micro-scale cell culture environment. *Biomedical Microdevices*, 11(1), 265–273. <https://doi.org/10.1007/s10544-008-9233-0>
- Wu, M. H., Urban, J. P. G., Zhan, F. C., Cui, Z., & Xu, X. (2007). Effect of extracellular pH on matrix synthesis by chondrocytes in 3D agarose gel. *Biotechnology Progress*. <https://doi.org/10.1021/bp060024v>
- Wu, S., Lin, Q., Yuen, Y., & Tai, Y. C. (2001). MEMS flow sensors for nano-fluidic applications. *Sensors and Actuators, A: Physical*. [https://doi.org/10.1016/S0924-4247\(00\)00541-0](https://doi.org/10.1016/S0924-4247(00)00541-0)
- Wypych, G. (2018). Handbook of material weathering. In *Handbook of Material Weathering*.

[https://doi.org/10.1016/1352-2310\(96\)90058-8](https://doi.org/10.1016/1352-2310(96)90058-8)

Yadavalli, V. K., & Pishko, M. V. (2004). Biosensing in microfluidic channels using fluorescence polarization. *Analytica Chimica Acta*. <https://doi.org/10.1016/j.aca.2003.12.029>

Yang, M., Li, C. W., & Yang, J. (2002). Cell docking and on-chip monitoring of cellular reactions with a controlled concentration gradient on a microfluidic device. *Analytical Chemistry*. <https://doi.org/10.1021/ac025536c>

Yeh, P., Yeh, N., Lee, C. H., & Ding, T. J. (2017). Applications of LEDs in optical sensors and chemical sensing device for detection of biochemicals, heavy metals, and environmental nutrients. In *Renewable and Sustainable Energy Reviews*. <https://doi.org/10.1016/j.rser.2016.11.011>

Yunus, M., & Arifin, A. (2018). Design of Oil Viscosity Sensor Based on Plastic Optical Fiber. *Journal of Physics: Conference Series*. <https://doi.org/10.1088/1742-6596/979/1/012083>

Zhang, Y., & Chen, X. (2019). Nanotechnology and nanomaterial-based no-wash electrochemical biosensors: From design to application. In *Nanoscale*. <https://doi.org/10.1039/c9nr05696c>

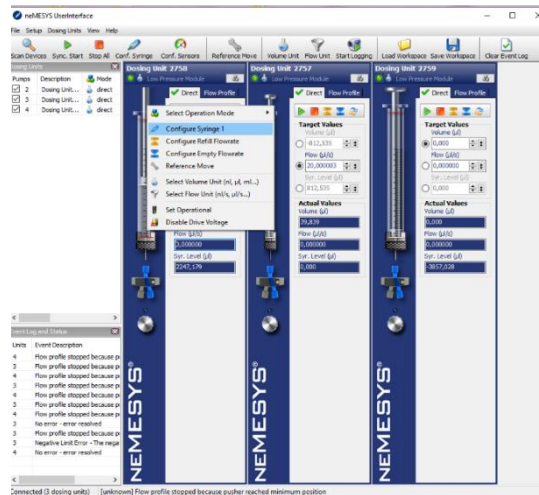
Zhang, Y. S. (2017). Modular multi-organ-on-chips platform with physicochemical sensor integration. *Midwest Symposium on Circuits and Systems, 2017-Augus*, 80–83. <https://doi.org/10.1109/MWSCAS.2017.8052865>

Zhu, J., Wang, H., Zhang, Z., Ren, Z., Shi, Q., Liu, W., & Lee, C. (2020). Continuous direct current by charge transportation for next-generation IoT and real-time virtual reality applications. *Nano Energy*. <https://doi.org/10.1016/j.nanoen.2020.104760>

Appendix I

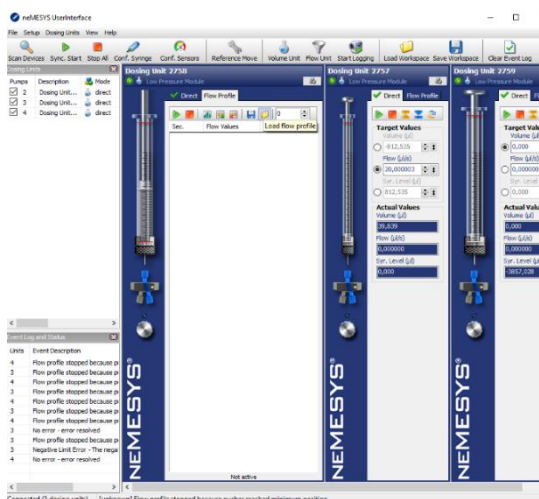
Here is presented the procedure, to a better understanding of the software possibilities, to use the neMESYS syringe pump used to test different types of flow and its behaviour on the mixing channel.

After opening the user interface program, we should start to "Scan Devices", so the program can detect the syringes existing in the neMESYS.

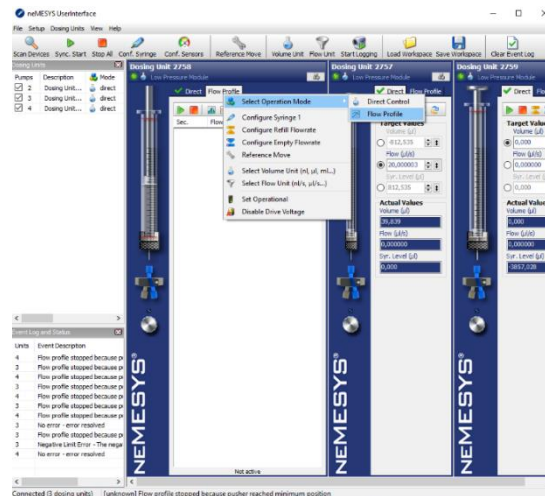


The syringes are assigned, having in consideration their brands and volumes, with a right-click on the name of each of syringe and then "Configure Syringe". If the opened window with numerous sample syringes with associated companies and sizes do not have the syringe that you need, it must be added with the necessary characteristics.

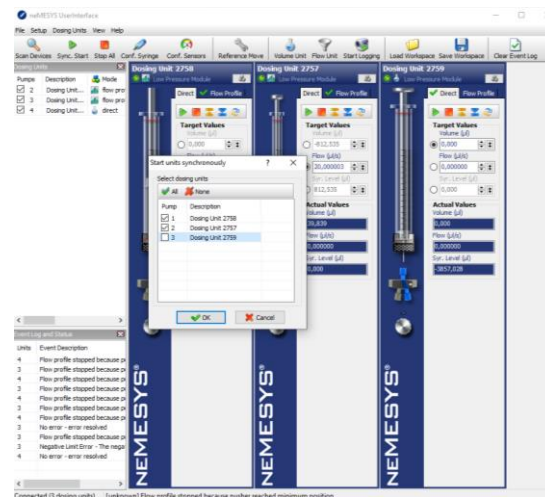
When it's essential to change the names of the syringes so that no misunderstandings occur, you double-click on the source name, and that allows a window, where the name can be changed, to open.



The syringe pump can be operated manually or automatically. To work in automatic mode, you select "Flow Profile" and choose the option "Load Flow Profile", where you going to upload a pre-prepared ".nfp" file, previously prepared, with the times and flow rates, of the individual dosages that you want to work in. This process is repeated to all the of the syringes.

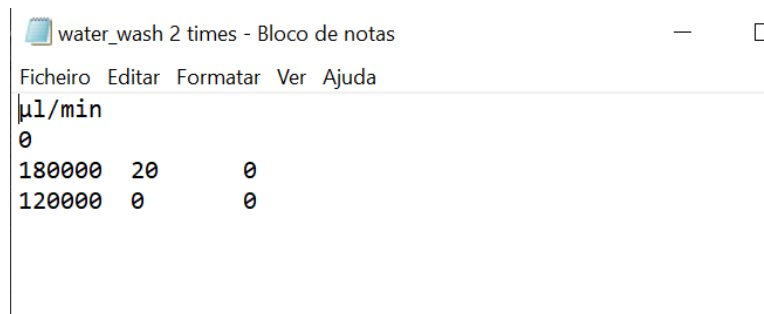


To start the automatic flow profile right click with the mouse on the "Dosing Units" window, making sure that the name of the syringe is green, and a new window will appear. Then you chose the "Select Operation Mode" and then change it to "Flow Profile".



As the desired mode of operation is automatic, click on "Sync Start" and a new window, "Start units synchronously" will appear. You must select the syringes that you want to operate, with a checkmark, and then click "OK". The synchronised start was confirmed, and it will start working.

Description of the execution automatic program:



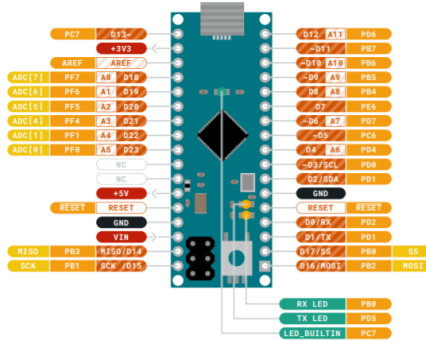
```
water_wash 2 times - Bloco de notas
Ficheiro Editar Formatar Ver Ajuda
µl/min
0
180000 20 0
120000 0 0
```

The first column has the time in μs of each step. The second column has the flow rate of the step. And then the third column has the number 1 or 0, indicating the behavior of the flow. We use both numbers when we want a smart step-up, with a valve. And then, if the 1 is activated the syringe will fill, if not, 0, the liquid will be flushed to the microchannel.

In this case we just have the zero in all the columns, because we don't have a valve and we just want that the liquids go inside of the microchannels to watch the behavior of the flow.

Appendix II

The pinout of the supplier Arduino is shown, embedded in the company website, and the code used to program it.

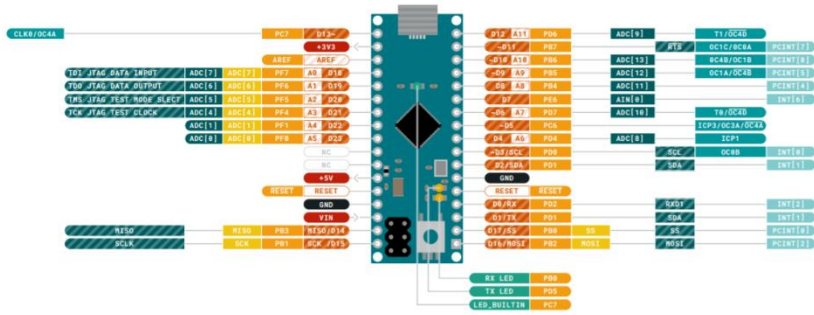


- Ground
- Power
- LED
- Internal Pin
- SWD Pin
- Digital Pin
- Analog Pin
- Other Pin
- Microcontroller's Port
- Default

- ▲ **MAXIMUM** current per I/O pin is 40mA
- ▲ **MAXIMUM** current per +3.3V pin is 50mA
- VIN** 6-20 V input to the board.

ARDUINO . CC
Last update: 23/03/2020

This work is licensed under the Creative Commons Attribution-ShareAlike 4.0 International License. To see a copy of this license, visit <http://creativecommons.org/licenses/by-sa/4.0/> or send a letter to Creative Commons, PO Box 1866, Mountain View, CA 94042, USA.

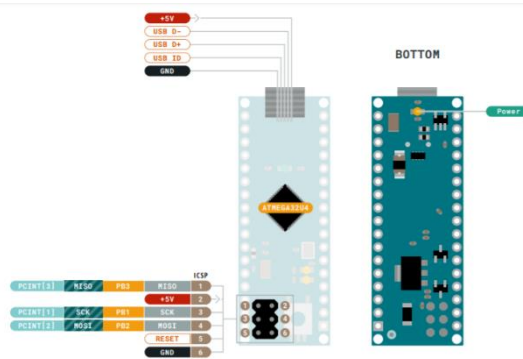


- Ground
- Power
- LED
- Internal Pin
- SWD Pin
- Digital Pin
- Analog Pin
- Other Pin
- Microcontroller's Port
- Default

- ▲ **MAXIMUM** current per I/O pin is 40mA
- ▲ **MAXIMUM** current per +3.3V pin is 50mA
- VIN** 6-20 V input to the board.

ARDUINO . CC
Last update: 23/03/2020

This work is licensed under the Creative Commons Attribution-ShareAlike 4.0 International License. To see a copy of this license, visit <http://creativecommons.org/licenses/by-sa/4.0/> or send a letter to Creative Commons, PO Box 1866, Mountain View, CA 94042, USA.



```
#include <Wire.h>
#include "Adafruit_AS726x.h"

//create the object
Adafruit_AS726x ams;

//buffer to hold raw values
uint16_t sensorValues[AS726x_NUM_CHANNELS];

//buffer to hold calibrated values (not used by default in this
example)
//float calibratedValues[AS726x_NUM_CHANNELS];

void setup() {
  Serial.begin(9600);
  while(!Serial);

  // initialize digital pin LED_BUILTIN as an output.
  pinMode(LED_BUILTIN, OUTPUT);

  //begin and make sure we can talk to the sensor
  if(!ams.begin()){
    Serial.println("could not connect to sensor! Please check your
wiring.");
    while(1);
  }
  ams.setIntegrationTime(100); //this time multiplied by 2.8ms will
be the integration time that the sensor will acquire signal
  //ams.setGain(2); //0:1x 1:3.7x 2:16x 3:64x(power.on default;;
just need to set the gain if it is needed less signal)

  ams.drivOn(); //turn on the LED of the chip 12.5 on default
```

```

ams.setDrvCurrent(0); //0:12.5mA (12.6) 1:25mA (25.32) 2:50mA (too
much) 3:100mA(too much).

//ams.enableIndicator(); //ams.disableIndicator();
//ams.setIndicatorCurrent(0) //0:1mA 1:2mA 2:4mA 3:8mA
//ams.setMeasurementMode(2) //0:continuous reading of VBGY (Visible)/
SRUV (IR) 1:continuous reading of GYor (Visible)/ RTUX
(IR) 2:continuous reading of all channels
//3:one-shot reading of all
channels (power-on default)
}

void loop() {

//read the device temperature
uint8_t temp = ams.readTemperature();

//ams.drivOn(); //uncomment this if you want to use the driver LED
for readings
ams.startMeasurement(); //begin a measurement

//wait till data is available
bool rdy = false;
while(!rdy){
    delay(5);
    rdy = ams.dataReady();
}
//ams.drivOff(); //uncomment this if you want to use the driver LED
for readings

//read the values!
ams.readRawValues(sensorValues);
//ams.readCalibratedValues(calibratedValues);

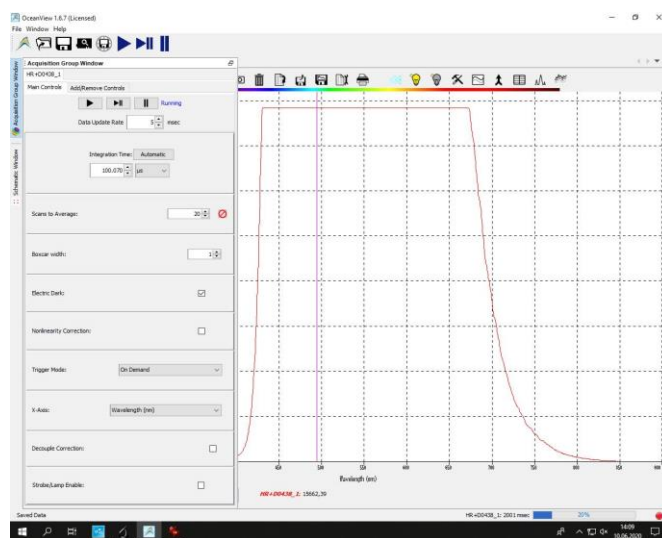
//Serial.print("Temp: "); Serial.print(temp);
//Serial.print(" Violet: ");
//Serial.print(sensorValues[AS726x_VIOLET]);
//Serial.print(" ");
//Serial.print(" Blue: ");
//Serial.print(sensorValues[AS726x_BLUE]);
//Serial.print(" ");
//Serial.print(" Green: ");
Serial.print(sensorValues[AS726x_GREEN]);
Serial.print(" ");
//Serial.print(" Yellow: ");
//Serial.print(sensorValues[AS726x_YELLOW]);
//Serial.print(" ");
//Serial.print(" Orange: ");
//Serial.print(sensorValues[AS726x_ORANGE]);
//Serial.print(" ");
//Serial.print(" Red: ");
//Serial.print(sensorValues[AS726x_RED]);
//Serial.print(" ");
Serial.println();
delay(100);
}

```

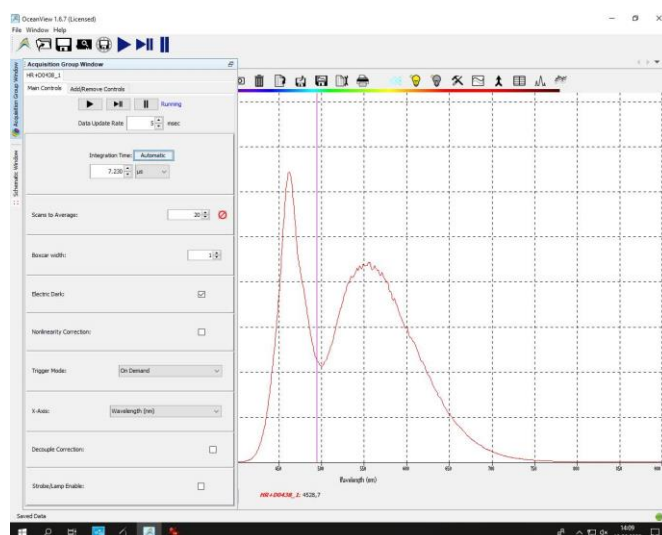
Appendix III

The acquisition of response along the wavelength ranges through *OceanView* is fast and easy.

This is the saturated signal that appears when the software is turned on and the light source (*DH-MINI Ocean Optics UV-VIS-NIR Fiver Optic Light Source*) is on.

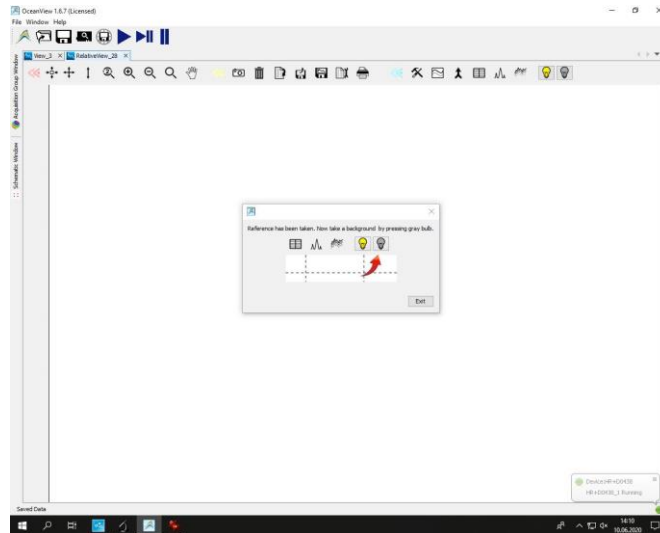


Then in Acquisition Group Window the integration time is set to automatic and 20 scans to average were used.

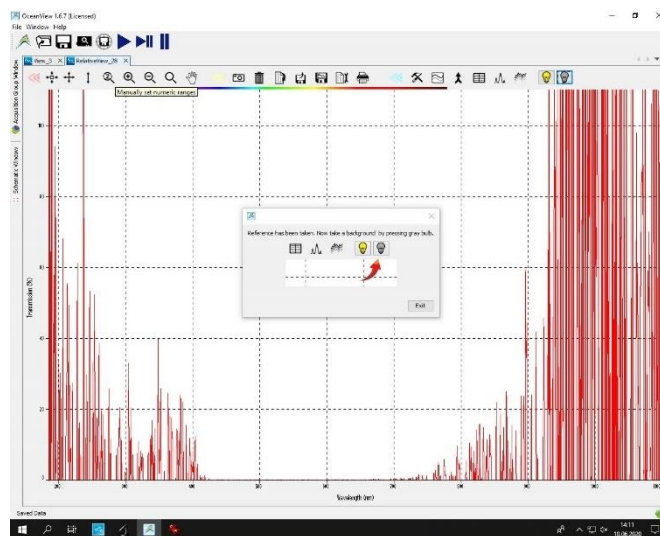


When the reference sample (in the cuvette) is placed in the setup (Figure 35) for the transmission signal reading, the reference is made to the readings of the other samples to be read.

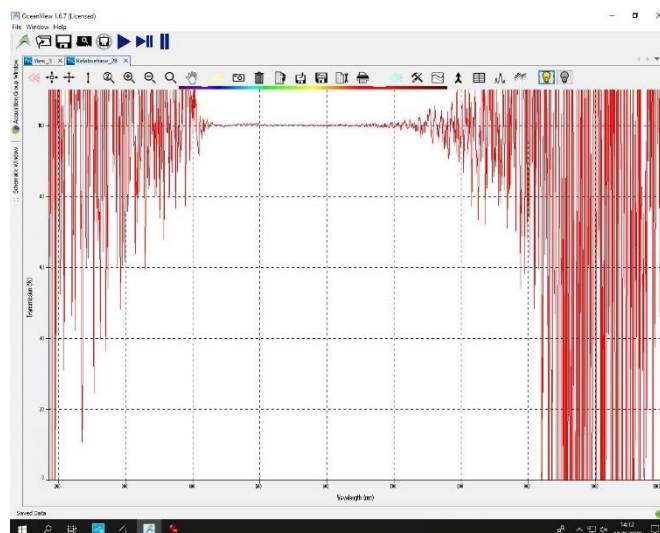
The first step is to click on the yellow lamp while the light source is on.



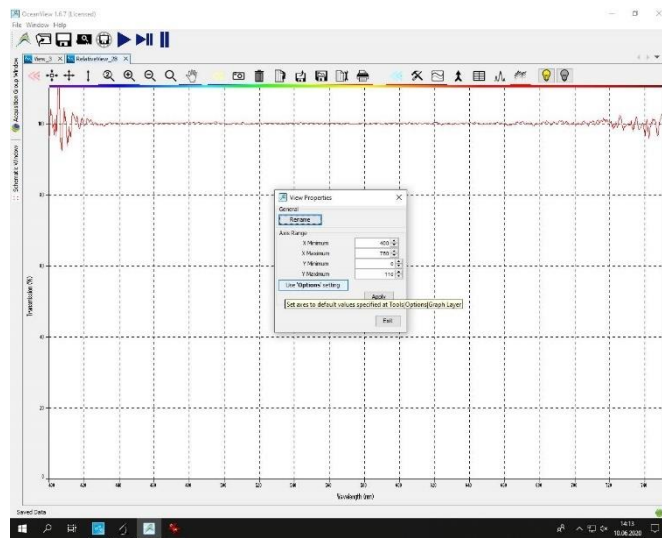
The second step is to turn off the light source and click on the grey lamp.



When the light source is switched on again we already have the transmittance signal of the reference solution as 100%.



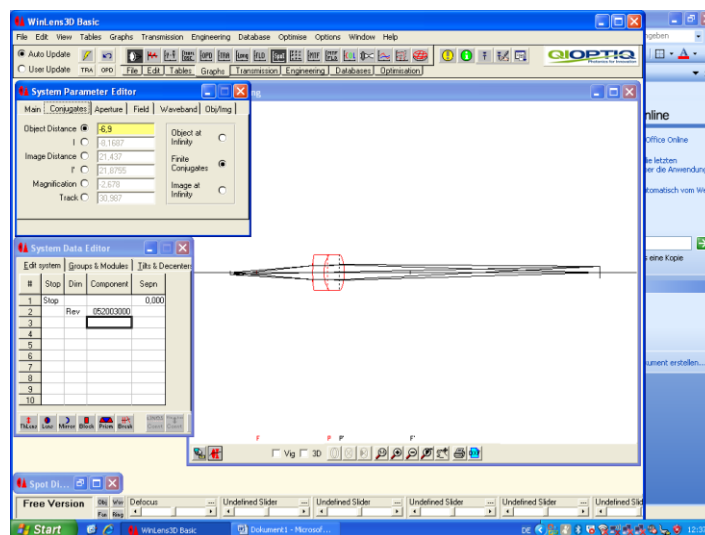
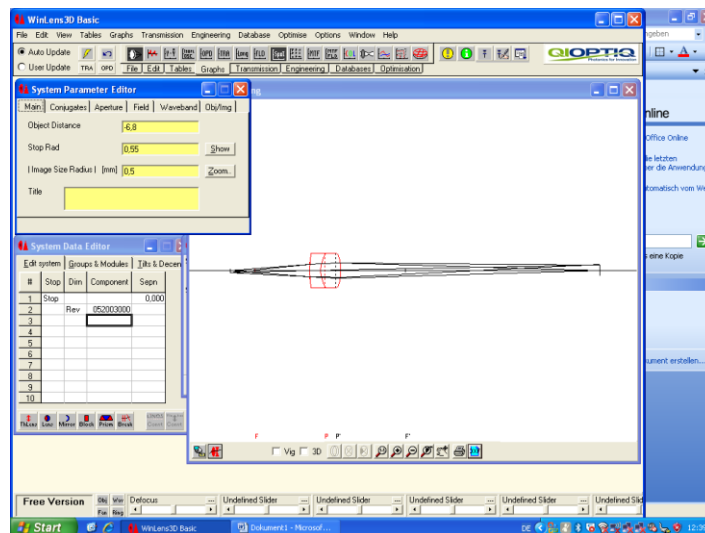
The reading window can then be adjusted in the View Properties to the desired wavelength range.



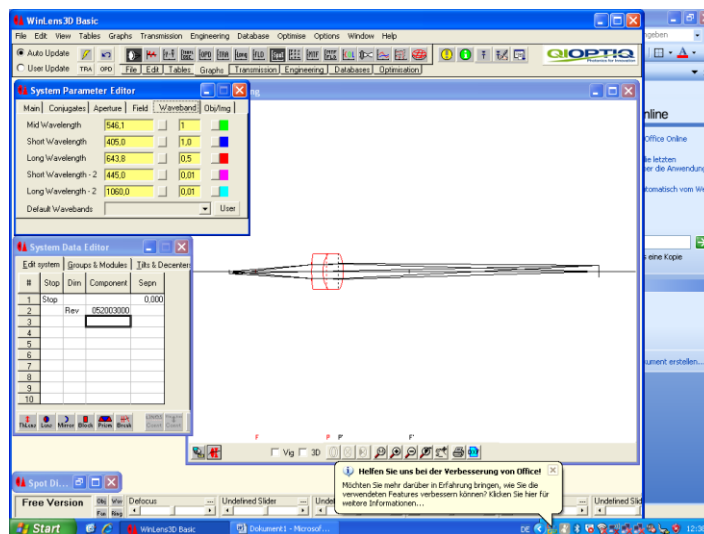
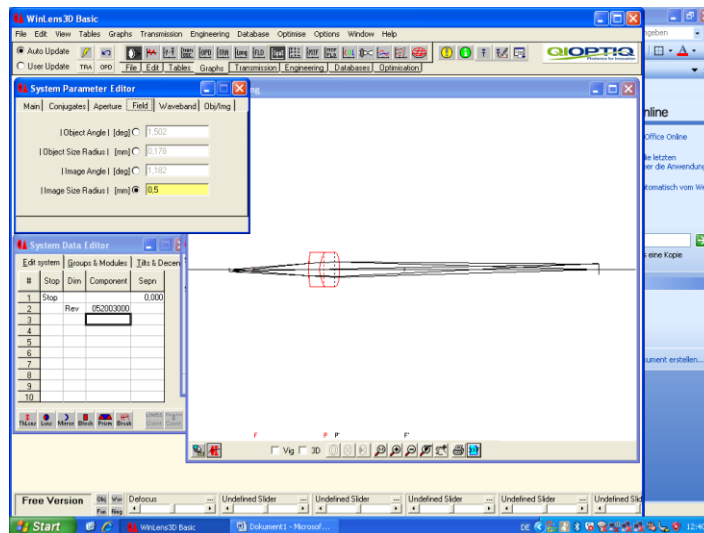
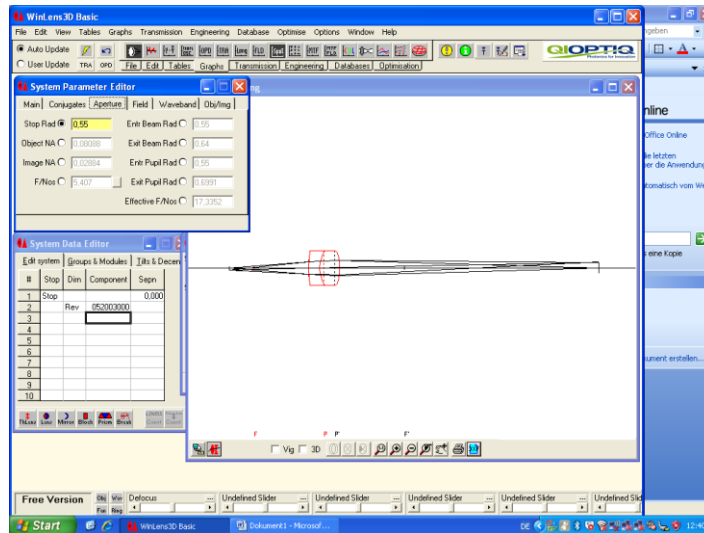
Appendix IV

WinLens3D Basic software is an easy-to-use and fast study software for light beam behaviors that pass-through lenses. First, the setup is defined in the System Data Editor and the lens is defined by a code present in the program database, which in the case of the N-BK7 is given by 0502003000.

After the setup is set, the distance of the object is set in the System Parameter Editor and on the "Conjugates" we can know what is the respective Image Distance.



A Stop Rad of 0.44 is also set in the System Parameter Editor "Aperture" and an Image Size Radius module in the Field.



In the System Parameter Edit "Obj/Img" the middle of the object and image are defined and the

Appendix V

The interface code is presented here in full.

```
import controlP5.*;
import processing.serial.*;

Serial myPort; // Create object from Serial class
String val;    // Data received from the serial port

//global variables used in the draw function
Integer count= 1;
float prev=0;
int ref=1;

//button variables
int[] button = new int[5];
int[] button2 = new int[5];

PFont f; //creat font variable

void setup()
{
  // Open the port
  String portName = Serial.list()[0]; //0 is respective number at port
  3 of                                     //the pc where the interface was
  created
  myPort = new Serial(this, portName, 9600);
}

public void settings() {
  size(400,300,P2D); //siye of the GUI
  button[0]=0;      //x coordinate
  button[1]=0;     //ycoordinate
  button[2]=20;    //width lenght
  button[3]=20;    //height length
  button[4]=0;

  button2[0]=30;   //x coordinate
  button2[1]=0;   //ycoordinate
  button2[2]=20;  //width lenght
  button2[3]=20;  //height length
  button2[4]=0;
}

void draw()
{
  fill(204, 102, 0); //color defined with (R,G,B) coordinates
  rect(button[0], button[1], button[2], button[3]); //creating a
  rectangle using the button
  if (button[4]==1){
    rect(100,100,30,30);
  }
}
```

```

}

fill(204, 102,200); //color defined with (R,G,B) coordinates
rect(button2[0], button2[1], button2[2], button2[3]); //creating a
rectangle using the button2
if (button2[4]==1){
    rect(100,100,30,30);
}

if ( myPort.available()> 0) // If data is available,
{
    val = myPort.readStringUntil(&apos;\n&apos;);          // read it and
store it in val
    val= trim(val);    //removes spaces present in the beginning or in
the end of the string
    println(val); //print it out in the console

    if ((mouseY<(button2[1]+button2[3]))&& (mouseY>(button2[1]))){
//if the mouse passes over the button2 the received
        if ((mouseX<(button2[0]+button2[2]))&& (mouseX>(button2[0]))){
//values are given to the variable ref
            ref= int(val);
        }

        int green=int(val);
        int g=(green/ref)*100; //percentage normalization
        float r; //variable r saves the respective pH value
        r=0;
        if ((g>99) && (g<=150)) r=6.0;
        else if ((g>98.5) && (g<=99))    r=6.2;
        else if ((g>98.0) && (g<=98.5)) r=6.4;
        else if ((g>97) && (g<=98.0))    r=6.6;
        else if ((g>95.5) && (g<=97))    r=6.8;
        else if ((g>93) && (g<=95.5))    r=7.0;
        else if ((g>91) && (g<=93))      r=7.2;
        else if ((g>89) && (g<=91))      r=7.4;
        else if ((g>86) && (g<=89))      r=7.6;
        else if ((g>83) && (g<=86))      r=7.8;
        else if ((g>80) && (g<=83))      r=8.0;
        float graphy= map(g, 0, 120, 0, height); //re-maps a number to
range of the window (0 and height)

        if ((mouseY<(button[1]+button[3]))&& (mouseY>(button[1]))){
            if ((mouseX<(button[0]+button[2]))&& (mouseX>(button[0]))){
stroke(0,0,255); //set the color of the graph as blue
line(prev, height-graphy, count, height-graphy);

f= createFont("Arial",16,true);//creat font
fill(255);          //color of the box for pH value
rect(100,5,100,30); //box for pH value
fill(0);           //color for text
textFont(f,16);    //let write in the font
text("pH=",100,20); //(text,x,y)
text(r,140,20);

prev=count;

```

```
    if(count>=width){ //if values fill the entire window it delete
the line
        count=0; //and start again in the x=0
        prev=0;
        background(200);
    }
    else
    {
        count++; //advance in the x coordinate
    }
}
}
```